3-31-2022 3:00 PM

Testing Aftershock Forecasts Using Bayesian Methods

Elisa Dong, *The University of Western Ontario*

Supervisor: Goda, Katsuichiro, *The University of Western Ontario*
Joint Supervisor: Shcherbakov, Robert, *The University of Western Ontario*
A thesis submitted in partial fulfillment of the requirements for the Master of Science degree in Geophysics

Abstract

The presence of strong aftershocks can increase the seismic hazard following a large earthquake and should be considered for operational earthquake forecasting and risk management. Aftershock forecasts are generated from seismicity models during the evolution of the aftershock sequence. This work compares quantitative test results of the forecasting abilities for three competing aftershock rate models - the modified Omori law, the Epidemic Type Aftershock Sequence model, and the compound Omori law - to identify the best performing model for forecasting the largest aftershock during the early aftershock sequence. Forecasts of large aftershock probabilities are generated by either the Extreme Value distribution or the Bayesian Predictive distribution for the forecasting time interval. Testing is conducted retrospectively on five sequences for a fixed forecasting time interval of seven days during the early aftershock sequence. None of the models and forecasting methods consistently outperforms the others regardless of the training time interval.

Keywords: Aftershock forecasting, Bayesian predictive distribution, ETAS model, Modified Omori law, Compound Omori law, Forecasting statistics, Forecast performance testing, Extreme value theory

Summary for Lay Audience

Large earthquakes and their subsequent aftershocks are destructive. The presence of strong aftershocks can increase the seismic hazard and should be considered for operational earthquake forecasting and risk management. In this study, selected large earthquakes and their aftershocks are analyzed using three models, the modified Omori law, the Epidemic Type Aftershock Sequence model, and the compound Omori law. The models are applied to data available during various lengths of time as the earthquake sequence progresses. For each length of time, the behaviour of the sequence is simulated for the next seven days. From the simulation, the probability of a large aftershock can be computed as a forecast. This study mimics operational forecasting by progressively increasing the amount of available data for each forecast. The probability for large aftershocks is computed using two different methods - the Extreme Value distribution and the Bayesian Predictive distribution. Several statistical tests are applied to the forecasting methods and evaluated for performance. Models are scored based on quantitative values for their performance and the results are used to compare the performance of the respective models and forecasting methods. The goal of this work is to determine whether one model and forecasting method consistently scores better than the others when forecasting large aftershocks using data available during the early aftershock sequence.

The results of the statistical testing indicate that there is no best model nor forecasting method. The most suitable model and method may be regional or sequence dependent. This suggests that the choice of using one model over another should be carefully considered. To forecast the probability of the largest aftershock occurring during a short time period more reliably, the early aftershock behaviour of sequences requires more detailed analysis in future studies.

Acknowledgements

I want to acknowledge Katsu Goda who had the faith and was the first to take me on as his student. Katsu has always found the time to give detailed feedback on nearly every piece of writing, encouraged me to find what I was passionate about, and listened to all my concerns.

Thanks to Robert Shcherbakov who spent many hours trawling through code with me and providing me with the starting material for this thesis, Sheri Molnar for suggesting I find a way to escape the lonely academic bubble I was living in, Sean Shieh for always sharing life advice, and the many other professors that showed kindness and support during this time. I would also like to acknowledge my fellow labmates - Karina, Yusong, and Charles - for keeping me company on this shared journey.

Thank you to everyone that played D&D with me in the last three years and gave me a distraction to look forward to, especially Joshua and TianTian who let me rule the world with an iron fist, and Nathan for always sharing stories. I'd like to thank my family for their patience with me as I struggled to finish data analysis during the pandemic, and my friends for supporting me throughout several injuries and hard times. Special thanks to my roommates Max and Rachel who were there for the beginning, and the end, respectively. Extra special thanks to Mauritz and the cats for letting me give head pats.

Lastly, I would like to acknowledge Thila Varghese from the Writing Support Centre, for excellent feedback and continual support. Writing would have taken much longer on my own.

There are many other people I would like to thank that have supported me on this journey. It has been a pleasure and quite an adventure. Thank you all.

Contents

Abstract i

Summary for Lay Audience ii

Acknowledgements iii

List of Figures viii

List of Tables xiii

List of Appendices xvii

List of Abbreviations, Symbols, and Nomenclature xviii

1 Introduction 1

1.1 Probability of Large Earthquakes 1

1.2 Rationale for This Study 3

1.2.1 Study Goals 5

1.3 Background and Concepts 6

1.3.1 Earthquakes 6

1.3.2 Gutenberg-Richter Law 8

1.3.3 Modified Omori Law 9

1.3.4 Epidemic Type Aftershock Sequence Model 9

1.3.5 Compound Omori Law 10

1.3.6 Model Fit and Parameter Estimation 11

Magnitude Completeness . . . 11
1.3.7 Forecasting . . . 11
1.3.8 Testing Forecasts . . . 14
1.4 Selected Case Studies . . . 15
1.5 Thesis Overview . . . 15

2 Data and Methods **17**
2.1 Data . . . 17
2.1.1 Italian Catalog - ISIDe . . . 18
2.1.2 Japanese Catalog - JMA . . . 19
2.1.3 United States of America Catalog - ComCat . . . 19
2.1.4 New Zealand Catalog - GeoNet . . . 19
2.2 Methods . . . 19
2.2.1 Model Training Time Intervals . . . 23
2.2.2 Model Region Selection . . . 24
2.2.3 Magnitude Completeness Analysis . . . 24
2.3 Gutenberg-Richter Law . . . 25
2.4 Temporal Seismicity Rate Models . . . 26
2.4.1 Modified Omori Law . . . 27
2.4.2 Compound Omori Law . . . 27
2.4.3 ETAS Model . . . 28
2.5 Model Parameter Fitting . . . 29
2.5.1 Maximum Likelihood Estimate . . . 29
2.5.2 Markov Chain Monte Carlo Chains . . . 30
2.6 Forecasting Methods . . . 31
2.6.1 Extreme Value Distribution . . . 31
2.6.2 Bayesian Predictive Distribution . . . 33
2.7 Statistical Tests . . . 34

2.7.1 N-Test . . . 35
2.7.2 M-Test . . . 37
2.7.3 R-Test . . . 38
2.7.4 T-Test . . . 38
2.7.5 Bayesian p-Test . . . 39

3 Case Studies **40**

3.1 The 2009 L'Aquila, Italy, Sequence . . . 41
3.1.1 Forecast Test Results . . . 48
3.2 The 2016 Amatrice, Italy, Sequence . . . 52
3.2.1 Forecast Test Results . . . 57
3.2.2 Forecasting the Second Largest Event . . . 59
3.3 The 2016 Kumamoto, Japan, Sequence . . . 60
3.3.1 Forecast Test Results . . . 66
3.4 The 2020 Monte Cristo Range, United States of America, Sequence . . . 68
3.4.1 Forecast Test Results . . . 72
3.4.2 Discussion in Response to the Monte Cristo Range Sequence . . . 74
3.5 The 2010 Darfield Sequence and 2011 Christchurch Events, New Zealand . . . 76
3.5.1 Forecasting Test Results . . . 80
3.5.2 Forecasting the 2011 Christchurch Event . . . 82

4 Discussion **84**

4.1 Interpretation of Forecast Tests . . . 86
4.2 Limitations and Assumptions . . . 93
4.2.1 Completeness . . . 93
4.2.2 Prior Information . . . 95
4.2.3 Background Seismicity Stationarity . . . 96
4.2.4 Forecasting Time Interval . . . 97

4.2.5 Additional Temporal Conditions 98
4.2.6 Limited Use of Compound Omori Law 99

5 Conclusions **100**

5.1 Summary of Work 101
5.2 Suggestions 103
5.3 Final Remarks 106

Bibliography **108**

A Functions and MATLAB Settings **127**

A.1 Log-Likelihood Functions 127
A.2 fmincon() Settings 128

B Additional Tables and Figures **130**

B.1 The 2009 L'Aquila, Italy Sequence 130
B.2 The 2016 Amatrice, Italy Sequence 137
B.3 The 2016 Kumamoto, Japan, Sequence 142
B.4 The 2020 Monte Cristo Range, United States of America, Sequence 149
B.5 The 2010 Darfield Sequence and 2011 Christchurch Events, New Zealand . . . 154
B.5.1 Increasing M_0 155

Curriculum Vitae **164**

List of Figures

1.1 Examples of earthquake sequences including mainshocks, foreshocks, and aftershocks 8

1.2 Visual reprentation of workflow following a large event leading to issuing an alarm. 13

2.1 World map showing epicenters of the mainshock for each case study. 18

2.2 Methodology flowchart from data collection to statistical testing done in this study. 21

2.3 Timeline of events during an earthquake sequence including the training time interval and forecasting time interval. 23

2.4 An example of quantile score interpretation on a plot for a forecasting test. . . . 36

3.1 Map of 2009 L'Aquila sequence during the first three days following the mainshock. 43

3.2 2009 L'Aquila sequence fitted to the GR law for the first three days. 43

3.3 Model parameter estimates for the L'Aquila sequence using the MLE method. . 45

3.4 Examples of the aftershock model fits for the 2009 L'Aquila sequence. 46

3.5 Probability of large aftershock for the 2009 L'Aquila sequence. 48

3.6 R-test and T-test performance for the L'Aquila sequence for the MOL and ETAS model as the competing hypotheses. 49

3.7 N-test, M-test, and p-test performance for the L'Aquila sequence for the MOL, CMOL, and ETAS model. 50

3.8 Map of 2016 Amatrice sequence during the first three days following the mainshock. 52
3.9 2016 Amatrice sequence fitted to the GR law for the first three days. 54
3.10 Model parameter estimates for the Amatrice sequence using the MLE method. . 54
3.11 Examples of the aftershock model fits for the 2016 Amatrice sequence. 55
3.12 Probability of large aftershock for the 2016 Amatrice sequence. 56
3.13 R-test and T-test performance for the Amatrice sequence for the MOL and ETAS model as the competing hypotheses. 57
3.14 N-test, M-test, and p-test performance for the Amatrice sequence for the MOL and ETAS model. 58
3.15 Map of 2016 Kumamoto sequence during the first three days following the mainshock. 60
3.16 2016 Kumamoto sequence fitted to the GR law for the first three days following the mainshock. 62
3.17 Model parameter estimates for the Kumamoto sequence using the MLE method. 63
3.18 Examples of the aftershock model fits for the 2016 Kumamoto sequence. 64
3.19 Probability of large aftershock for the 2016 Kumamoto sequence. 65
3.20 R-test and T-test performance for the Kumamoto sequence for the MOL and ETAS model as the competing hypotheses. 67
3.21 N-test, M-test, and p-test performance for the Kumamoto sequence for the MOL, CMOL, and ETAS model. 68
3.22 Map of 2020 Monte Cristo Range sequence during the first three days following the mainshock. 69
3.23 2020 Monte Cristo Range sequence fitted to the GR law for the first three days. 70
3.24 Model parameter estimates for the Monte Cristo Range sequence using the MLE method. 71
3.25 Examples of the aftershock model fits for the 2020 Monte Cristo Range sequence. 71

3.26 Probability of large aftershock for the 2020 Monte Cristo Range sequence. . . . 72
3.27 R-test and T-test performance for the Monte Cristo Range sequence for the MOL and ETAS model as the competing hypotheses. 73
3.28 N-test, M-test, and p-test performance for the Monte Cristo Range sequence for the MOL and ETAS model. 74
3.29 Map of 2010 Darfield sequence during the first three days following the mainshock. 77
3.30 2010 Darfield sequence with $M_0 = 3.3$ fitted to the GR law for the first three days. 78
3.31 Model parameter estimates for the Darfield sequence using the MLE method. . 79
3.32 Examples of the aftershock model fits for the 2010 Darfield sequence. 79
3.33 Probability of large aftershock for the 2010 Darfield sequence. 80
3.34 R-test and T-test performance for the Darfield sequence for the MOL and ETAS model as the competing hypotheses for $M_0 = 3.3$. 81
3.35 N-test, M-test, and p-test performance for the Darfield sequence for the MOL and ETAS model for $M_0 = 3.3$. 81

4.1 N-test performance for all sequences using the ETAS model. 88
4.2 N-test performance for all sequences using the MOL. 88

B.1 Probability of large aftershocks for the L'Aquila sequence using the a) MOL and b) CMOL produced by the EVD. 132
B.2 The performance of the MOL and CMOL on the N-test and M-test for the L'Aquila sequence using the EVD method for forecasting. 132
B.3 Average number of events generated during seven day forecast for L'Aquila sequence using the BPD method. 136
B.4 Probability of large aftershocks for the Amatrice sequence using the MOL produced by the EVD. 137

B.5 The performance of the MOL on the N-test and M-test for the Amatrice sequence using the EVD method for forecasting. 139
B.6 Average number of events generated during seven day forecast for Amatrice sequence using the BPD method. 139
B.7 Probability of large aftershocks for the Kumamoto sequence using the a) MOL and b) CMOL produced by the EVD. 142
B.8 The performance of the MOL and CMOL on the N-test and M-test for the Kumamoto sequence using the EVD method for forecasting. 144
B.9 Average number of events generated during seven day forecast for Kumamoto sequence using the BPD method. 148
B.10 Probability of large aftershocks for the Monte Cristo Range sequence using the MOL produced by the EVD. 149
B.11 The performance of the MOL on the N-test and M-test for the Monte Cristo Range sequence using the EVD method for forecasting. 151
B.12 Average number of events generated during seven day forecast for Monte Cristo Range sequence using the BPD method. 154
B.13 Probability of large aftershocks for the Darfield sequence with $M_0 = 3.3$ using the MOL produced by the EVD. 154
B.14 The performance of the MOL on the N-test and M-test for the Darfield sequence using the EVD method for forecasting using $M_0 = 3.3$. 160
B.15 Average number of events generated during seven day forecast for Darfield sequence with $M_0 = 3.3$. 160
B.16 Probability of large aftershocks for the Darfield sequence for $M_0 = 3.5$ forecasted using the a) MOL with BPD, b) MOL with EVD, and c) ETAS model. . 161
B.17 Probability of large aftershocks for the Darfield sequence for $M_0 = 3.7$ forecasted using the a) MOL with BPD, b) MOL with EVD, and c) ETAS model. . 162
B.18 N-test performance of the Darfield sequence with a) $M_0 = 3.5$ and b) $M_0 = 3.7$. 162

B.19 M-test performance of the Darfield sequence with a) $M_0 = 3.5$ and b) $M_0 = 3.7$. 163
B.20 a) R-test performance of the Darfield sequence with $M_0 = 3.5$. b) The associated information gain is plotted for $M_0 = 3.5$ with 95% confidence intervals. . . 163
B.21 a) R-test performance of the Darfield sequence with $M_0 = 3.7$. b) The associated information gain is plotted for $M_0 = 3.7$ with 95% confidence intervals. . . 163

List of Tables

2.1 Excerpt of the JMA catalog used for the 2016 Kumamoto sequence analysis. . . 17

3.1 R-test and T-test performance for the L'Aquila sequence for the MOL and CMOL model as the competing hypotheses. 49

3.2 R-test and T-test performance for the Kumamoto sequence for the MOL and CMOL model as the competing hypotheses. 67

B.1 The 2009 L'Aquila sequence model parameter estimates for the MOL using the MLE method and associated errors. 130

B.2 The 2009 L'Aquila sequence model parameter estimates for the CMOL using the MLE method and associated errors. 131

B.3 The 2009 L'Aquila sequence model parameter estimates for the ETAS model using the MLE method and associated errors. 131

B.4 Variance for 2009 L'Aquila sequence Gamma priors. 132

B.5 MCMC sampling of model parameter estimates for the L'Aquila sequence fitted to the MOL. 133

B.6 MCMC sampling of model parameter estimates for the L'Aquila sequence fitted to the CMOL. 134

B.7 MCMC sampling of model parameter estimates for the L'Aquila sequence fitted to the ETAS. 135

B.8 The 2016 Amatrice sequence model parameter estimates for the MOL using the MLE method and associated errors. 137

B.9 The Amatrice sequence ETAS model parameters estimated using the MLE method without fixing of model parameters. 138

B.10 The 2016 Amatrice sequence model parameter estimates for the ETAS model using the MLE method and associated errors where $\mu = 0.03$ is fixed. 138

B.11 Variance for 2010 Amatrice sequence Gamma priors. 138

B.12 MCMC sampling of model parameter estimates for the Amatrice sequence fitted to the MOL. 140

B.13 MCMC sampling of model parameter estimates for the Amatrice sequence fitted to the ETAS model. 141

B.14 The 2016 Kumamoto sequence model parameter estimates for the MOL using the MLE method and associated errors. 142

B.15 The 2016 Kumamoto sequence model parameter estimates for the CMOL using the MLE method and associated errors. 143

B.16 The 2016 Kumamoto sequence model parameter estimates for the ETAS model using the MLE method and associated errors. 143

B.17 Variance for 2016 Kumamoto sequence Gamma priors. 144

B.18 MCMC sampling of model parameter estimates for the Kumamoto sequence fitted to the MOL. 145

B.19 MCMC sampling of model parameter estimates for the Kumamoto sequence fitted to the CMOL. 146

B.20 MCMC sampling of model parameter estimates for the Kumamoto sequence fitted to the ETAS model. 147

B.21 The 2020 Monte Cristo Range sequence model parameter estimates for the MOL using the MLE method and associated errors. 149

B.22 Monte Cristo Range sequence ETAS model parameters estimated using the MLE method without fixing of model parameters with associated errors. 150

B.23 Monte Cristo Range sequence ETAS model parameters estimated using the MLE method with $\mu = 0.0$ fixed with associated errors. 150

B.24 The 2020 Monte Cristo Range sequence model parameter estimates for the ETAS model using the MLE method and associated errors. The model parameters $\mu = 0.0$ and $K = 0.1$ were fixed. The model parameter $c = 0.3$ was fixed for $\Delta T_m = 1, 2$ days for stability. 151

B.25 Variance for 2020 Monte Cristo Range sequence Gamma priors. 151

B.26 MCMC sampling of model parameter estimates for the Monte Cristo Range sequence fitted to the MOL. 152

B.27 MCMC sampling of model parameter estimates for the Monte Cristo Range sequence fitted to the ETAS model. 153

B.28 The 2010 Darfield sequence model parameter estimates using $M_0 = 3.3$ for the MOL using the MLE method and associated errors. 155

B.29 The 2010 Darfield sequence model parameter estimates using $M_0 = 3.3$ for the ETAS model using the MLE method and associated errors. 155

B.30 Variance for 2010 Darfield sequence Gamma priors. 155

B.31 MCMC sampling of model parameter estimates for the Darfield sequence fitted to the MOL for $M_0 = 3.3$. 156

B.32 MCMC sampling of model parameter estimates for the Darfield sequence fitted to the ETAS model for $M_0 = 3.3$. 157

B.33 The 2010 Darfield sequence model parameter estimates with $M_0 = 3.5$ for the MOL using the MLE method and associated errors. 158

B.34 The 2010 Darfield sequence model parameter estimates using $M_0 = 3.5$ for the ETAS model using the MLE method and associated errors. 158

B.35 The 2010 Darfield sequence model parameter estimates using $M_0 = 3.7$ for the MOL using the MLE method and associated errors. 159

B.36 The 2010 Darfield sequence model parameter estimates using $M_0 = 3.7$ for the ETAS model using the MLE method and associated errors. 159

List of Appendices

Appendix A Functions and MATLAB Settings 127
Appendix B Additional Tables and Figures 130

List of Abbreviations, Symbols, and Nomenclature

GR law	Gutenberg-Richter law
MOL	Modified Omori law
CMOL	Compound Omori law
ETAS	Epidemic Type Aftershock Sequence
MCMC	Markov Chain Monte Carlo
M_w	Moment magnitude
M_L	Local magnitude
M_{JMA}	Magnitude used by the Japan Meteorological Agency
M_0	Magnitude cutoff
M_c	Magnitude completeness
***N*-test**	Number test
***L*-test**	Likelihood test
***M*-test**	Magnitude test
***R*-test**	Ratio test
***T*-test**	Test inspired by Student's *t*-test
***p*-test**	Bayesian *p*-test
MLE	Maximum Likelihood Estimate
EVD	Extreme value distribution
BPD	Bayesian predictive distribution

JMA	Japan Meteorological Agency
USGS	United States Geological Survey
GeoNet	Geological hazard information for New Zealand provided by the Earthquake Comission and GNS Science
ISIDe	Italian Seismological Instrumental and Parametric Data-Base
LAQ	2010 L'Aquila, Italy, sequence
AMA	2016 Amatrice, Italy, sequence
KUM	2016 Kumamoto, Japan, sequence
DFL	2010 Darfield, New Zealand, sequence
MCR	2020 Monte Cristo Range, United States of America, sequence
ω	Model parameter estimates for the aftershock rate model
θ	Model parameter estimate for the GR law
b	GR b-value, related to β
β	Related to b-value by $\beta = \ln b$
λ_ω	Seismicity rate based on model parameter estimates ω
$\Lambda_\omega(\Delta T)$	Productivity based on model parameter estimates ω during ΔT
μ	Background seisimicity in ETAS model
K, K_0, K_1,K_2	Instantaneous productivity of MOL instance
c, c_0, c_1, c_2	Short time interval for each MOL instance before the MOL fits
p, p_0, p_1, p_2	Rate decay for each MOL instance

α	Efficiency of a parent shock generating aftershock activity based on its magnitude for the ETAS model, also the quantile score for the R-test
δ_1, δ_2	Quantile scores for the N-test
κ	Quantile score for the M-test
IG	Information gain from the T-test
p_B	Quantile score for the Bayesian p-test

Chapter 1

Introduction

One of the main purposes of earthquake research is the prevention of loss of life. Shaking of the Earth by moderate to large earthquakes disrupts activities on the surface and can cause infrastructure damage. Secondary effects of large earthquakes can also be taken under consideration when prioritizing studies of earthquake behaviour. Secondary effects may include landslides, liquefaction, fires, and power grid impacts, which all contribute to the loss of life [Kossobokov, 2013, Zhang et al., 2018, Petersen et al., 2020]. Aftershocks, earthquakes that take place following large earthquakes, may also cause these effects. The more aftershocks take place, the more likely these effects will occur. Given the potential physical and societal damage, improvements to the response time and general preparatory steps to large earthquakes during aftershock sequences can be made. Much attention has also been given to the forecasting of the large earthquakes and their associated sequences [Utsu, 1971, Reasenberg and Jones, 1989, Zechar et al., 2010, Rhoades et al., 2011, Page et al., 2016, Earthquake Research Committee, 2016].

1.1 Probability of Large Earthquakes

The occurrence of very large earthquakes near populated areas, such as those exceeding moment magnitude 7, tends to dominate the discussion in terms of safety, earthquake preparedness, and building requirements [Woessner et al., 2015,

Earthquake Research Committee, 2016, Hardebeck et al., 2019, Petersen et al., 2020]. These earthquakes have special considerations in the public view and are understandably a high priority in terms of anticipating their occurrence as they are associated with higher risk. However, earthquakes with moment magnitude as low as $M_w = 4.0$ should be considered as they contribute to the seismic hazard in the short term (e.g., 50 years in Europe) [Beauval et al., 2008, Delavaud et al., 2012]. For mainshocks that result in long and productive sequences, the greater number of aftershocks increases the probability that one of these may be a large magnitude event [Reasenberg and Jones, 1989, Page et al., 2016].

Since aftershocks are typically present following a sufficiently large magnitude event, it is necessary to consider what the probability of a large or "mainshock" event occurring is. The premature labelling of events can lead to a false sense of security as the public may not consider that a larger event will take place shortly afterwards [Omi et al., 2019]. Thus, the probability that a temporarily labelled mainshock will have a larger magnitude aftershock should be considered, especially during the time close to the mainshock as the sequence tends to be the most productive at this time. To do so, computational methods and models can be applied to estimate the probability of a large event.

For short-term forecasting, it is important to use a suitable model to describe the known seismicity. In addition, for the forecast to be useful, the forecast should demonstrate features that closely align with the observed seismicity. Some features that can be considered include: the number of events, the magnitude distribution of the events, and the maximum magnitude event. Several models have been published and are available in the literature. Two common aftershock rate models used in real-time forecasting are the Epidemic Type Aftershock Sequence (ETAS) model and the modified Omori law (MOL) [Omori, 1894, Utsu, 1961, Ogata, 1998, Ogata, 1999]. Other models include those based on rate-and-state, stick-slip, Every Earthquake a Precursor According to Scale, and the compound Omori law, in addition to the many region-specific models [Dieterich, 1994, King et al., 1994, Utsu et al., 1995, Scholz, 2002, Evison and Rhoades, 2004, Rhoades and Evison, 2004, Field et al., 2009, Strader et al., 2017,

Rhoades et al., 2017]. The magnitude distributions are typically assumed to follow the Gutenberg-Richter law [Gutenberg and Richter, 1944].

Basic forecasting may use the forecasted rate model to calculate the number of events and assign magnitudes to individual events. Forecasting can also be done by forward simulation of the fitted models. The results of any improvements to forecasting methods will be reflected in downstream products such as early aftershock warnings [Helmstetter and Sornette, 2003, Zechar and Jordan, 2008, Allen et al., 2009, Shebalin et al., 2012, Kawamoto et al., 2016, Chung et al., 2020].

Short-term forecasting, where the forecast is on the order of days, provides the ability to respond to on-going earthquake events to evaluate the value of issuing announcements such as recommendations for return or evacuation warnings to and from an affected site. For example, the United States Geological Survey (USGS) and the Japan Meteorological Agency (JMA) currently make use of the modified Omori law as the primary earthquake aftershock model and issue forecasts based on the probability of exceeding a certain magnitude threshold [Hardebeck et al., 2019, Earthquake Research Committee, 2016, Omi et al., 2019]. More recently, there has a been a shift towards implementing the ETAS model for forecasting as the main method or an additional option in future versions of current forecasting methods [Marzocchi and Lombardi, 2009, Omi et al., 2016, Omi et al., 2019]. In the USGS, the ETAS model is used on demand [N/A, 2020]. This is presumably due to the inherently stochastic nature of the ETAS model which demonstrates more variability in the sequence behaviour and the expectation that the ETAS model may perform better and more accurately describe the number of forecasted events and magnitude distribution.

1.2 Rationale for This Study

While it is desirable to develop a method of when and where large shocks will occur, the precise prediction of large shocks is not feasible [Geller, 1997, Geller et al., 1997]. It is, however, possible to characterize the aftershock behaviours and make use of them to provide

forecasts in the near future, such as the next several hours to days. This is also of great importance as this knowledge provides decision-makers with the information necessary to decide when to evacuate and when it may be appropriate for citizens to return to a previously impacted area. Thus, the forecasting of earthquake behaviour during sequences should be improved and incorporate new understanding of earthquake behaviour where possible.

To improve forecasting, retrospective analysis can be applied to earthquake sequences that have occurred in the past. When both training and testing data are available, models can be tested on their performance. This is the case with early aftershock sequences (training data) and the following aftershocks (testing data). Then, models that are currently in use, or newly proposed models can be trained and tested to evaluate whether they produce useful forecasts. Testing must be done to assess the features of the forecast before the model can be used reliably for real-time purposes. Test results should also be produced in a form similar to previous work, easily replicated, and the tests should ideally be easy to interpret. The limitations of the forecasts from different models can also be identified during retrospective analysis.

The organized effort to put together forecasting testing and a systematic way of comparing the forecast results has been in progress for over a decade now, such as with the Collaboratory for the Study of Earthquake Predictability (CSEP) [Zechar et al., 2009]. However, the results from this testing have not provided a conclusion as to the best overall model for forecasting. The testing conducted by the CSEP is for longer term forecasts and requires advance preparation [Zechar et al., 2009, Lombardi and Marzocchi, 2010a]. Previous work using the CSEP tests has shown that certain models perform better on various metrics for specific time frames, as summarized in [Schorlemmer et al., 2018, Rhoades et al., 2018]. In addition, many of the models being tested are region specific and cannot automatically be applied to other regions without careful consideration [Zechar et al., 2009, Gerstenberger and Rhoades, 2010]. To standardize the testing process, the submitted models do not receive additional human input and do not tend to account for the variability in initial parameter estimates as demonstrated in [Shcherbakov et al., 2019]. The current state of practice is to analyze one sequence at a

time, apply an alternative forecasting model, then compare the forecast performance based on the previous model used for forecasting and the alternative forecast performance based on the observed events such as in [van der Elst et al., 2022]. Competing forecast models have not previously been tested in a systematic manner for several sequences occurring in different regions.

1.2.1 Study Goals

The goal of this thesis is to provide quantitative analyses of the forecasts produced using different aftershock rate models and forecasting methods by means of a series of statistical tests to identify if one model consistently performs better than the others on specific metrics. By applying consistent statistical tests with quantile scores and reviewing the information gain of competing models, it may be possible to identify which model tends to perform better than the others.

In this work, three different models using two different forecasting methods are tested for forecast performance and compared. While Bayesian methods have been previously used in model parameter estimation and forecasting, Shcherbakov et al. (2019) recently investigated the use of the Bayesian Predictive distribution (BPD) to account for inherent uncertainty of model parameter estimation. While similar work is being conducted by the CSEP group, this study is the first direct comparison of the ETAS model and the MOL, both of which are used for real-time forecasting. In addition, the compound Omori law (CMOL), which is a model that has features in between the ETAS model and the MOL is also included for testing where applicable.

The thesis goal will be achieved with three primary objectives. The first objective is to evaluate the forecast test scores for model performance. The second objective is to assess the limits of each model and sequence to determine if there are specific conditions that the model performs better under. Considerations include the catalog magnitude completeness, necessity of fixing model parameters, and sensitivity to model parameter priors on the forecasting results. Third, the impact of magnitude cutoff is examined on the above objectives.

The results of this study are intended to better inform current real-time forecasting prac-

tices. The quantitative scores allow for straightforward comparison between the different methods and models tested. The results of this work can provide quantitative guidelines for policy and decision-makers when considering more than one model or method for forecasting earthquake sequences. The forecast test results also isolate specific features in the forecasts and indicate if the model and method used to forecast does not successfully replicate the corresponding features in the observed sequence. In addition, this work provides examples of forecast test score interpretation.

1.3 Background and Concepts

To have quantifiable forecasts and simulations that can be compared to observed seismicity, it is necessary to have a model that can describe the earthquake sequence. The model can then be used to generate a forecast. There are empirical laws which describe various aspects of earthquakes. Some well-known ones include the Gutenberg-Richter (GR) law which relates magnitude and frequency [Gutenberg and Richter, 1944, Gutenberg and Richter, 1955], the modified Omori law which describes the aftershock behaviour following a mainshock, and the Utsu-Seki law which describes the relationship between the rupture length and the magnitude of the event [Omori, 1894, Utsu et al., 1995]. The aftershock models used in this study include the MOL, ETAS model, and the CMOL [Omori, 1894, Utsu, 1961, Utsu et al., 1995, Ogata, 1998, Ogata, 1999]. The magnitude-frequency distribution of the sequences is described by a left-truncated GR law.

1.3.1 Earthquakes

An earthquake is the result of exceeding a critical value of stress within the Earth's crust, leading to a physical slip along a fault in the crust and release of energy [Kanamori, 1977, Abercrombie et al., 2006]. Forces in the Earth's crust contribute to continuous loading of stress and strain. Earthquake ruptures may be triggered in areas of weakness and slip in response to a large change in the stress field. Thus, one large earthquake or stress release may lead to the occurrence of aftershocks. The total energy released with each earth-

quake can be represented using the moment magnitude (M_w), which has a logarithmic scale [Kanamori, 1977, Hanks and Kanamori, 1979]. For regional catalogs, magnitudes may be recorded using a local magnitude (M_L) which can be converted between different magnitude scales [Richter, 1935, Kanamori, 1977, Hanks and Kanamori, 1979, Kanamori, 1983, Bindi et al., 2005, di Bona, 2016, Mueller, 2019].

A collection of earthquake events related by space and time is called an earthquake sequence. The events in a sequence can be treated as a stochastic marked point process in time. The event times t_i and magnitudes m_i are organized in a set $S = (t_i, m_i) : i = 1, \ldots, n$ [Vere-Jones, 1975, Ogata, 1999]. If the assumption is made that the magnitudes are not correlated and that t_i can be fully described by the time-dependent rate $\lambda(t)$, then earthquake occurrences can be modelled as a non-homogeneous Poisson process in time [Utsu et al., 1995, Shcherbakov et al., 2005b]. This abstraction of earthquake sequences then allows for forecasting based on the sequence properties described by the models.

During retrospective analysis, the largest event in the sequence is referred to as the mainshock. The events before and after are foreshocks and aftershocks, respectively. During a real-time situation, the first, large shock may be designated the "mainshock" until a larger event takes place. An example of some possible earthquake sequences is shown in Figure 1.1.

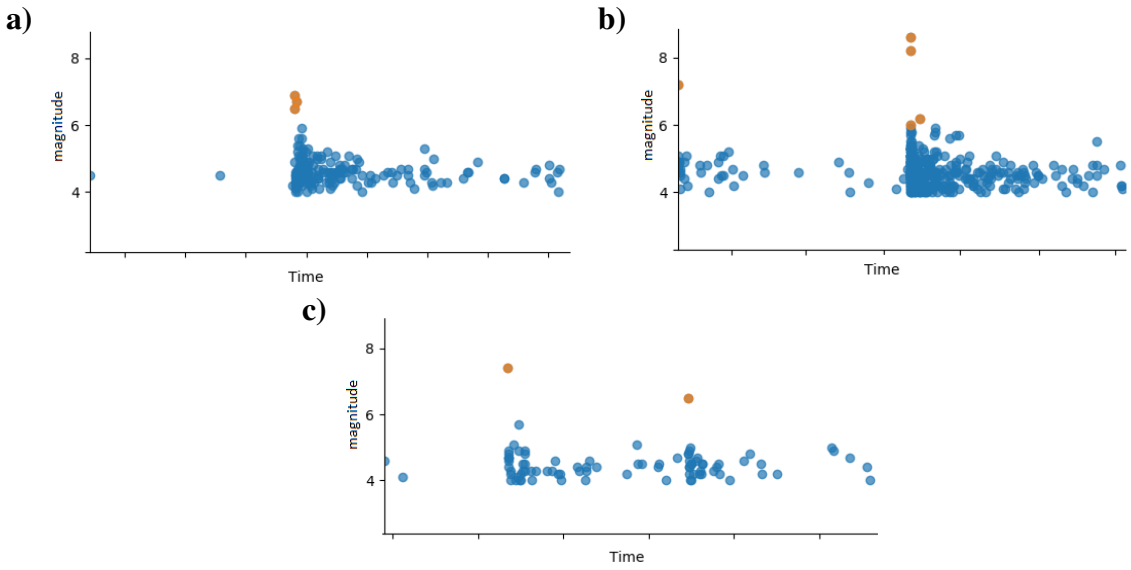

Figure 1.1: Examples of a different earthquake sequences representing mainshocks, foreshocks, and aftershocks. The y-axis denotes the magnitude of the events, and the x-axis is the relative time of the events. Events with magnitudes $M > 6$ are shown in orange. a) demonstrates the typical mainshock with aftershock sequence. b) shows a strong foreshock with its own aftershocks (foreshock sequence) preceeding a mainshock and aftershock sequence. c) demonstrates a mainshock with aftershock sequence and a strong shock during the sequence, producing an elevated seismicity rate and its own aftershock sequence.

1.3.2 Gutenberg-Richter Law

The GR law comes from an observation that there are relatively fewer large magnitude earthquakes in comparison to small magnitude earthquakes [Gutenberg and Richter, 1944]. At the extreme end, the number of $M_w \geq 9.0$ earthquakes in the last century is easily countable, while the number of tremors $M_w \leq 1.0$ are extremely numerous, and cannot be completely recorded due to factors such as strength of seismic signal and attenuation. The GR law applies to both global and local events, and applies to aftershocks [Shcherbakov et al., 2005a, Shcherbakov et al., 2015]. The value that is typically reported for the GR law fit is the b-value, which describes the relative number of small to large earthquakes in the sequence. The b-value has been shown to change leading up to large earthquakes and is also associated with the type of faulting present [Scholz, 1968, Wyss, 1973, Kanamori and Anderson, 1975, Båth, 1981, Frohlich and Davis, 1993, Márquez-Ramírez et al., 2015]. The b-value typically varies be-

tween $0.8 < b < 1.1$, where $b \sim 1.0$ is the average value globally [Frohlich and Davis, 1993, Márquez-Ramírez et al., 2015].

1.3.3 Modified Omori Law

The MOL is an aftershock rate model developed on an observation that the aftershock rate, λ_ω, decreases as time increases from the mainshock [Omori, 1894, Utsu et al., 1995]. The aftershock rate as modelled by the MOL has an inverse rate related to the time passing from the mainshock [Utsu, 1961]. Following a large shock, the aftershock rate is elevated and the time between events is small. As time passes from the mainshock, the aftershock rate of the sequence decreases until it reaches a stable rate of seismicity or returns to background seismicity levels. The MOL typically fits aftershock sequences well and is one of the aftershock models that is often used by government agencies, such as the USGS, for forecasting the probable behaviour of the ongoing aftershock sequence [Hardebeck et al., 2019]. The MOL has also been used for early forecasting and used with daily adaptive forecasting in [Ebrahimian et al., 2014, Ebrahimian and Jalayer, 2017]. Aftershocks that follow this empirical law show "Omori-like behaviour". While frequently used, the MOL does not account for secondary aftershocks - aftershocks produced by events other than the mainshock, and localized clustering behaviour.

1.3.4 Epidemic Type Aftershock Sequence Model

The ETAS model is a self-exciting point process which allows for each shock to generate its own associated aftershock sequence which decays in an Omori-like fashion [Ogata and Katsura, 1986, Ogata, 1988, Zhuang et al., 2011]. This model addresses clustering behaviour and punctuation in the sequence in a way that incorporates MOL behaviour with a limited number of parameters. Utsu (1995) suggests that the ETAS model is the best model that incorporates behaviour described by the MOL, which is necessary to describe aftershocks [Ogata and Katsura, 1986, Ogata, 1988, Zhuang et al., 2011]. The seismicity rate as described by the ETAS model is a sum of two rates, background rate and triggered rate, re-

flecting background and triggered events, respectively. The constant background rate, which is not associated directly with the earthquake sequence and occurs independently as a Poisson process, is explicitly accounted for in the ETAS model. Moreover, the ETAS model allows for the background events to trigger events as part of the sequence. For each event in the sequence, the event can be considered a "parent" event if it generates associated aftershocks, which are called "daughter" events. Like the MOL, larger parent events are more likely to produce a larger number of daughter events.

The ETAS model is also self-exciting and the aftershock rate is dependent on the history of events. Thus, the model parameter estimations for the ETAS model can be more difficult and multiple model fits can be found. During forecasting, the rate cannot be calculated directly and requires simulation dependent on the magnitude of individual events. The use of the ETAS model may be unnecessary if the sequence clearly demonstrates Omori-like behaviour with little to no background seismicity present.

1.3.5 Compound Omori Law

The MOL assumes that the sequence behaviour is dominated by the mainshock and the ETAS model allows for each event to trigger more events, all of which can produce Omori-like aftershocks. When a sequence that has strong secondary aftershocks clearly associated with one specific earthquake, such as a doublet type sequence with a second instance of Omori-like behaviour, an intermediate model can also be considered. The basic CMOL is described as two instances of the MOL which take place at different times during the sequence [Utsu, 1970, Ogata, 1983]. A second instance of the MOL begins at a second large shock in the sequence. The second MOL instance contributes to the seismicity in addition to the partially decayed rate from the first instance of the MOL by using a step function that "turns on" the additional MOL function at the time of the large aftershock [Utsu, 1971, Ogata, 1983, Shcherbakov et al., 2012, Shcherbakov, 2021]. The CMOL can be further extended to many instances of stacked events which contribute to increased seismicity by adding an additional MOL component.

1.3.6 Model Fit and Parameter Estimation

For each aftershock model, the rate of earthquake occurrence is described by the model parameter values. Estimation of the model parameters is done using a model fitting procedure during the training time interval. The estimated parameters are then used to forecast future earthquakes during the forecasting time interval. When assuming that aftershocks are a non-stationary Poisson process, the aftershock rate can be solved using an optimization method [Ogata, 1983].

The uncertainty of point parameter estimates is important to address as the uncertainty can propagate through the forecasting time period. The ETAS model is particularly affected due to its rate dependence on prior events. Variations in parameter estimates can lead to different forecasts. To account for the nature of the ETAS model and incorporate the model parameter uncertainty, Markov Chain Monte Carlo (MCMC) algorithms can also be used to sample the distribution of the parameters [Shcherbakov et al., 2019].

Magnitude Completeness

When modelling earthquake sequences, it is important to consider the completeness of the data [Kagan, 2004, Peng et al., 2006, Hainzl, 2016a, Hainzl, 2016b]. The completeness magnitude M_c can be considered the lowest magnitude event consistently in a catalog. See Chapter 2 for identifying M_c. Small earthquake magnitudes at distances far from seismic stations will not be accounted for as their signals are too small. M_c decreases as additional seismic stations are deployed to increase coverage and increases temporarily if signals overlap following a large shock or instrumental failure takes place [Agnew, 2015]. To properly estimate the aftershock rate and model parameters, the impacts of early aftershock incompleteness need to be considered [Ogata, 1988, Kagan, 2004, Peng et al., 2006, Hainzl, 2016a, Hainzl, 2016b].

1.3.7 Forecasting

For specific and constrained regimes in space and time, it may be possible to provide probability estimates of large earthquakes for active fault segments as the region approaches

a state of criticality or during an ongoing sequence [Sykes et al., 1999]. Efforts have been put into place to better identify and analyze the characteristics of earthquakes to forecast during earthquake sequences or shortly there-after [Zechar et al., 2009, Rhoades et al., 2011, Schorlemmer et al., 2018]. An example series of actions for practical, real-time forecasting follows. Shortly after a large earthquake event, the associated seismicity is collected as a sequence. The sequence can be rapidly characterized using a well-fitting aftershock model. From the model fit, the probability of large events and the behaviour of the sequence can be forecasted. The results of the short-term forecast (hours to days) can assist in decision making. See Figure 1.2 for an example of the data collection to alarm issuing workflow.

To provide meaningful short-term forecasting, models describing the behaviour of the earthquake sequence are necessary. In addition, an evaluation of both their fit and forecast are important when there is more than one model available.

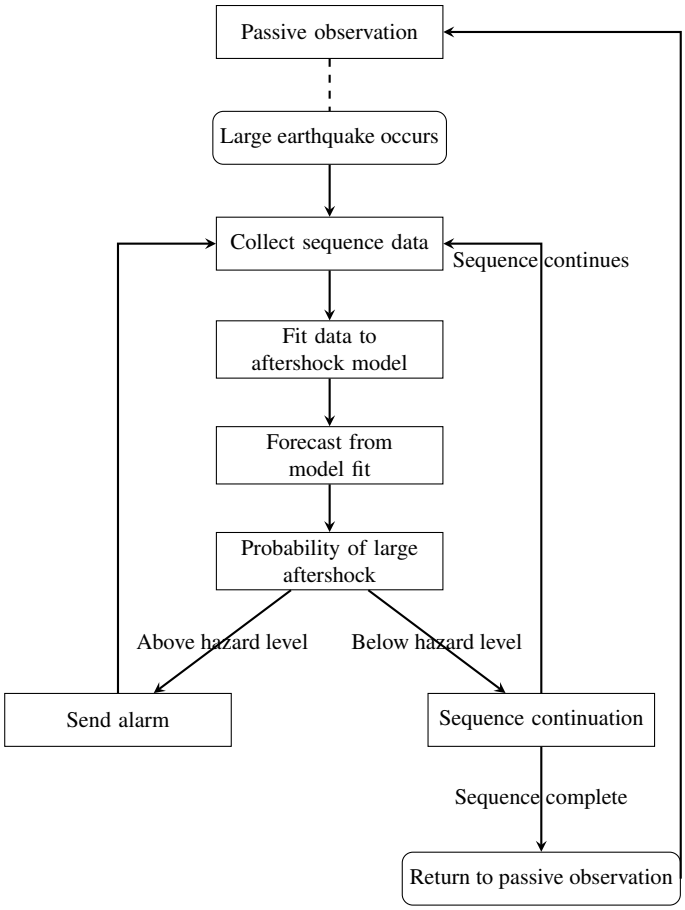

Figure 1.2: Visual representation of an example workflow starting from a large event leading to issuing an alarm. As an example, the alarm can be directed to either a group of scientists who inform the government and choose how to deliver the information to the public, or automatically to the public with suggestions for immediate earthquake preparation response.

In practice, the point parameter estimates of the models solved using the maximum likelihood estimate (MLE) method are often directly used for the forecasting procedures directly to estimate the number of events and the probability of large events. The probability of large aftershocks can be estimated directly using the extreme value theory, resulting in the extreme value distribution (EVD). For the MOL and CMOL, it is possible to directly compute the probability of events above a certain magnitude using the Reasenberg-Jones Model or using extreme value theory [Campbell, 1982, Reasenberg and Jones, 1989, Daley and Vere-Jones, 2003, Page et al., 2016, Hardebeck et al., 2019]. The direct estimate is not appropriate for the ETAS model and the probability of large events can be estimated from

simulating the ETAS model during the forecast time period. The BPD was introduced for forecasting to incorporate uncertainties in the model parameter estimates. The forecast produced by the BPD uses MCMC sampling and prior information from the MLE estimate. The complete algorithm for the BPD forecast is provided in [Shcherbakov et al., 2019].

While the MOL is the primary model used for forecasting, there has been a transition and shift towards using the ETAS model as the proposed model for real-time forecasting. For example, the ETAS can be implemented for alarm based systems such as the USGS, which currently applies the ETAS model on demand [N/A, 2020]. It is generally accepted that the ETAS model is more flexible and suitable to fitting earthquake sequences in comparison to the MOL. In addition, the ETAS model encompasses the MOL and can mimic the behaviour of the MOL. Thus, it is reasonable to see a shift towards integrating the ETAS models into real-time forecasting.

1.3.8 Testing Forecasts

When comparing different models for forecasting purposes, the forecasting ability of these models can be tested. The CSEP has implemented testing of submitted models in testing centers for specific regions such as the Regional Earthquake Likelihood Models projects in California, New Zealand, Japan, and Italy [Jordan, 2006, Schorlemmer et al., 2007, Marzocchi and Lombardi, 2009, Nanjo et al., 2012, Ogata, 2017]. The tests used by the CSEP can be adapted for testing specific forecasts and can be considered benchmark requirements in showing a model's forecast value.

Forecasts presented in terms of probabilities can be tested statistically [Kagan and Jackson, 1995]. To evaluate the forecasts produced by the forward simulation of a parameterized model, the likelihood function can be solved and relative likelihood scores can be compared [Schorlemmer et al., 2007]. Earthquake features that affect the likelihood were investigated in [Kagan, 1991]. Other investigations on likelihood methods in the temporal domain were investigated in previous studies [Vere-Jones and Ozaki, 1982, Ogata, 1983, Ogata and Katsura, 1986].

1.4 Selected Case Studies

A brief overview on the selected sequences is provided below. Five sequences were selected for forecasting analysis in this study. These include the 2009 L'Aquila sequence and 2016 Amatrice sequence in Italy; the 2016 Kumamoto sequence in Japan; the 2010 Darfield sequence and associated 2011 Churchfield events in New Zealand; and, the 2020 Monte Cristo Range (MCR) sequence in the United States of America. The case studies were selected based on previous work and suitability to the methods applied. The catalogs for the selected works are fairly complete and are from typically seismic regions across the world. The sequences took place within the last 13 years with good coverage and catalog completeness. All of the sequences have published examples of the ETAS model fitting with the exception of the MCR sequence.

The MCR sequence took place during the period of this study [Morton et al., 2020]. With a mainshock of $M_w = 6.5$, the sequence was prolific and continued for over a year. This behaviour was similar to the other, previously studied sequences with the mainshock magnitude and the productivity. The MCR sequence is analyzed in the same manner to see if the methods provide similar results to this newer sequence. In addition, the MCR is the first sequence near the border of Nevada and California that has taken place in the past 50 years in a typically aseismic region [Rogers et al., 1991, Zheng et al., 2020].

1.5 Thesis Overview

In this chapter, an overview of earthquake modelling and forecasting with associated techniques was presented. Specific earthquake models and sequences with previous forecasting examples were described. Testing of forecasts with associated literature were provided briefly in Chapter 1. The methods and data used in this work will be described in Chapter 2. Details regarding the model parameters, model parameter estimation methods, forecasting methods, and tests applied to the forecasts will be provided. The models used include the GR law to describe the frequency-magnitude statistics, and the MOL, CMOL, and ETAS model to describe

the aftershock rates. The model parameters are estimated using both the MLE method and MCMC methods. From the model parameter estimation, the probability of large aftershocks is forecasted using the EVD and BPD methods where applicable. Five statistical tests are applied to the forecasts.

The results of individual case studies using methods proposed in Chapter 2 are applied to the five earthquake sequences in different tectonic settings and are presented in Chapter 3 using retrospective testing. The forecasts for the probability of large aftershocks and forecast test performance are shown for the MOL and ETAS model for each sequence. The CMOL results are provided where available. Intermediate steps are compared to previous works to demonstrate similarity or to note differences.

In Chapter 4, the results of the model and method comparisons and forecast test performance are discussed. The results indicate that the ETAS model performed better than the MOL and CMOL for most of the case studies and training time intervals considered. However, the MOL was not rejected as an alternative hypothesis. The CMOL was not found to bring value in the forecasts and forecast performance. The relative forecast performance of the competing models indicates that the performance is also dependent on the magnitude completeness of the catalog. Some assumptions and potential limitations of this thesis are also addressed in Chapter 4. In Chapter 5, a summary of the previous chapters and suggestions for future work are provided.

Chapter 2

Data and Methods

2.1 Data

The data used in this study were acquired in the form of catalogs ("datasets"). Catalogs consist of a list of earthquake events for a specific area in chronological order and include details, such as the magnitude, date, time, latitude, longitude, and depth estimates of the events. Additional details, such as estimation methods, the source of the data, and closest recording station to the event may be listed in the original catalog. Following acquisition, the catalogs are formatted in the manner as shown in Table 2.1 where each line of the catalog is one event listing. These are listed in order as year, month, day, hour, minute, seconds, latitude, longitude, magnitude, and depth of the event. Unless otherwise specified, it is assumed that the event listings are of the best calculated hypocenter location. The catalogs used in this study are publicly available for download via an Application Programming Interface (API) or direct user interface with optional filters. The location of each study sequence is indicated in Figure 2.1.

Table 2.1: Excerpt of the JMA catalog used for the 2016 Kumamoto sequence analysis.

year	month	day	hour	min	sec	latitude	longitude	magnitude	depth (km)
2016	4	14	21	26	34.43	32.7333	130.8052	6.5	11.39
2016	4	14	21	28	11.92	32.6667	130.7405	4.1	9.77
2016	4	14	21	28	52.38	32.7167	130.7716	3.4	9.25
2016	4	14	21	28	58.03	32.7333	130.7876	3.5	11.5
2016	4	14	21	29	15.59	32.75	130.8264	3.4	13.59

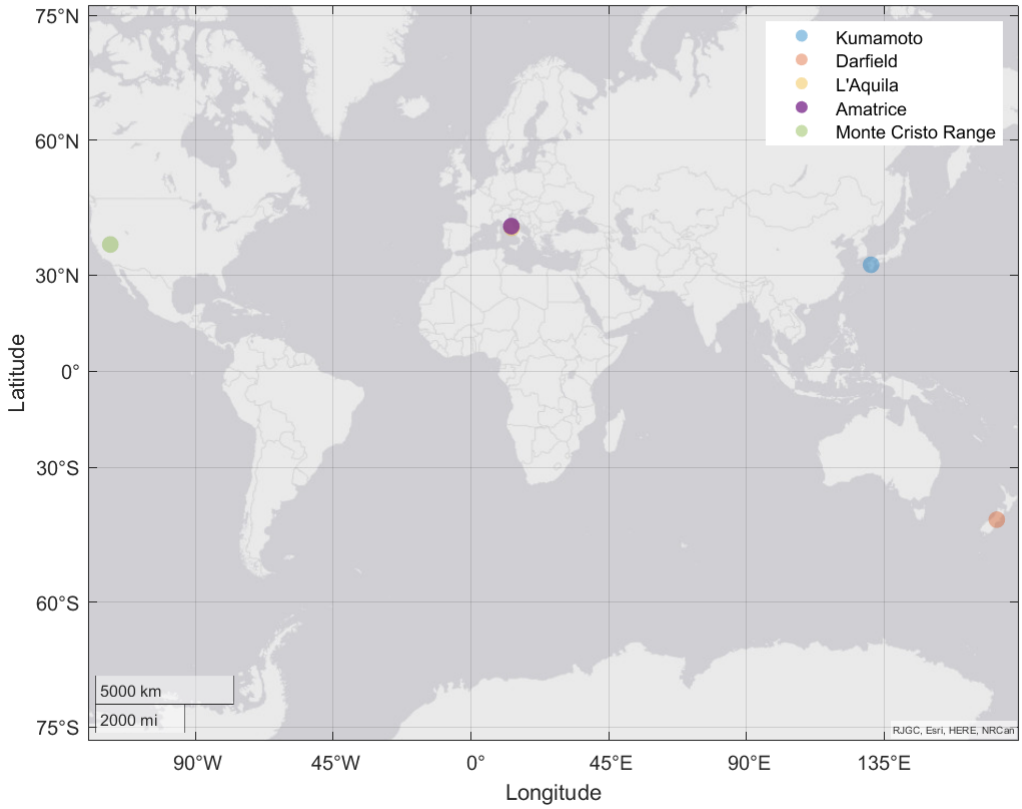

Figure 2.1: World map with the epicenters of the mainshocks of the five case studies denoted on the map. The L'Aquila sequence and the Amatrice sequence mainshocks overlap each other on the map.

2.1.1 Italian Catalog - ISIDe

The Italian Seismological Instrumental and Parametric Data-Base (ISIDe catalog) was used for the 2009 L'Aquila sequence and 2016 Amatrice sequence. The ISIDe catalog magnitudes are reported in local magnitude M_L. The ISIDe catalog is complete to as low as $M_L = 2.0$ and shows a marked improvement following upgrades to the network after April 16, 2005 [Schorlemmer et al., 2010, Lombardi and Marzocchi, 2010b]. The improvement in the catalog does not impact the analysis in this study. The catalog can be found at http://terremoti.ingv.it/en/iside and is provided by the Istituto Nazionale di Geofisica e Vulcanologia.

2.1.2 Japanese Catalog - JMA

The Japanese Meteorological Agency (JMA) catalog was used for the 2016 Kumamoto sequence. Data are available in updated form on the JMA website up until 2018 as of the download date (https://www.data.jma.go.jp/svd/eqev/data/bulletin/eqdoc_e.html). The JMA magnitude is provided in M_{JMA}. An evaluation of the automatic hypocenter estimates which contribute to the bulk of the catalog can be found in [Tamaribuchi, 2018] which improves on the method implemented in 2016. For the Kumamoto sequence, event depth restriction was adjusted to a maximum of 20 km following [Shcherbakov et al., 2018].

2.1.3 United States of America Catalog - ComCat

The United States Geological Survey Advanced National Seismic System Comprehensive Earthquake Catalog (USGS ANSS ComCat or ComCat) was used for the 2020 Monte Cristo Range (MCR) sequence. A specific sub-catalog was created by querying the ComCat API for the MCR sequence. The events in the catalog are available at https://earthquake.usgs.gov/earthquakes/search/.

2.1.4 New Zealand Catalog - GeoNet

The GeoNet catalog from the New Zealand GeoNet project was used to analyze the 2010 Darfield sequence and the later 2011 Christchurch earthquakes, large aftershocks part of the Darfield sequence. The catalog was retrieved from the Quake Search function https://quakesearch.geonet.org.nz/. The depth parameter for this catalog when performing analysis was unrestricted as all events within the elliptical area of study were shallow earthquakes. The magnitudes in this catalog are provided in M_L.

2.2 Methods

A high level view of the workflow for this study is presented in Figure 2.2. First, a catalog of interest that contains the sequence data was downloaded and formatted into a standard format suitable for further processing. The data were then filtered to be of at most 30 km depth

unless otherwise noted. The catalog was further refined by the sequence region and magnitude completeness M_c of the catalog. The region of the sequence was indicated by an ellipse that encircled the events of the sequence. The M_c within the region was initially guided by the reported completeness for the catalog if available. Then, a visual inspection of the frequency-magnitude plot was used to check and adjust the M_c. Subsequent processing used events with a selected magnitude cutoff $M_0 \geq M_c$. The catalog was then divided into the training time interval, which was used to fit model parameters, and the forecasting time interval, which was used to forecast events.

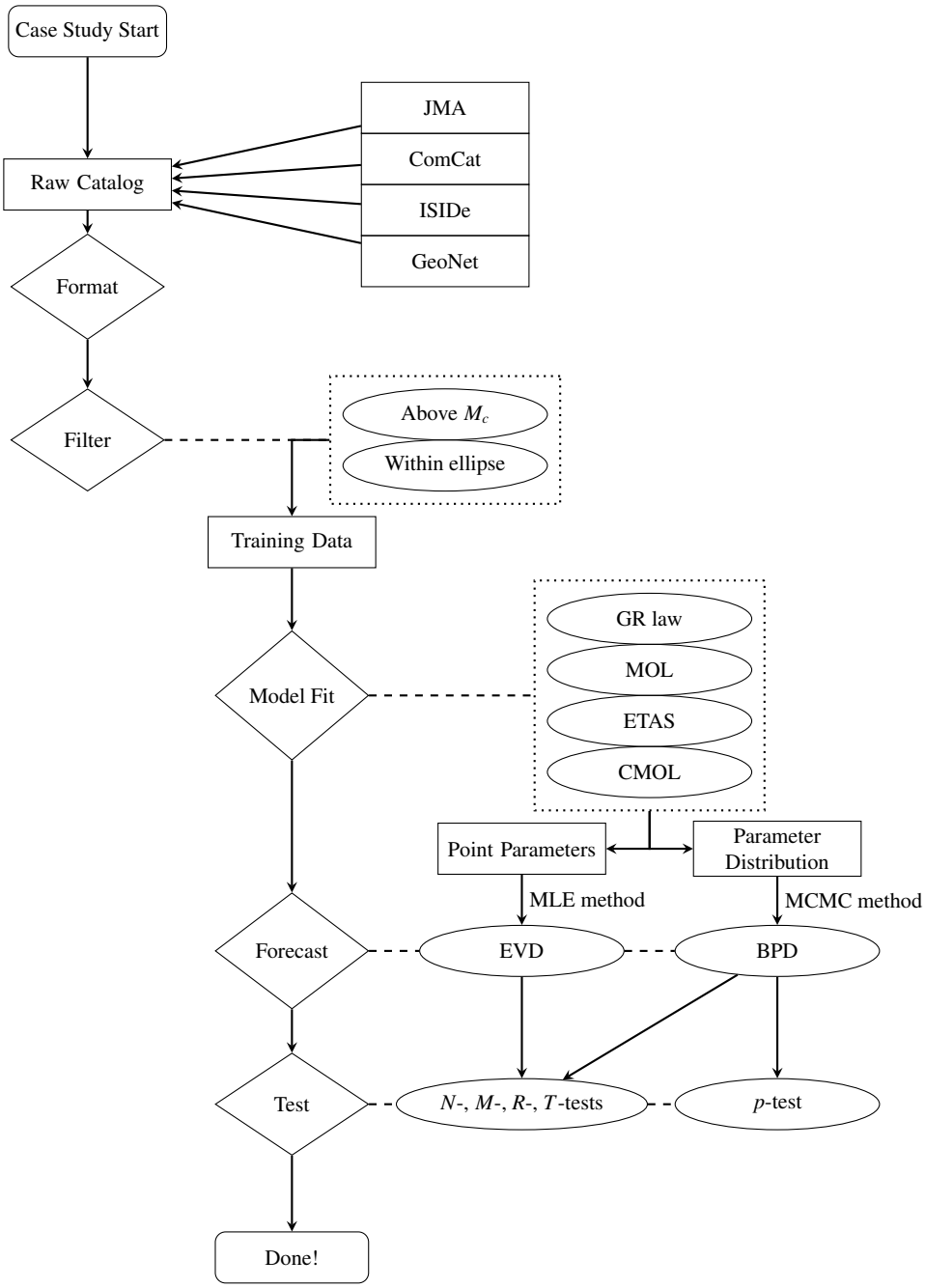

Figure 2.2: Methodology flowchart. Earthquake event data was collected in the form of catalogs and reduced to events with magnitude $M \geq M_c$ and within the user defined the ellipse. The magnitude cutoff M_c was determined by visual inspection of the GR law applied to three days of events following the mainshock. The resulting data was used to train different model types to solve for MLE point parameter estimates. The MCMC parameter distribution was estimated using the MLE results as the Gamma prior means. The parameter estimates were used to forecast the probability of large aftershocks using either the EVD or BPD during the forecasting time period. Statistical tests were then applied to the forecasts and the performance of the models were evaluated.

For each training time interval $[T_0, T_e]$, the Gutenberg-Richter (GR) law was fitted for the training period using the Maximum Likelihood Estimate (MLE) method to describe the magnitude population for the training interval. The magnitude population as described by the GR law parameters were assumed to represent event magnitudes during the forecasting time interval (Sections 2.2.3 and 2.3). Up to three different aftershock models were fitted to the same training period using the MLE to estimate the aftershock rate parameters in addition to the GR law parameters. The aftershock models used in this work included the modified Omori law (MOL), compound Omori law (CMOL), and the Epidemic Type Aftershock Sequence (ETAS) model (Section 2.4). Using the point parameter estimates from the MLE method as mean values and prior information, Markov Chain Monte Carlo (MCMC) sampling was applied to the same training time interval to produce model parameter distributions and were recorded as chains (Section 2.5).

The point parameter estimates for the MOL and CMOL were used to directly calculate the probability of large events during the forecasting time period $[T_e, T_e + \Delta T]$ using extreme value theory (EVD) method [Shcherbakov et al., 2019]. In addition, for all of the aftershock models, the MCMC chains were used to forward simulate the sequence in time as an ensemble for the duration of the forecasting time period. The simulations were used to compute the probability of large aftershocks during ΔT. The sampling algorithm used to produce the MCMC chains accounts for the uncertainty in the model parameter estimates and uses Bayesian methods to incorporate prior knowledge from the MLE estimates. This results in the Bayesian predictive distribution (BPD) method [Shcherbakov et al., 2019, Shcherbakov, 2021] (Section 2.6).

Lastly, five statistical tests were applied to the forecasts produced by the EVD and BPD methods. Each test compared the forecasted events to the observed events during the forecasting time period for specific characteristics. These tests were applied for the early aftershock training periods of each sequence, model, method for model fitting, and forecasting method where applicable (Section 2.7). All analyses as described in this chapter were done using MATLAB with code provided by Robert Shcherbakov and modified by Elisa Dong.

2.2.1 Model Training Time Intervals

The model parameters were estimated during the training time period as shown in Figure 2.3. The training time period $[T_0, T_e]$ consists of two components, the preparatory time interval $[T_0, T_s]$ and the target time interval $[T_s, T_e]$. The preparatory time interval provides a short time interval where the events in the catalog are not included in the model parameter fitting procedure for the MOL and CMOL. This bypasses some of the issues with fitting that are impacted by potentially missing data close to the mainshock. For the ETAS model, the preparatory time interval is used to condition the model parameter estimates. For each sequence and aftershock model used, the preparatory time interval remains the same for all training time intervals. The model parameter estimates take place over the target time interval.

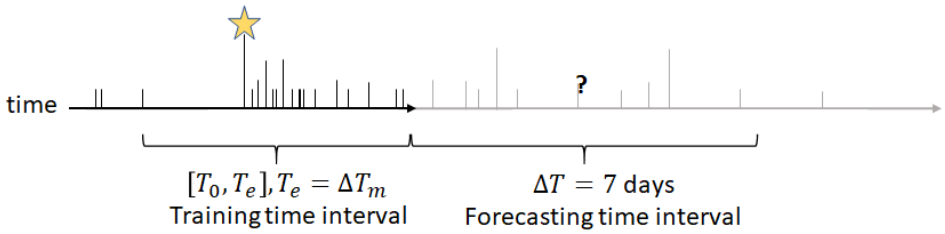

Figure 2.3: Timeline of events during an earthquake sequence. The preparatory time interval $[T_0, T_s]$ can be used to condition the ETAS model (T_s is typically the time of the mainshock, or shortly after). The model is fitted over the training time interval $[T_0, T_e]$, where T_e is typically provided in number of days following the mainshock, ΔT_m. The forecasting takes place during $[T_e, T_e + \Delta T]$.

To simulate real-time forecasting, the training time interval is typically aligned with the first identified "mainshock" that produces a notable aftershock sequence. The first target time interval ends a full day ($T_e = 1$) after the mainshock. To capture the evolution of the sequence, the start of the training time T_0 is fixed as the T_e is progressively increased in increments of 24 hours up to seven days. Additional training time periods are considered for each case study. In this work, the number of "training days", ΔT_m, is always made in reference to the number of days following the mainshock unless otherwise noted. For example, Sequence A is preceded by a foreshock sequence. The ETAS model and the CMOL can be trained starting at T_0, where T_0 is the time of the first large foreshock. The foreshock sequence is 3.5 days long. One training

day for Sequence A, $\Delta T_m = 1$, has a training time interval $[0.0, 4.5]$. The MOL is fitted to Sequence A beginning with T_0 at the time of the mainshock. For the MOL, the training time interval is $[0.0, 1]$ for $\Delta T_m = 1$. For all of the target time intervals, if T_0 is the time of the mainshock, then T_s is a short time such as 0.002 to 0.03 days after the mainshock.

The forecasting time period $[T_e, T_e + \Delta T]$ immediately follows the training time interval (Fig. 2.3). Model parameter estimates produced using the training time interval are used to simulate and forecast for large aftershocks during the forecasting time interval. The forecasted events can be compared with the observed events in the catalog. In this work, the length of the forecasting time interval was set to seven days, $\Delta T = 7$.

2.2.2 Model Region Selection

A large magnitude event can have an estimated fault length based on an empirical relationship and region of influence [Utsu and Seki, 1955, Wells and Coppersmith, 1994, Kagan, 2002]. In this study, it is assumed that the spatial distribution of the sequence can be restricted to events that fall within a user-defined ellipse. This ellipse is selected by reviewing the early aftershocks by including most events during the early aftershock sequence, and may use knowledge of the location of fault or faults. Event data up to three days after the main event were used to identify the extent of the aftershocks. All events captured within the ellipse and above the selected magnitude cutoff M_0 were used in subsequent analysis. Forecasted events also occur within the same region used for training.

2.2.3 Magnitude Completeness Analysis

The magnitude completeness indicates at which magnitude the events in the sequence are considered to be complete in the catalog. It is assumed in this work that the magnitude distribution of earthquakes follows the GR law [Gutenberg and Richter, 1944]. Based on this premise, most of the events taking place during a sequence will be of low magnitude. If many of these smaller events are missing from the catalog when training, this may bias the subsequent aftershock rate analysis. In addition, M_c typically increases temporarily after a

large shock. Some reasons include instrument saturation and the presence of coda waves [Aki, 1969, Kagan, 1991, Shebalin et al., 2011]. Thus, it is important to find the magnitude completeness where the data is deemed sufficiently complete for further analysis. However, it is also important to not select too high a value for M_c as doing so reduces the amount of data available for training. In particular, the ETAS model tends to underestimate the number of events during a forecast when using high M_c and the productivity from small events is not accounted for [Helmstetter and Sornette, 2003].

M_c was assessed on a sequence by sequence basis. After acquiring the catalogs, the first three days of data following the first large shock in the elliptical region were selected. The events were plotted onto a log-log plot of frequency-magnitude of the events. If the GR law is an accurate representation of the frequency-magnitude relationship, then the events should fall along a straight line on the log-log plot. When the lower magnitude events start falling below the straight line, this indicates that the GR law does not hold in the magnitude range below the deviation and events are missing. Other methods for selection can be found in the following studies [Rydelek and Sacks, 1989, Woessner and Wiemer, 2005, Mignan et al., 2011, Agnew, 2015].

The magnitude cutoff M_0 is a similar value that the user can select to limit the data available in the catalog to restrict the analysis to events above M_0, where $M_0 \geq M_c$. The choice of higher M_0 may affect the GR law model parameter estimation and the productivity parameters of the rate models. M_0 may affect the α parameter of the ETAS model, which is a productivity parameter that indicates if the sequence is more swarm-like or if the aftershock behaviour is dominated by the mainshock. In this study, $M_0 = M_c$ with the exception of the Darfield sequence.

2.3 Gutenberg-Richter Law

The Gutenberg-Richter Law is an empirical power law that describes the frequency and magnitude of earthquakes [Gutenberg and Richter, 1944]. Assuming that the GR law is applied

to a complete catalog, then the GR law parameters can also be used to sample the magnitude of forecasted events. The GR law can be represented by the left-truncated exponential distribution

$$\log_{10} N = a - b(M - M_0) \tag{2.1}$$

where N is the number of events, b-value is a scaling parameter, and a is a constant. A larger b-value results in a steeper slope on the plot relating the log number of events and the magnitude of the events. This corresponds to a relatively small number of large magnitude events in comparison to a smaller b-value.

The standard deviation for the b-value is provided by [Bender, 1983] and the standard error for the estimation method is provided in [Shi and Bolt, 1982]. The estimation of the b-value error due to binning for a confidence interval follows the procedure in [Tinti et al., 1987].

Equations

$$f_\theta(m) = \beta \exp[-\beta(m - m_0)], \tag{2.2}$$

$$F_\theta(m) = 1 - \exp[\beta(m - m_0)], \tag{2.3}$$

are the probability and cumulative density functions for the GR law, respectively [Vere-Jones, 2010]. The model parameter for the GR law is described by $\theta = \{\beta\}$, where β is related to the b-value by $\beta = \ln b$. θ provides the magnitude population to draw upon during the forecasting time period.

2.4 Temporal Seismicity Rate Models

Three aftershock models are used in this study, the MOL, CMOL, and the ETAS model. The rate is described by λ_ω and the aftershock rate model parameters are represented by ω.

2.4.1 Modified Omori Law

A decay in seismicity rate following a large shock can be described with the empirical modified Omori law [Omori, 1894, Utsu, 1961]. The functional form of the rate model is

$$\lambda_\omega(t) = K_0/(t + c_0)^{p_0}, \tag{2.4}$$

where t is the time relative to the beginning of the target time interval. The model parameters for the MOL are $\omega = \{K_0, c_0, p_0\}$. K_0 parameter describes the aftershock productivity rate of the sequence with respect to the mainshock. The productivity rate K_0 is dependent on M_0. The seismicity rate decays in inverse fashion as controlled by the decay parameter p_0. c_0 is a short time delay following the mainshock before the decay of the aftershock rate begins. Further reading on the parameters with respect to the magnitude cutoff can be found in studies by [Utsu et al., 1995, Shcherbakov et al., 2004, Lippiello et al., 2007].

2.4.2 Compound Omori Law

In the case where an earthquake sequence has two distinct Omori-like aftershock sequences that overlap each other, the CMOL can be applied. The CMOL consists of two instances of the MOL which take place at different times. The functional form of the CMOL is written as

$$\lambda_\omega(t) = \frac{K_1}{(t + c_1)^{p_1}} + H(t - \tau)\frac{K_2}{(t - \tau + c_2)^{p_2}}. \tag{2.5}$$

The aftershocks from the first MOL instance can continue to contribute to the seismicity rate following the second MOL instance. The model parameters are $\omega = \{K_1, c_1, p_1, K_2, c_2, p_2\}$ where t is the time after the first large shock and τ is the time of the second large shock. The Heaviside step function $H(x)$ is equal to one when $x \geq 0$ and is zero when $x < 0$. $H(x)$ controls when the second instance of the MOL will contribute to the seismicity rate. τ indicates when the second instance of the MOL begins. The model parameters for the CMOL provide similar representations as they do in the MOL function, with two instances of the MOL contributing

to the total seismicity rate.

When the sequence has a distinct foreshock sequence, τ can be set to the time of the mainshock. Otherwise, τ is set to a user defined time associated with a large magnitude event that is not necessarily the largest event during the aftershock sequence following the mainshock.

2.4.3 ETAS Model

The ETAS model represents seismicity by means of a trigger-model, where each parent event in the sequence produces its own Omori-like aftershocks. The functional form of the ETAS model is described as

$$\lambda_{\omega}(t|H_t) = \mu + \sum_{i:t_i<t} \frac{e^{\alpha(m_i - m_0)}}{\left(\frac{t-t_i}{c} + 1\right)^p}. \tag{2.6}$$

The model parameters for the ETAS model are $\omega = \{\mu, K, c, p, \alpha\}$ and conditioned over the history H_t of events during the time interval $[T_0, t]$. For the ETAS model, the background seismicity rate μ is explicitly taken into account. μ is a constant rate prior to and during the sequence, and is associated with seismicity from tectonic loading and can be modelled using a homogeneous Poisson process [Ogata, 1998]. t is the time relative to the beginning of the target time interval, and t_i is the time of each event relative to the beginning of the target time interval. The model parameters $\{K, c, p\}$, which provide a similar function to $\{K_0, c_0, p_0\}$ in the MOL, describe the aftershock decay for short-term triggering effects in the ETAS model [Lombardi and Marzocchi, 2010b]. The c and p values are time based parameters, where c is the same short time delay for each parent event triggering a Omori-like aftershock sequence, and p describes the rate of decay for each local cluster. K and α are productivity parameters associated with each individual event in the sequence. K describes the aftershock productivity after each event in the sequence and α describes the efficiency of aftershock activity generation by a shock of a certain magnitude. The productivity value α indicates how large the contribution to the productivity from event m_i will be. If α is small, then the ETAS model describes swarm-like behaviour. If α is large, then the ETAS model describes Omori-like behaviour.

2.5 Model Parameter Fitting

The model fitting takes place over the training time interval. In this work, two different parameter estimation methods were applied.

The first parameter estimate method uses the MLE method. The MLE produces specific point parameter estimates for θ and ω based on the training time interval. When using the MLE method, it is assumed that the catalog being fitted over a complete and homogeneous for the time periods under consideration [Kagan and Jackson, 1995, Zhuang et al., 2012]. The likelihood functions are further elaborated in Appendix A.

The second method for estimating parameters uses a Markov Chain Monte Carlo (MCMC) method. This method produces chains of point parameter estimates from each sampling step as part of the method. By sampling the potential model parameters, the MCMC method results in a distribution for each model parameter, thus accounting for the uncertainty in the estimates. This method accounts for the stochasticity of the ETAS model better than that of a single point parameter representation from the MLE method.

2.5.1 Maximum Likelihood Estimate

To estimate θ and ω, the log-likelihood function is maximized. The point parameter estimation for the GR law requires additional steps as the magnitudes in the catalog are binned. In this study, the data is typically binned in $\Delta M = 0.1$ intervals. θ can be solved using the MLE method for magnitudes exceeding M_0 [Utsu, 1965, Aki, 1965, Guttorp and Hopkins, 1986].

The likelihood is the probability of observing the aftershocks within the training time period given the model and the parameter estimate [Ogata, 1983, Hardebeck et al., 2019]. For the likelihood with a time-dependent rate as with the ETAS model, see [Daley and Vere-Jones, 2003, Shcherbakov et al., 2019]. The log-likelihood is maximized using all events within $[T_s, T_e]$ for the MOL and CMOL, and $[T_0, T_e]$ for the ETAS model, above M_0 and above the maximum depth for the sequence. The MLE is solved using the MATLAB fmincon() function, by minimizing the negative log-likelihood function

https://www.mathworks.com/help/optim/ug/fmincon.html. Additional details are available in Appendix A.

In some cases, the ETAS model parameter estimation may be unstable over the varying training time intervals. To improve parameter stability, it is possible to fix some of the parameters to specific values during estimation. This is useful when catalogs of low magnitude events dating back several years are available and the background seismicity rate appears to be low leading up to the earthquake sequence. In those cases, μ can be fixed to an extremely low value or $\mu = 0$ and the model parameter does not need to be solved for.

Errors for the point parameter estimate using the MLE method for the aftershock models are calculated using the inverse Fisher information matrix [Ogata, 1983, Ogata, 1978], which can be derived from the Hessian. In this work, the Hessian is a byproduct of the fmincon() solution when using MATLAB. The MOL and ETAS model inverse Fisher information matrices were computed directly.

2.5.2 Markov Chain Monte Carlo Chains

To better describe the model parameter distributions, the MCMC method was used with the sampler proposed by [Shcherbakov, 2021]. Each random sampling produces a set of parameter estimates that is then saved as part of a chain. From the previous sampled step, the chain progresses by taking another step in an arbitrary direction in the parameter space. 100,000 steps are discarded for "burn-in" and 100,000 steps are sampled for the parameter estimates so the distribution only represents the latter portion of the steps. This is based on the procedure in [Shcherbakov et al., 2019, Shcherbakov, 2021]. The results of the chain can be used to forward simulate as an ensemble for forecasting. The large number of steps was needed to produce a smooth distribution for the forecast probabilities.

Several variations of MCMC methods are available. The method in this study uses the Metropolis-Hastings algorithm for the MOL and CMOL and Metropolis-within-Gibbs sampling algorithm for the ETAS model for the posterior distributions of the ETAS model parameters [Shcherbakov et al., 2019]. The initial model parameter estimates θ and ω from the MLE

are used as the mean for the Gamma priors. Since the sampling method accounts for the prior knowledge, forecasts produced from the MCMC parameter estimates result in the BPD.

For the ETAS model, the parameter estimates are updated using both the Metropolis-Hastings sampler and the Gibbs sampler [Shcherbakov et al., 2019]. The sampling process samples one parameter while all other parameter values are fixed. The Gibbs sampler is used to generate random variables from the Metropolis-Hastings sampling [Shcherbakov et al., 2019]. The ETAS model proposal distribution follows a log-normal distribution.

2.6 Forecasting Methods

Two forecasting methods were used in this study. The first uses the model parameter estimates from the MLE, which can be directly input into the function described by the EVD for the MOL and CMOL. While the EVD for the ETAS model can be produced via simulation, the EVD does not account for the uncertainty in the parameter estimates and nature of the ETAS model, where slightly different model parameters may result in significantly different number of forecasted events during the forecating time period. To include the uncertainties in the model parameters, the BPD was used as the second forecasting method for all of the aftershock models.

The forecasts produced the probability of large magnitude earthquakes occurring during the forecasting time period for $\Delta T = 7$ days following the target time intervals. For each sequence, the probability of the forecasted sequence containing at least one event above the magnitude M_{ex} was calculated.

2.6.1 Extreme Value Distribution

The point parameter estimates from the MLE can be directly used to estimate the probability of large events during the forecasting time period with

$$P_{EV}(m_{ex} > m|\theta, \omega, \Delta T) = 1 - \exp\{-\Lambda_{\omega}(\Delta T)[1 - F_{\theta}(m)]\}. \tag{2.7}$$

For the MOL and CMOL models, it is assumed that individual earthquake events are independently and identically distributed and are a nonhomogeneous Poisson process which can then be directly estimated using the Gumbel distribution

$$P_{EV}(m_{ex} > m|\theta, \omega, \Delta T) = 1 - \exp\{-\Lambda_\omega(\Delta T)\exp[-\beta(m - m_0)]\}, \tag{2.8}$$

[Shcherbakov et al., 2019]. The productivity Λ_ω is the number of events produced during the time interval ΔT. Λ_ω for the MOL and CMOL can also be written explicitly with equations

$$\Lambda_\omega(\Delta T) = K_0\frac{(T_e + c_0)^{1-p_0} - (T_e + \Delta T + c_0)^{1-p_0}}{p_0 - 1}, \tag{2.9}$$

$$\begin{aligned}\Lambda_\omega(\Delta T) = &+K_1[(T_e + c_1)^{1-p_1} - (T_e + \Delta T + c_1)^{1-p_1})/(p_1 - 1)] \\ &+K_2[(T_e - \tau_m + c_2)^{1-p_2} - (T_e + \Delta T - \tau_m + c_2)^{1-p_2})/(p_2 - 1)],\end{aligned} \tag{2.10}$$

respectively [Shcherbakov, 2021]. Then, the probability of an event during forecasting time period ΔT above magnitude m_{ex} in Equation 2.8 is directly estimated by providing parameters θ and ω for the MOL and CMOL by replacing Λ_ω with either Equation 2.9 or Equation 2.10.

The productivity of the ETAS model can be found in [Shcherbakov et al., 2019]. However, the direct calculation of the productivity is not suitable for the ETAS model. Unlike the MOL, the ETAS model simulation depends on the past history. Thus, for the ETAS model, the EVD is generated from many simulations of the ETAS model using the parameter values. For forecasting the largest aftershock, the ETAS model can be forward simulated during the forecasting time period following the thinning method [Ogata, 1981, Ogata, 1998, Zhuang et al., 2004]. The largest magnitude from each simulation is extracted and the distribution of all the largest magnitude events results in the estimation of the EVD [Renard et al., 2013, Shcherbakov, 2021]. The EVD following this method for the ETAS model deviates from the Gumbel distribution [Shcherbakov et al., 2019]. Since the EVD uses only one set of model parameter estimates to produce a forecast, the EVD was not directly applied to the ETAS model.

2.6.2 Bayesian Predictive Distribution

The extreme value framework can be used to derive the BPD, as shown in

$$P_B(m_{ex} > m|\mathbf{S}, \Delta T) = \int_{\Omega}\int_{\Theta} P_{EV}(m_{ex} > m|\theta, \omega, \Delta T)p(\theta, \mathbf{S})d\theta d\omega, \tag{2.11}$$

[Shcherbakov et al., 2018, Shcherbakov, 2021]. Unlike the EVD, the BPD accounts for uncertainty of the parameter estimates. Explicitly, the BPD is the multi-dimensional integral of the EVD multiplied by the posterior distribution over the parameters of the frequency-magnitude domain and the model rate parameters [Shcherbakov et al., 2018]. The probability of an extreme event from the P_{EV} is used with the posterior distribution function and integrated over the parameter space, resulting in P_B. The posterior distribution can be described by

$$p(\theta, \omega|\mathbf{S}) \propto L(\mathbf{S}|\theta, \omega)\pi(\theta, \omega), \tag{2.12}$$

which is proportional to the prior distribution π and the likelihood function based on the training data [Shcherbakov et al., 2019]. The posterior distribution provides constraints on the model parameter variability by using prior information and information obtained from the training data via the likelihood function. The prior distribution is represented by a Gamma distribution [Zhuang et al., 2012, Shcherbakov et al., 2019]. The proposal distributions $J(x|\tilde{x})$ are set so that the parameters can only be positive and are chosen to approximate the posterior distribution [Shcherbakov et al., 2019]. $J(x|\tilde{x})$ is incorporated in the Metropolis-Hastings algorithm during the model sampling procedure as log-normal distributions.

In practice, to compute P_B, the posterior distribution $p(\theta, \mathbf{S})$ is sampled using the MCMC method to produce a chain of parameters which accounts for the uncertainty in the parameter estimates. From this chain, each set of model parameters ω is forward simulated for the forecasting period.

$\mathbf{S}$ is the set of observed events during the parameter estimation time period. The probability of an event during forecasting time period ΔT above magnitude m_{ex} is integrated over the

possible parameter ranges of the frequency-magnitude distribution Θ and the parameter ranges of the earthquake rate model Ω (Eqn. 2.11).

2.7 Statistical Tests

Hypothesis testing assumes that there is a null hypothesis which an alternative hypothesis is being tested against. Either the null hypothesis will be rejected in favour of the test hypothesis, or the null hypothesis is not rejected. When the null hypothesis is not rejected at a specified significance level, then the test hypothesis does not perform better than the null hypothesis [Schorlemmer et al., 2007].

The forecast itself is a vector of earthquake rates in the corresponding magnitude and temporal bins [Schorlemmer et al., 2007]. From the forecast vector, the number of predicted events for each of the bins is calculated to produce a vector of expectations. For each bin, the probability of observing events in the bin is the Poisson probability. The joint log-likelihood is the sum of all the logs of the likelihoods in each bin when comparing the expectation to the observed events in each bin [Zechar et al., 2010]. The joint log-likelihood value produces the score on the likelihood test (L-test). A higher value suggests that the forecasted and observed events agree better [Schorlemmer et al., 2007]. To account for uncertainty, the likelihood test (L-test) can be conducted by simulating the observed events. In this study, the L-test score is not produced as L-test can be divided into the N-test (testing the rate forecast) and the M-test (magnitude test) [Zechar et al., 2010].

To evaluate the event distributions during the forecasting time period, several specific aspects of the forecasts were tested. Features of interest may include: the likelihood of the forecast, the number of forecasted events, and the magnitude distribution of the forecasted events in comparison to the observed events. Whether the largest event in the observation is forecasted is also an interesting feature. In addition, the relative performance of the models can be compared in terms of relative likelihood and relative information gain.

In this work, the the number test (N-test), magnitude test (M-test), ratio test (R-test),

T-test [Kagan and Jackson, 1995, Rhoades et al., 2011], and the Bayesian p-test were considered [Shcherbakov, 2021]. The first four were adapted from tests used by the CSEP [Schorlemmer et al., 2007, Zechar and Jordan, 2008, Zechar et al., 2010] and the Bayesian p-test was introduced by [Shcherbakov, 2021]. For all statistical tests, effective significance levels of 2.5% and 5% were preselected as per [Taroni et al., 2018]. Values exceeding the significance level can typically be considered to result in a passing score on the test (Fig. 2.4). However, extremely high quantile scores should be interpreted with caution. Passing the test with near perfect scoring indicates that nearly all the individual forecast simulations pass the evaluation criteria. This may be unexpected considering the variation in the model parameters used for the BPD forecasting method. Quantile scores below the significance level indicate that the model has failed the test and can be rejected for the criterion it is being evaluated for. If a model fails the R-test and also fails the N- and M-tests, then the model is rejected. The T-test and Bayesian p-test provide additional context for the model performance.

2.7.1 N-Test

The N-test compares the number of events simulated during the forecasted time period to the number of observed events during the forecasting time period [Zechar et al., 2010]. Two associated quantile scores are considered for the N-test, δ_1 and δ_2. The quantile scores indicate if the generated sequences produced forecasted event numbers N_{fore} above or below the observed values N_{obs} as shown in equations

$$\delta_1 = 1 - P((N_{obs} - 1)|N_{fore}), \tag{2.13}$$

$$\delta_2 = P(N_{obs}|N_{fore}), \tag{2.14}$$

respectively. δ_1 is the probability of observing at least N_{obs} and δ_2 is the probability of observing at most N_{obs}. Both the overall forecast rate and observed number of events are assumed to be Poissonian and described by N_{fore} and N_{obs}, respectively. δ_2 describes the right-continuous Poisson cumulative distribution with the expectation N_{fore} at corresponding N_{obs} at the times

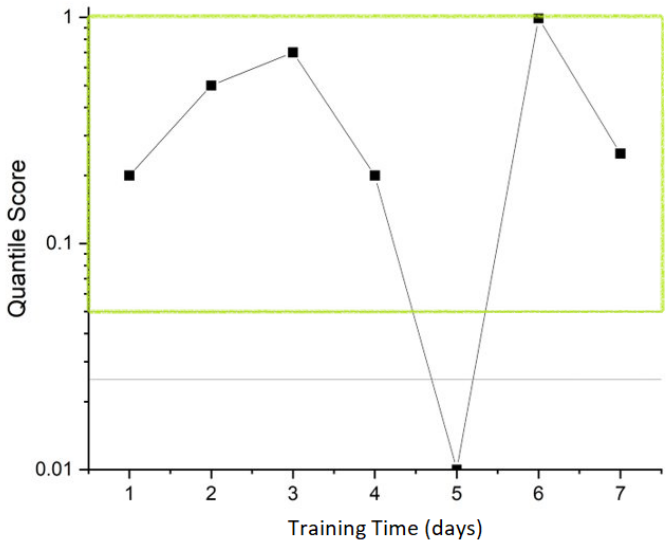

Figure 2.4: An example of the interpretation of the quantile score on a forecasting test is provided in this image. For the training time intervals ending at T_e, the performance on the forecasting test produces a quantile score q between $0 \geq q \leq 1$. Values above the effective significance level 5% fall in the region marked by the green outline. Values below the effective significance level are considered a fail on the test. The effective significance level 2.5% is also plotted on a horizontal line in the plot. In this example, $\Delta T_m = 5$ results in a very low quantile score. Thus, the model producing the forecast at the corresponding training time interval fails the forecasting test at that time interval.

evaluated. This score describes the fraction of forecast expectations smaller than the observed events. The probability that more than N_{obs} events are forecasted can be described as $(1 - \delta_2)$. The problem with this approach is addressed in [Zechar et al., 2010]. Instead, the δ_1 probability was added in addition to the original N-test to describe at least N_{obs}, in which the user only needs to be concerned about low probability values [Schorlemmer et al., 2007, Zechar et al., 2010].

For this updated N-test, the quantile scores determine whether the number of forecasted events is inconsistent with N_{obs}. A small δ_1 indicates that the forecast underpredicts the observed sequence, and a small δ_2 indicates that that the forecast overpredicts the number of events. Thus if the probabilities of δ_1 and δ_2 are smaller than the effective significance level, the forecast can be rejected [Zechar et al., 2010]. The effective significance level for the re-

spective one-sided N-tests was set to 2.5% to correspond with a single quantile score which then represents a 5% error rate for the test [Zechar et al., 2010].

The N-test performance can be interpreted by observing whether the quantile scores for δ_1 and δ_2 fall within the green region in Figure 2.4. High δ_1 scores tend to correspond to low δ_2 scores, thus it is not unusual to observe fluctuation in the scores early during the aftershock sequence and for shorter training time intervals as the model parameters and the sequence are stabilizing.

2.7.2 M-Test

The M-test evaluates the distribution of the magnitudes of the forecasted events during the forecasting time period compared to the true magnitude distribution of the observed events [Schorlemmer et al., 2007, Zechar et al., 2010]. For this test, the magnitude distribution is isolated from the number of forecasted events by normalizing the forecast such that the number of simulated events $N_{sim} = N_{obs}$ (N_{sim} is different from N_{fore}). The testing is done by computing the joint log-likelihood score of the simulated magnitude events. The M-test statistic is indicated by a κ quantile as shown in

$$\kappa = \frac{|\{\hat{M}_x | \hat{M}_x \leq M\}|}{\{|\hat{M}|\}}, \tag{2.15}$$

where M is the true joint log-likelihood of the observed event magnitudes and $\{\hat{M}\}$ is the joint log-likelihood computed for every simulation x [Zechar et al., 2010]. $|\{A\}|$ is the number of elements in the set $\{A\}$. Then, the value of κ is the number of simulations that have equal or lower joint log-likelihood than M, normalized by the number of simulations. If the quantile score falls below the significance level, the simulated magnitude distribution is inconsistent with the observed magnitude distribution.

2.7.3 *R*-Test

The *R*-test compares two different forecasting models relative to each other by assuming one of the models is true and stands in as the null hypothesis. Each of these models has a likelihood score from the *L*-test based on the modified observed events sampled assuming the null hypothesis is true. The *R*-test provides the ratio of the log-likelihoods for two models as *R*, where $R_{21} = L^2 - L^1$ [Kagan and Jackson, 1995, Schorlemmer et al., 2007]. In this case, it is assumed that the model associated with the likelihood L^2 corresponds with the correct hypothesis H^2. If $R > 0$, then model H^2 performs better. In particular, if α, the quantile score is larger, then H^2 performs better. If $R < 0$, then model H^1 performs better. For example, when comparing the MOL vs. ETAS model, where ETAS is H^2, if $R > 0$, then the ETAS model has a greater log-likelihood and performs better than the MOL. By reversing the competing hypotheses, it is possible that both models can fail the *R*-test, leading to an inconclusive test result.

2.7.4 *T*-Test

To simplify the *R*-test interpretation and to reduce computational time, the *T*-test was introduced as a proxy and supplement for the *R*-test and is inspired by the Student's *t*-test [Rhoades et al., 2011]. The results of the *T*-test indicate whether a second hypothesis has performed better than the first hypothesis and demonstrates significant information gain. The *T*-test indicates if one model is inconsistent with the reference model. The *T*-test uses the sample information gain (IG) per earthquake of one model over another, where the sample information gain for each earthquake in model 2 over model 1 is shown as $I_N(H^2, H^1)$ and N_{obs} is the number of observed events during the forecasting time interval ΔT [Rhoades et al., 2011]

$$IG(H^2, H^1) = \frac{R^{21}}{N_{obs}}. \tag{2.16}$$

The IG represents the expected value of the difference between entropy scores of the two

models. The entropy score is $-\log p_j$, where the forecast probability of outcome j for several trials is p_j [Harte and Vere-Jones, 2005]. Large and positive values of IG suggest that H^2 is the favoured model.

2.7.5 Bayesian p-Test

For forecasts that use the BPD method to generate probabilities, the Bayesian p-test can be conducted. In this work, the value p_B gives the probability that the simulated events in the sequence will be more extreme than the observed largest event during the forecasting time interval. p_B is described as

$$p_B = Pr[T(\hat{y}, \theta, \omega) \geq T(t, \theta, \omega)], \tag{2.17}$$

[Shcherbakov, 2021]. The M-test provides information on how close the magnitude distribution of the simulated forecast is to the observed events and is different than the p-test which checks for the extreme magnitude consistency.

The implementation of the Bayesian p-test (herein p-test) uses a test quantity $T(t, \theta, \omega)$ for the observed variable y and the simulated quantity $\hat{y}$ where $T(y, \theta, \omega) = max(y)$. $max(y)$ is the largest event in the simulation, and p_B is the proportion of the test quantities from the simulated maximum events that are greater than or equal to the observed largest event during the forecasting time interval. Extreme values of p_B close to 0 suggest that the features are not well demonstrated by the model [Shcherbakov, 2021]. This test was not applied to forecasts produced using the EVD.

Chapter 3

Case Studies

Five sequences were selected for analysis using the methods presented in Chapter 2 with a forecasting time interval of $\Delta T = 7$ days for each training time interval. The results are presented in the following manner. A description of each sequence and a summary of the previous aftershock analysis are provided for context. The Gutenberg-Richter (GR) law fit for a training time interval of $\Delta T_m = 3$ days is demonstrated for the selected magnitude cutoff of the sequence, M_0. The model parameter estimates using the maximum likelihood estimate (MLE) with corresponding errors using the aftershock rate models are provided for the training time intervals. The forecast probabilities of the largest expected earthquake produced using the Monte Carlo Markov Chain (MCMC) method and Bayesian predictive distribution (BPD) for the same training time intervals are provided. The forecast performance of the aftershock rate models using the BPD forecast method are evaluated using five statistical tests. The comparative results of the R- and T- tests are summarized briefly, then the individual aftershock rate models are evaluated using the N-,M-, and the Bayesian p- tests. Where applicable, the model parameter estimates and the forecast performance are compared to previously published works.

The results of the extreme value distribution (EVD) forecasting method for the modified Omori law (MOL) and compound Omori law (CMOL) are nearly identical to those of the Bayesian predictive distribution (BPD) method. Thus, the results of the BPD shown in this

chapter apply to the EVD forecasts unless otherwise noted. For brevity, the EVD forecasts for the largest aftershock and forecast test performance are not in shown in this chapter and can instead be found in Appendix B.

3.1 The 2009 L'Aquila, Italy, Sequence

The 2009 L'Aquila sequence began with a mainshock of $M_w = 6.3$ ($M_L = 6.1$) on April 6, 2009 at 01:32:39 UTC, resulting in the deaths of about 300 people [Chiarabba et al., 2009]. L'Aquila is in the central Apennines next to large and active normal faults where there is high seismic hazard [Woessner et al., 2015]. The deformation in this region is accommodated by the NW-SE normal fault systems [Serpelloni et al., 2005]. In the months prior to the earthquake sequence, there was increased background seismicity and what appeared to be foreshocks days before the mainshock [Papadopoulos et al., 2010]. The mainshock was a normal faulting event that took place $\sim$ 9 km beneath the surface, consistent with the extensional nature of the Apennines [Elter et al., 2003, Atzori et al., 2009]. The aftershocks indicated that the main fault dips SW and had $\sim 0.6 - 0.8$ m slip using interferometry and ~ 0.5 m slip with GPS [Atzori et al., 2009, Walters et al., 2009, Anzidei et al., 2009]. Further descriptions of this sequence and the associated faults can be found in [Chiaraluce et al., 2011].

The spatiotemporal Epidemic Type Aftershock Sequence (ETAS) model was fitted to the Italian catalog between April 16, 2005 to June 1, 2009 using the MLE procedure [Lombardi and Marzocchi, 2010b]. They found that the completeness of the L'Aquila sequence reaches $M_c = 2.5$ soon after the main event. With a retrospective test, the estimated model parameters were found to perform well based on statistical tests when used for daily forecasts. The model performance for real-time forecasting on the 2009 L'Aquila earthquake sequence was evaluated in [Marzocchi and Lombardi, 2009]. Subsequent work showed that the MOL was not the most suitable in terms of aftershock rate modelling [Lolli et al., 2011]. However, during the first 60 days, the strong aftershocks did not produce large increases in aftershock rate. In addition, Lolli et al. (2011) even found that the rate leading up to some

large aftershocks *increased*. Thus, the ETAS variants used in their study did not perform significantly better within the first 60 days [Lolli et al., 2011].

In a separate study, spatiotemporal forms of the MOL and ETAS models were used for daily forecasts by applying Bayesian updating which resulted in the aftershock-hazard curve for these two models. Performance of the models was evaluated using the Bayes factor [Ebrahimian et al., 2014]. Their results indicated that the spatial MOL performed better in the first two days following the mainshock, and the performance of the MOL and the ETAS model alternated in performance of the daily forecast [Ebrahimian et al., 2014]. The ETAS model generally tended to provide upper bounds to the number of estimated events. The results of the ETAS and the MOL daily forecast impact on the ground-motion hazard was in good agreement for the daily hazard predictions. They also noted that the performance of the MOL using generic parameters for Italy performs notably worse than the two other models they demonstrated performance testing on. Lastly, Ebrahimian et al. (2014) indicated that the ETAS model performs better than the MOL on several individual days.

In this study, the magnitude cutoff $M_0 = 2.5$ was the same as was used for [Ebrahimian et al., 2014] for the ISIDe catalog. The area and GR relation for the first three days following the mainshock is shown in (Figs. 3.1, 3.2). A relatively large aftershock of $M = 5.2$ took place three days after the mainshock and produced a distinct aftershock sequence which was used to fit to the CMOL.

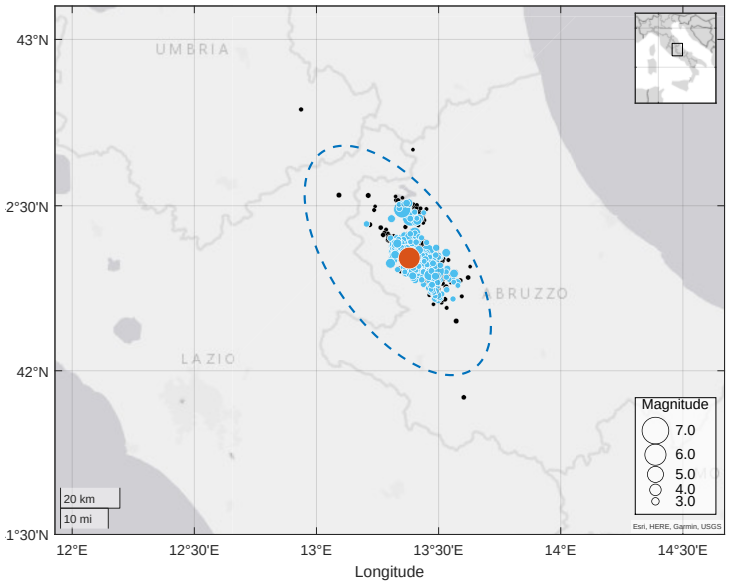

Figure 3.1: Map of the 2009 L'Aquila sequence during the first three days following the mainshock. The elliptical region indicates the area that is considered part of the sequence. The blue circles indicate the events that are included in the analysis, and the black circles indicate events outside of the study region, or below the magnitude cutoff threshold. The main shock is marked with a red circle. The inset map provides context for the geographic region in Italy.

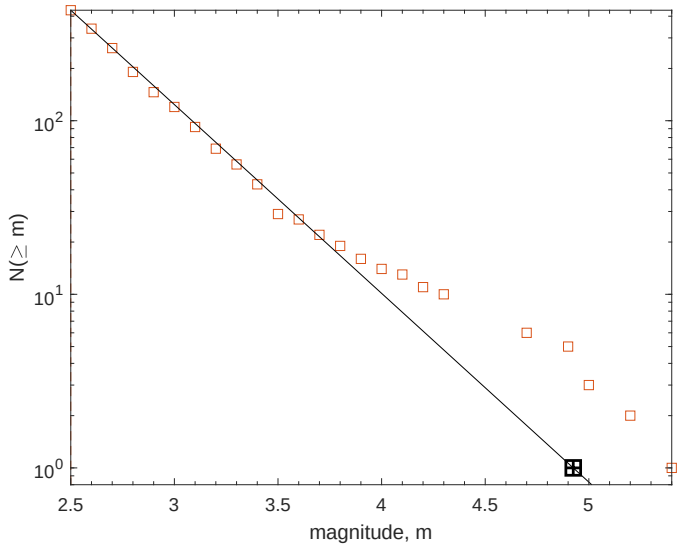

Figure 3.2: The 2009 L'Aquila sequence during the first three days following the mainshock fitted to the GR law. The events greater than the magnitude indicated on the x-axis are counted and plotted along a straight line. The events are also binned into $\Delta M = 0.1$ increments.

The L'Aquila sequence was analyzed using the MOL, CMOL, and the ETAS model. As the L'Aquila sequence was preceded by foreshocks, the foreshocks were also incorporated in

analysis for the ETAS model by using 30 days of data leading up to the mainshock in the training time interval. However, the foreshocks did not appear to have Omori-like behaviour, and thus, the CMOL did not make use of the foreshocks. Instead, the CMOL was fitted to the mainshock and the $M = 5.2$ shock at $\tau = 2.97$ days for the second large shock. As the CMOL model is equivalent to the MOL before the second shock, and the second MOL instance begins nearly three days after the mainshock, the CMOL parameter estimation begins on $T_e = 4$ days to allow time for the sequence to progress after the large aftershock. T_s for the MOL, CMOL, and the ETAS model are $T_s = 0.001, 0.001$, and 0.05, respectively. The point parameter estimates from the MLE method are provided in Figures 3.3. The aftershock sequence rate using the different models fitted for a specific training time interval is shown in Fig. 3.4. The MLE estimates, MCMC prior variance and parameter estimates from the MCMC sampling procedure are available in Tables B.1 - B.5 in Appendix B.

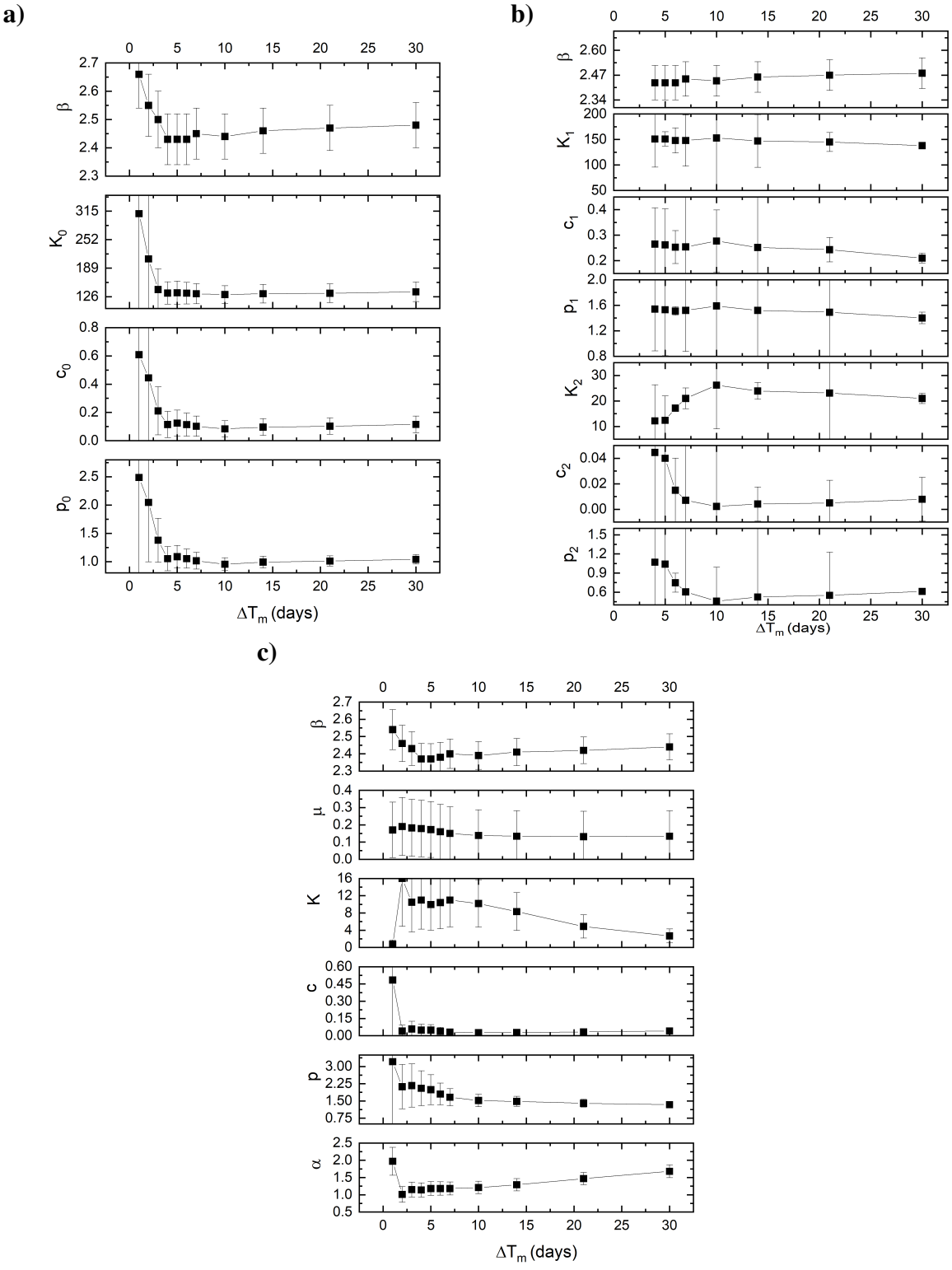

Figure 3.3: The model parameter estimates (black squares) for the L'Aquila sequence using the MLE for various training time intervals ending at ΔT_m with corresponding 95% confidence intervals. The aftershock rate models used are the a) MOL, b) CMOL and c) ETAS model.

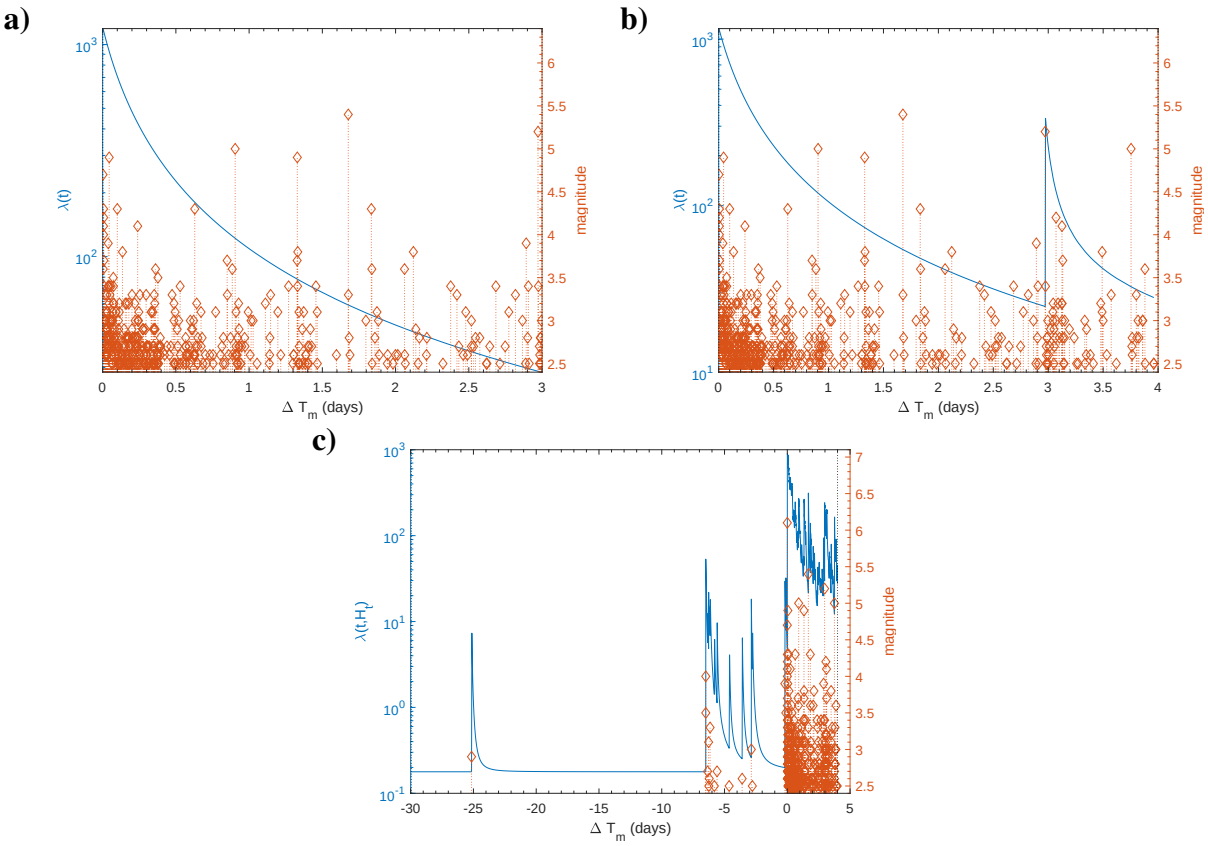

Figure 3.4: The aftershock model fit using the a) MOL and c) ETAS model to the L'Aquila sequence for ΔT_m = 3 days. The b) CMOL is shown for ΔT_m = 4 days. The events during this training time interval are shown with orange markers, where markers indicate the magnitude of the events (denoted on the right axis). The blue lines indicate the seismicity rate (left axis). The ETAS model includes an additional 30 days for the training time interval.

There was a slow shift in the decay parameter p_0 during the first few days of the sequence which increased from $p_0 \approx 0.5$ to 1.2 for the MOL over 80 days found in [Lolli et al., 2011]. This was not observed using the MLE for model parameter estimation in this sequence (Table B.1). In the MLE estimates, there was very little variation in the parameter estimates after $\Delta T_m = 4$ days, including the CMOL, which takes one day to stabilize.

The results of the real-time earthquake forecast experiment taking place during the L'Aquila sequence were described in [Marzocchi and Lombardi, 2009] which also used spatiotemporal parameters. Their reported model parameter values were $\{c, p, \alpha\} = \{0.03 \pm 0.01, 1.2 \pm 0.05, 1.5 \pm 0.1\}$ using 60 days of training time for a larger surrounding area. c is in agreement with the results from this study and p decreases from 3.2 to 1.3 at $\Delta T_m = 30$. α is close to their reported values.

The probabilities of largest expected aftershock for the MOL, CMOL, and ETAS models as computed in this study are shown in Figure 3.5. From most of the probability estimates, the ETAS model provided the upper bound of the probability of large aftershocks. The performance of the ETAS model in this work demonstrated a similar trend to the forecast in Marzocchi et al. (2009) which used a forecasting time period of $\Delta T = 1$ day.

As expected, the general trend of the probability for large events was to decrease as the forecasting time interval was shifted further away from the mainshock. The forecasting behaviour during the early aftershock sequences $\Delta T_m \leq 4$ indicated a slight increase in the probability of large aftershocks for the ETAS model leading up to the time of the large $M = 5.2$ aftershock, τ. This was reflected in the ETAS model parameter estimate of K, which increased 10-fold following $\Delta T_m = 1$, with slight adjustments to other model parameters as well. Following τ, the effects of the increased seismicity had limited impact on the probability estimates for longer training time intervals. The contribution of seismicity from the aftershock taking place at τ can be seen in the CMOL probabilities. Following the second shock, the probability decreased steeply as K_2 stabilized, then was restored as the contribution from the second shock increased slightly afterwards. From the MLE estimates, the K_0 parameter from the MOL was simply

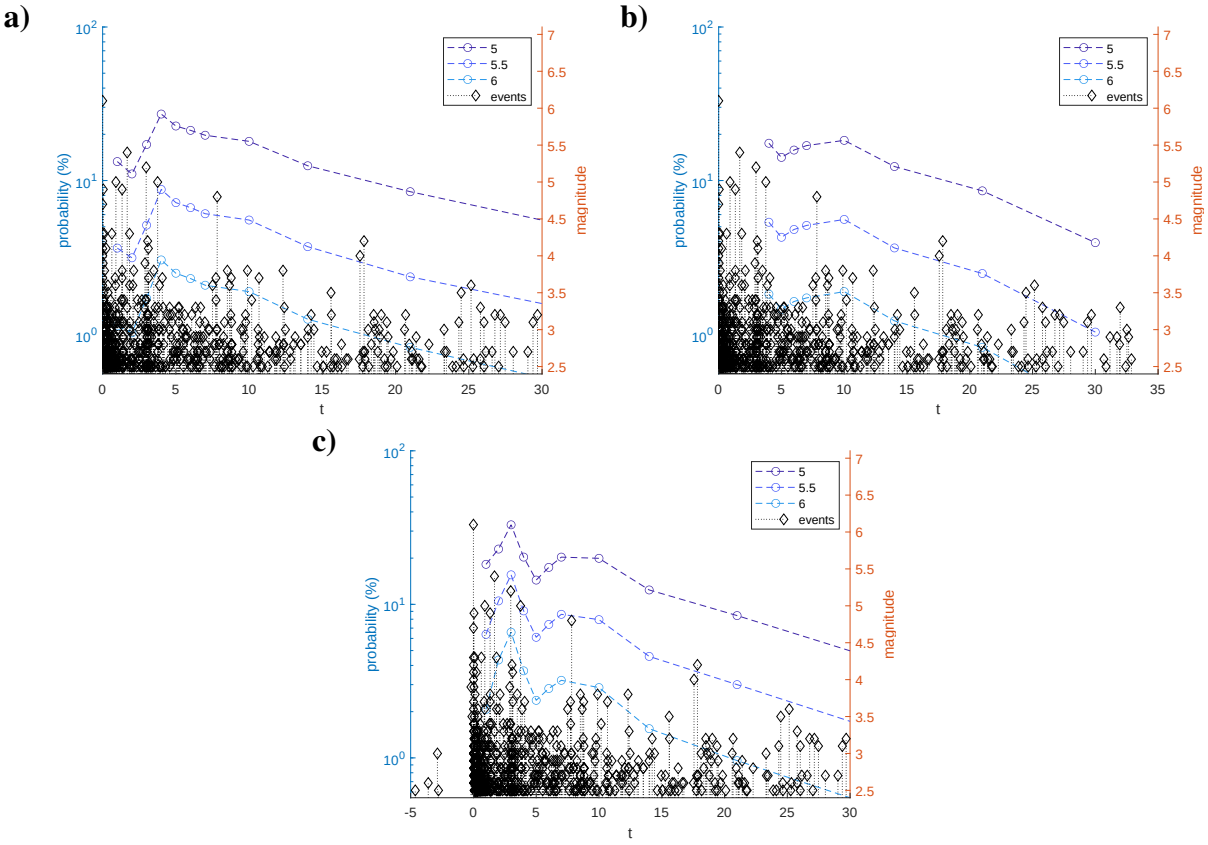

Figure 3.5: The probability of large aftershock of $M_{ex} = \{5.5, 6.0, 6.5\}$ during a seven-day forecast for the L'Aquila sequence using various target time intervals for the MOL, CMOL, and ETAS model in figures a), b) and c), respectively. The events are used in the training time intervals are shown with black diamonds, corresponding with their magnitudes (right axis). The probabilities are indicated for the corresponding training time interval.

distributed into two contributions for the CMOL. For $\Delta T_m \geq 14$, the probability estimates converged and provided similar forecast results.

3.1.1 Forecast Test Results

In the comparison tests, the ETAS model performed better than the MOL in both directions (Fig. 3.6). For the MOL vs. ETAS comparison test, the information gain was weakly positive, which did not entirely refute the hypothesis that the MOL may be the better model. When comparing the CMOL to the MOL, the MOL performed better after $\tau = 2.97$ as seen in Table 3.1. The N-, M-, and p-test scores for the L'Aquila sequence BPD forecasting results are shown in Figure 3.7.

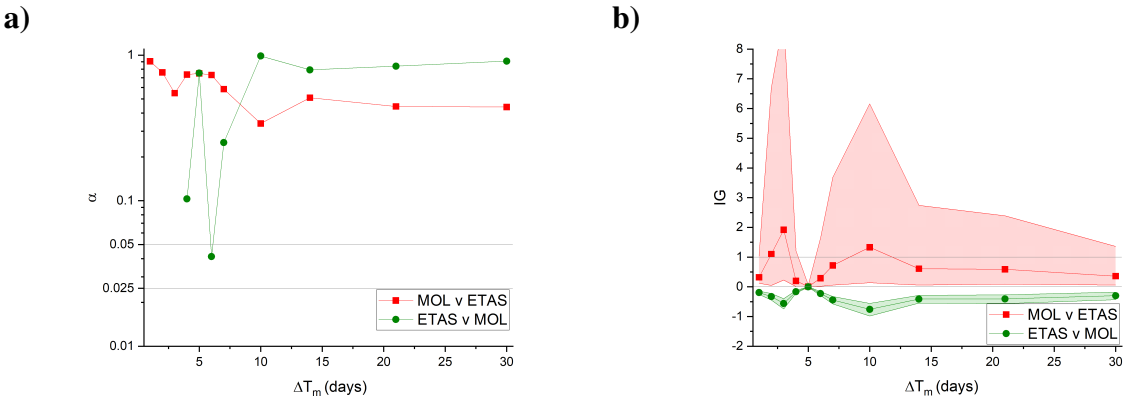

Figure 3.6: Results of the a) R-test and b) T-test for the L'Aquila sequence using relative information gain and quantile score α for the MOL and the ETAS model. Quantile scores of zero are not plotted. The 95% confidence intervals for the information gain are shown on the information gain plot.

Table 3.1: Results of the T-test and R-test for the L'Aquila sequence as shown using relative information gain and quantile score α for the MOL (M) and the CMOL (C). The 95% confidence intervals for the information gain are also provided. The confidence intervals are indicated by their lower (-) and upper (+) bounds.

ΔT_m	α_{CvM}	IG_{CvM}	IG_{CvM} -	IG_{CvM} +	α_{MvC}	IG_{MvC}	IG_{MvC} -	IG_{MvC}+
4	0.90	0.41	*0.11*	*0.12*	0.00	-0.25	*0.07*	*0.07*
5	0.99	0.37	*0.10*	*0.11*	0.00	-0.22	*0.07*	*0.06*
6	0.96	0.25	*0.07*	*0.07*	0.00	-0.18	*0.06*	*0.05*
7	0.74	0.14	*0.04*	*0.04*	0.03	-0.12	*0.04*	*0.03*
10	0.98	-0.05	*0.01*	*0.01*	0.02	0.05	*0.01*	*0.02*
14	0.81	-0.01	*0.00*	*0.00*	0.30	0.01	*0.00*	*0.00*
21	0.85	-0.04	*0.02*	*0.01*	0.14	0.04	*0.01*	*0.02*
30	0.63	-0.03	*0.04*	*0.04*	0.25	0.04	*0.03*	*0.04*

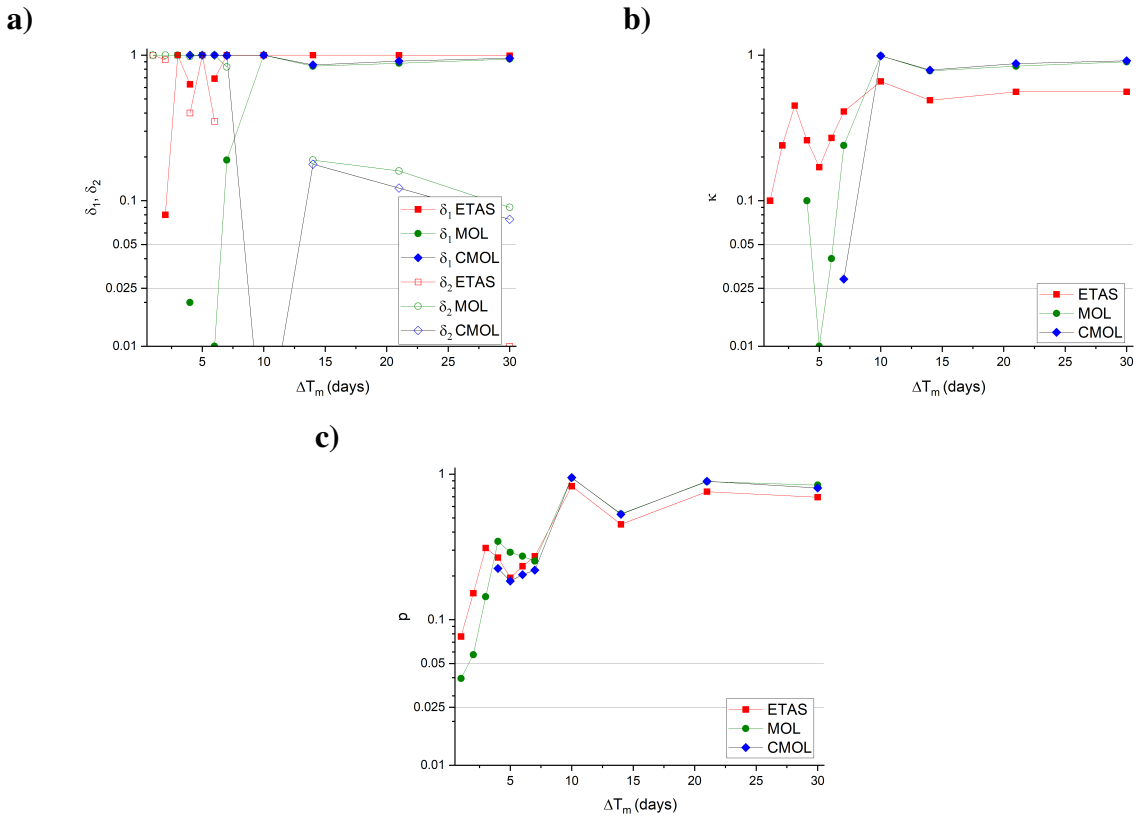

Figure 3.7: The performance of the MOL, CMOL, and ETAS model for various training time intervals for the L'Aquila sequence. Forecast performance scores are listed for the N-test (δ_1, δ_2), the M-test (κ), and the Bayesian p-test in images a), b) and c), respectively.

Generally, the N-test indicated that the ETAS model performed well for the longer target time intervals. However, the ETAS model underestimated the number of events during $\Delta T_m = 1$ day and $\Delta T_m = 5$ days (Fig. B.3 in Appendix B). This corresponded to the low K at $\Delta T_m = 1$ day and low probability of large aftershocks following both training time interval. The MOL tended to underestimate the number of events until $\Delta T_m = 10$ days, around when the forecast probabilities begin to converge for the different models. The CMOL performed reasonably well on the N-test for all the training time intervals it was applied to. Low δ_1 scores were found at training time intervals $\Delta T_m = 5$ days, where both the ETAS model and the MOL underestimated the number of events. This also corresponds with the M-test quantile score decrease, potentially related to a shift in the magnitude distribution following contribution from the seismicity associated with the aftershock at time τ.

The ETAS model passed the M-test consistently (Fig. 3.7b). The MOL performed poorly on the M-test during several early training time intervals $\Delta T_m \leq 6$. The CMOL performance on the M-test was the same as the MOL. None of the models failed the Bayesian p-test. For this sequence, the CMOL was unnecessarily complex without providing additional information. Thus, the MOL was more suitable than the CMOL for forecasting during the training time periods investigated. In addition, the information gain of the CMOL vs MOL indicated that during the training time intervals closer to τ, the MOL performed better than the CMOL, despite the CMOL specifically identifying the location of the secondary aftershocks (Table 3.1). Considering that the model parameters of the MOL and the ETAS do not change in a notable manner following τ, the contributions from the smaller aftershock sequence may be considered minimal.

In contrast to [Lolli et al., 2011], the ETAS model appeared to perform better than the MOL based on the selected training time intervals. As with [Ebrahimian et al., 2014], the ETAS provided an upper-bound estimate during the evolution of the model forecasts and was better at responding to increases in number of events during the ongoing sequence. From their spatiotemporal forecasts, both the MOL and ETAS model were generally good at representing the

trend in the number of aftershocks. In the results from this study, the number of forecasted events is underestimated close to the mainshock, though the ETAS underestimates the number events at specific training time intervals.

3.2 The 2016 Amatrice, Italy, Sequence

The 2016 Amatrice sequence was initiated with an event with magnitude $M_w = 6.0$ near the village of Amatrice in Central Italy on August 24, 2016 at 01:36 UTC and included a $M_w = 5.4$ aftershock within an hour of the mainshock (Fig. 3.8). A 60 km long normal fault system was activated during the 2016 Amatrice sequence. The sequence was very active and produced several $M_w \geq 5.0$ events. Hundreds of earthquakes took place after the mainshock and in the months following, the aftershocks migrated into the the 2009 L'Aquila aftershock zone [Mancini et al., 2019].

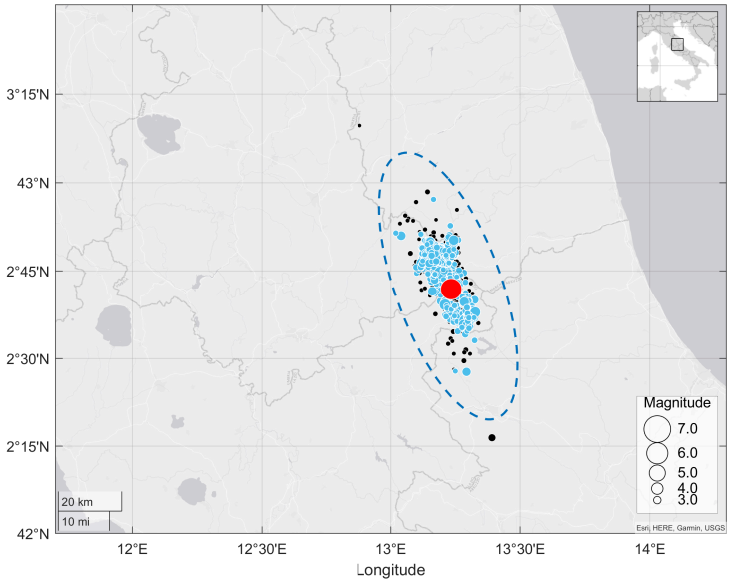

Figure 3.8: Map of the 2016 Amatrice sequence during the first three days following the mainshock of $M_w = 6.0$. The elliptical region indicates the area that is considered part of the sequence. The blue circles indicate the events that are included in the analysis, and the black circles indicate events outside of the study region, or below the magnitude cutoff threshold. The mainshock is indicated by the red circle. The inset map provides context for the geographic region in Italy.

The spatiotemporal ETAS model was previously fitted to this sequence in conjunction with

Bayesian inference and MCMC methods to sample directly from the posterior probability distribution [Ebrahimian and Jalayer, 2017]. They used a simulation-based method that provided a robust estimate of the spatial distribution of the events within a specific forecasting time interval following the main event. Ebrahimian and Jalayer (2017) accounted for the ETAS model parameter uncertainty estimates in the posterior joint probability distribution as conditioned by the events prior in the sequence. The method used in Ebrahimian and Jalayer differs from the BPD method in this study, which uses the priors from the MLE estimates for each training time interval rather than the previous training time interval estimates.

In this study, the magnitude cutoff was set to $M_0 = 2.5$ (Fig. 3.9). The MOL and ETAS models were applied to the 2016 Amatrice sequence. There was no clear indication of strong seismicity following an aftershock during the early aftershock sequence analysis. Thus, the CMOL was not applied for this sequence. Prior to the ETAS model parameter estimation, the background seismicity was reviewed over the preceding three years of available data within the elliptical study region and fixed to $\mu = 0.3$ for all training time interval estimates (Fig. 3.8). This resulted in stable parameter estimates for the remainder of the analysis and avoided over estimation of μ when the parameter was not fixed. Foreshock activity was not included in the ETAS model analysis. T_0 was set to time of the mainshock for all models, and $T_s = 0.001, 0.02$ for the MOL and ETAS model, respectively. The model parameter estimates are shown in Figure 3.10, with point parameter values provided in Tables B.8 and B.10 in Appendix B. The aftershock sequence rate as provided by the aftershock rate models is provided in Figure 3.11. The corresponding MCMC sampling and Gamma prior variances are also provided in B.11, B.12, and B.13 in Appendix B. While the model parameters for the ETAS model are presented in a different form than that of [Ebrahimian and Jalayer, 2017], the c value estimates in this work are similar to their estimates, with slightly higher p-values around $p = 1.4$.

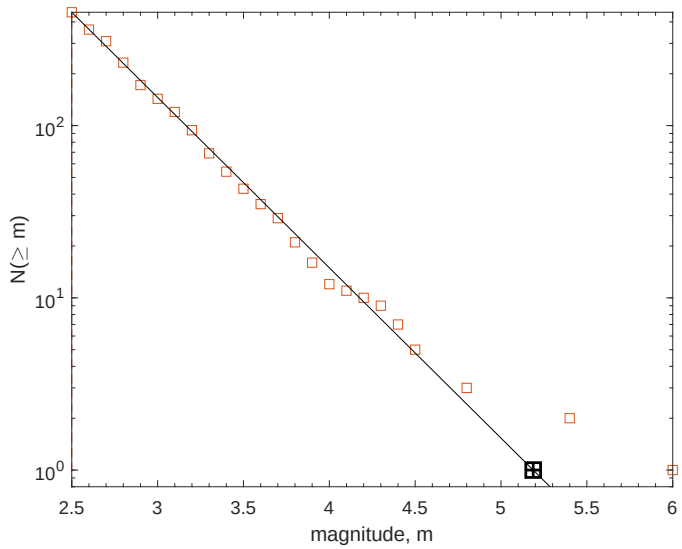

Figure 3.9: The 2016 Amatrice sequence during the first three days following the mainshock was fitted to the GR law. The events greater than the magnitude indicated on the x-axis are counted and plotted along a straight line. The event magnitudes were binned into $\Delta M = 0.1$ increments.

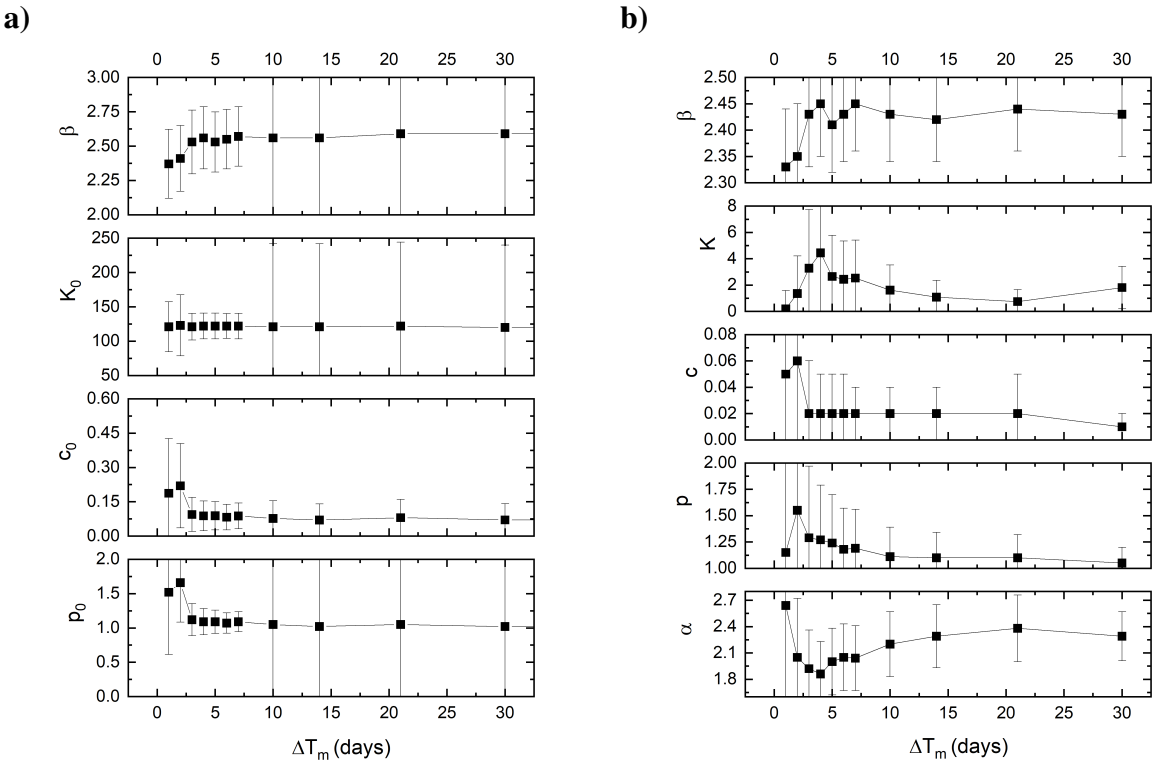

Figure 3.10: The model parameter estimates (black squares) for the Amatrice sequence using the MLE for various training time interval ending at ΔT_m with corresponding 95% confidence intervals. The aftershock rate models used are the a) MOL and b) ETAS model.

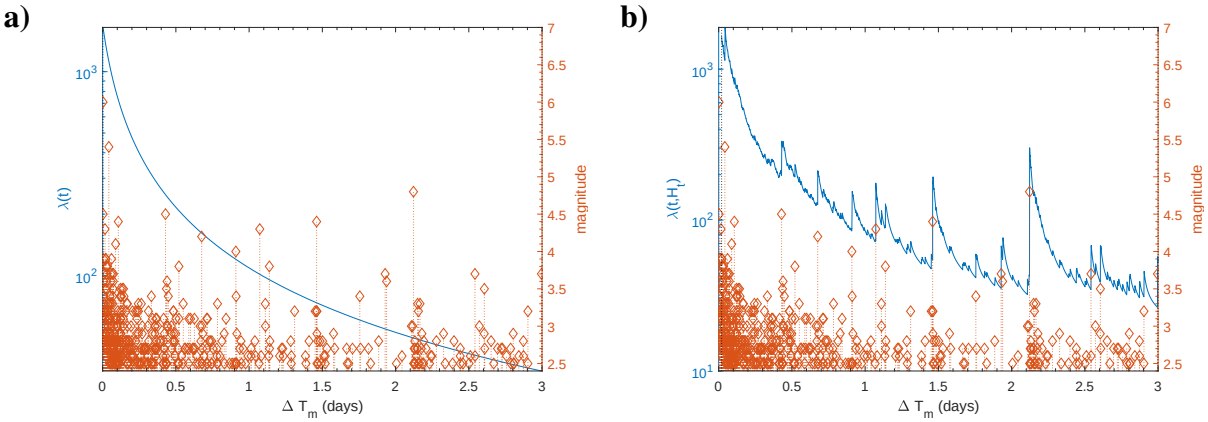

Figure 3.11: The aftershock model fit using the a) MOL and b) ETAS model to the Amatrice sequence for $\Delta T_m = 3$ days. The events during this training time interval are shown with orange markers, where markers indicate the magnitude of the events (denoted on the right axis). The blue lines indicate the seismicity rate (left axis).

[Lombardi, 2016] reviewed the Amatrice sequence using the spatiotemporal ETAS model with the MLE estimation of model parameters. They produced a forecast using the thinning method and compared the forecast to the observed number of events for varying forecasting magnitudes. From Lomdardi's analysis, it is evident that the ETAS model does not have predictive ability prior to a main event, as the probability of having an event $M_L \geq 5.5$ for the entire area under consideration is very small before the mainshock. Lombardi also found that the ETAS model parameter sensitivity was negligible with respect to the occurrence history at the time of the work, which was during the ongoing events of the Amatrice sequence.

The probability of the largest aftershocks using the BPD forecast is shown in Figure 3.12. As expected, the probability of the largest aftershock decreased with increased training time intervals. The ETAS model forecasts provided the upper bound of the estimates. Both models demonstrated a slight increase in probability at $\Delta T_m = 3$ days. This corresponded to a slight increase in the K parameter for the ETAS model and a decrease in the p and p_0 parameters for both models, which reduced the rate of seismicity decay. The lower probability estimate following $\Delta T_m = 2$ days was also reflected in some of the statistical tests.

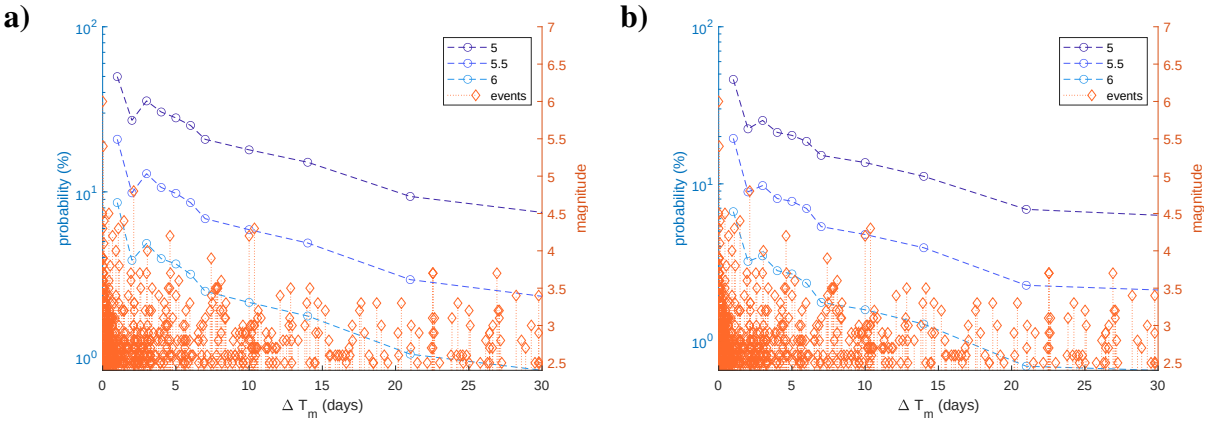

Figure 3.12: The probability of large aftershock of $M_{ex} = \{5.5, 6.0, 6.5\}$ during a seven-day forecast for the Amatrice sequence using various target time intervals for the a) MOL and the b) ETAS model. The events are used in the training time intervals are shown with black diamonds, corresponding with their magnitudes (right axis). The probabilities are indicated at the corresponding training time interval.

3.2.1 Forecast Test Results

Based on the T-test, it can be seen that the ETAS model typically performed better than the MOL model with information gain values that were consistently positive and close to one (Fig. 3.13). This was supported by the R-test quantile scores. When reversing the test (ETAS vs. MOL), the MOL shows consistently negative information gain over the ETAS model and the R-test was failed in several instances. The results of the individual model forecasting tests are provided in Figure 3.14.

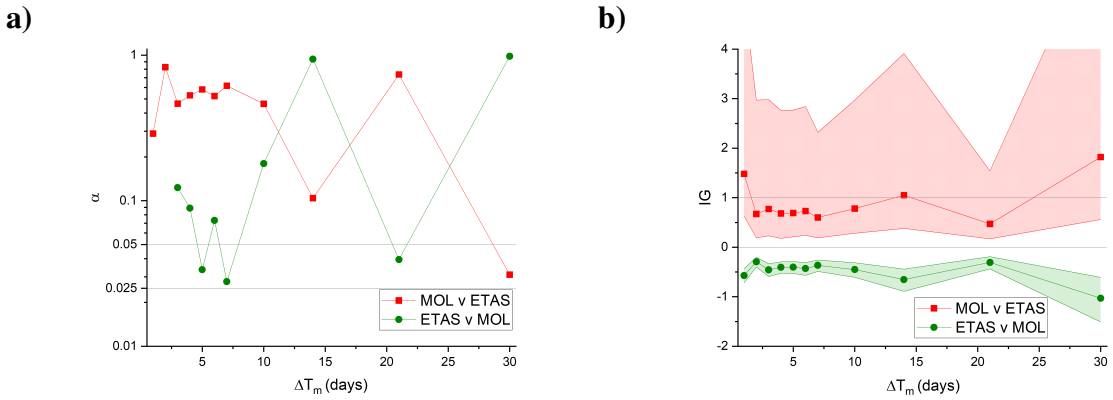

Figure 3.13: Results of the a) R-test and b) T-test for the Amatrice sequence as shown using relative information gain and quantile score α for the MOL and the ETAS model. The 95% confidence intervals for the information gain are shown on the plot.

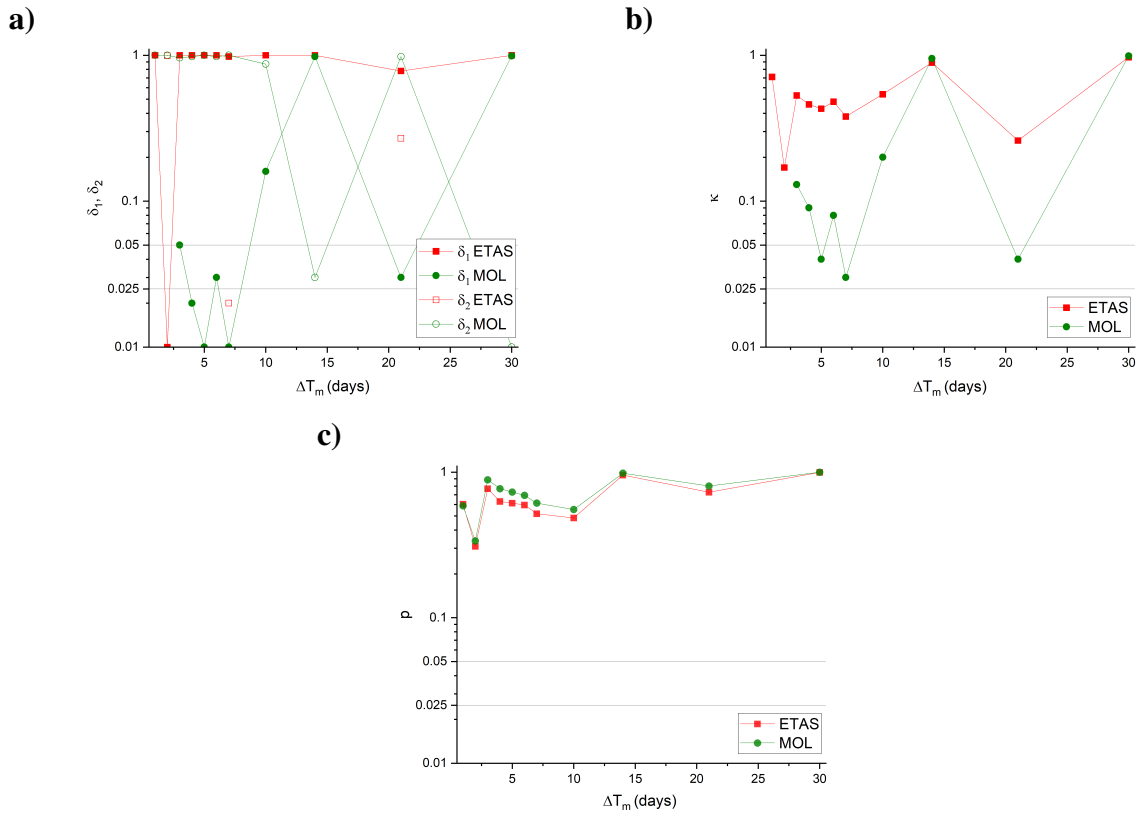

Figure 3.14: The performance of the MOL and the ETAS model for various training time intervals for the Amatrice sequence. Forecast performance scores are listed for the N-test (δ_1, δ_2), the M-test (κ), and the Bayesian p-test in figures a), b) and c), respectively.

From the N-test results, the MOL tended to underestimate the number of events during the forecasting time interval. In comparison, the ETAS model tended to overestimate the number of events, but not greatly (see Fig. B.6 in Appendix B). Thus, when interpreting the probabilities provided by the model forecasts, it is not surprising that the ETAS model consistently provided the upper bound to the probability of large aftershocks as seen in Figure 3.12.

The ETAS model tended to perform better on the M-test than the MOL, especially for shorter ΔT_m. However, the shape of the M-test was similar for both of the models. This suggests that the performance on the M-test may have been influenced by additional factors that were not the model parameters of the aftershock models.

The general behaviour of the p-test score reflected the behaviour in the number of events produced during the forecast. When the p-value was high, the number of events N_{sim} in the

forecasts was on average higher than N_{obs} for the same training time intervals (Fig. B.6 in Appendix B). The MOL p-values mimicked the behaviour of the ETAS model results. Thus, despite the MOL having simulated fewer events than average, the maximum magnitude as displayed by the Bayesian p-test produced nearly the same results as with the ETAS model.

[Mancini et al., 2019] retrospectively demonstrated the spatiotemporal ETAS model applied to the 2016 Amatrice sequence beginning with training on 2005 with a fixed productivity value K. The parameter estimates were produced using the MLE and a spatially isotropic power law distribution were used for the spatial distribution component of the ETAS model [Mancini et al., 2019]. Compared to the other models in that paper based on several classes of the Coulomb rate-stress, the ETAS model indicated the lowest rejection ratio during the shorter training time intervals and tended to pass the N-test [Mancini et al., 2019]. Following the $M_w = 6.0$ foreshock, the ratio of ETAS model forecasted to observed events during the one day forecast was 1.22 [Mancini et al., 2019]. The forecasts following the events two months after the mainshock, the forecast to observed events is 1.65. In comparison, the average number of events forecasted during the seven-day forecast from this study using $\Delta T_m = 1$ day was 0.62 when using the ETAS model (Fig. B.6 in Appendix B). However, the seven-day forecast following $\Delta T_m = 60$ days in this work had a ratio of 0.33. The forecasts produced by the temporal ETAS model in this study produced fewer events than that of the spatiotemporal ETAS model used in Mancini et al. (2019). Despite this difference, the ETAS model in this study still performs better than that of the MOL.

3.2.2 Forecasting the Second Largest Event

With retrospective knowledge, it is known that a large shock of $M = 6.0$ in the 2016 Amatrice sequence occurred. This event took place after two months following the mainshock. The forecasting probability of this event for seven days following $\Delta T_m = 63$ days with the MOL and ETAS model were 0.3% (EVD), 0.4% (BPD) and 0.3% (ETAS). While the 2016 Amatrice sequence was known to have migrated, the aftershock region selected contains these later migrated events and does not need to be adjusted [Ebrahimian and Jalayer, 2017]. Neither

model demonstrated the ability to forecast with high probability this larger event.

3.3 The 2016 Kumamoto, Japan, Sequence

The Kumamoto sequence began on April 14, 2016 with a large event of $M_{JMA} = 6.5$, which preceded a large shock of $M_{JMA} = 6.4$ and the $M_w = 7.0$ ($M_{JMA} = 7.3$) mainshock (Fig. 3.15). The foreshocks took place near the northern part of the Hinagu fault, and the subsequent earthquakes took place along the active Futagawa-Hinagu fault zone [Kawamoto et al., 2016]. The initial results of the finite-fault estimation were provided in [Kawamoto et al., 2016], indicating right lateral strike-slip fault along the Futagawa fault segment. The mainshock of the Kumamoto sequence was preceded by anomalous seismic activity and the large foreshock produced its own aftershock sequence prior to the mainshock [Nanjo et al., 2016, Nanjo and Yoshida, 2017].

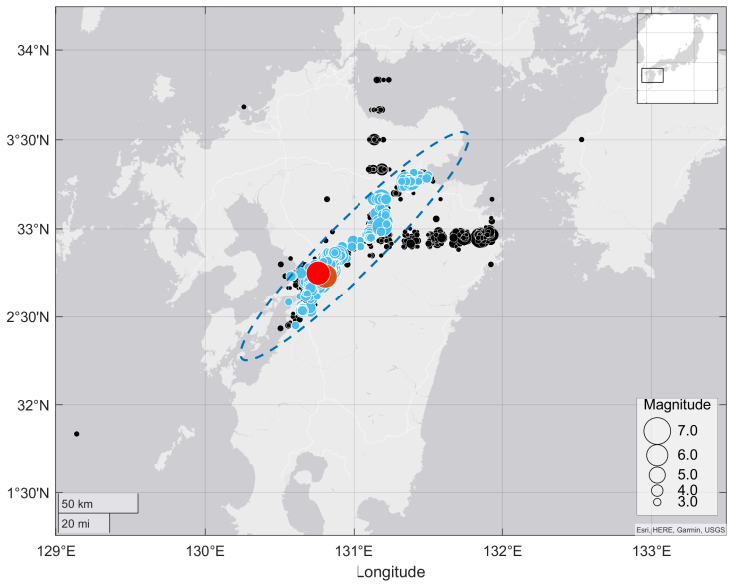

Figure 3.15: Map of the 2016 Kumamoto sequence during the first three days following the large foreshock of $M_w = 6.5$. The elliptical region indicates the area that is considered part of the sequence. The blue circles indicate the events that are included in the analysis, and the black circles indicate events outside of the study region, or below the magnitude cutoff threshold. The inset map provides context for the geographic region in Japan. The $M_w = 6.5$ foreshock is coloured in orange and the $M_w = 7.0$ mainshock is coloured in red.

[Milliner et al., 2020] found that the afterslip component of the dynamic rupture was con-

sidered an important possible triggering mechanism during the aftershock sequence. The probability of the mainshock rupture was retrospectively analyzed in a multi-element probability estimation method using anomalies and time dependent long-term forecasting [Ogata, 2017]. He found that including the first foreshock led to a higher probability of a larger earthquake forecast in the time leading up to the mainshock.

Following the 2016 Kumamoto earthquakes, the Earthquake Research Committee (ERC) of Japan revised the procedure for operational aftershock forecasting [Earthquake Research Committee, 2016]. Prior to the 2016 Kumamoto sequence, the ERC procedure for calculating aftershock probabilities used the MOL for the aftershock decay and the GR law for the magnitude-frequency relation [Omori, 1894, Gutenberg and Richter, 1944, Utsu, 1961, Utsu et al., 1995]. At the time this procedure was proposed, the ETAS model was mentioned, but no specific procedure using the ETAS model was described. The proposed method in [Omi et al., 2019] issues a forecast around three hours after the mainshock, which is an improvement to the ERC procedure produced in 2016.

In this study, the early aftershock completeness was found to be $M_c = 2.5$ (Fig. 3.16). The analysis was adjusted to use $M_0 = 3.1$ to align with previous work which first demonstrated the forecasting technique used in this thesis [Shcherbakov et al., 2018, Shcherbakov et al., 2019]. As the foreshock produced its own aftershock sequence before the mainshock occurrence, the Kumamoto sequence provided a clear instance where the CMOL could be applied.

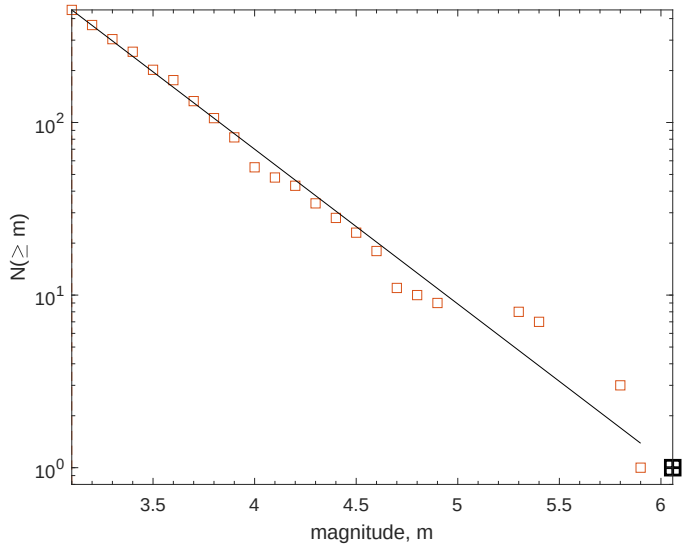

Figure 3.16: The 2016 Kumamoto sequence during the first three days following the mainshock with $M_0 = 3.1$ fitted to the GR law. The events greater than the magnitude indicated on the x-axis are counted and plotted. The events are binned by $\Delta M = 0.1$.

For the ETAS model, the foreshocks were incorporated in the target time interval for model parameter fitting. The preparatory time interval ended at $T_s = 0.03$ days following the time of the foreshock, and the evaluation for sequence progression began after the mainshock at $t = 1.17$ days. The CMOL was fitted to the beginning of the foreshock sequence and the second instance of the MOL was fitted to the mainshock of the sequence at $\tau = 1.17$ days. For the MOL, the training time period began at the mainshock. The preparatory time interval for both the MOL and CMOL ended at $T_s = 0.001$. The results of the MOL, CMOL, and the ETAS model parameter estimates using the MLE and an example of the fit at $\Delta T_m = 3$ days relative to the mainshock are shown in Figures 3.17 and 3.18. The point parameter estimates and MCMC sampling results are provided in Tables B.14 - B.20 in Appendix B.

As the background rate was relatively high compared to the other case studies, the free estimation during the MLE resulted in various μ parameters depending on the training time interval. Model parameters for $M_0 = 3.3$ fitted to the forecast sequence can be found in [Shcherbakov et al., 2019]. p and α values for the ETAS model in this work are of similar, thought slightly higher than, values presented in Shcherbakov et al. (2019).

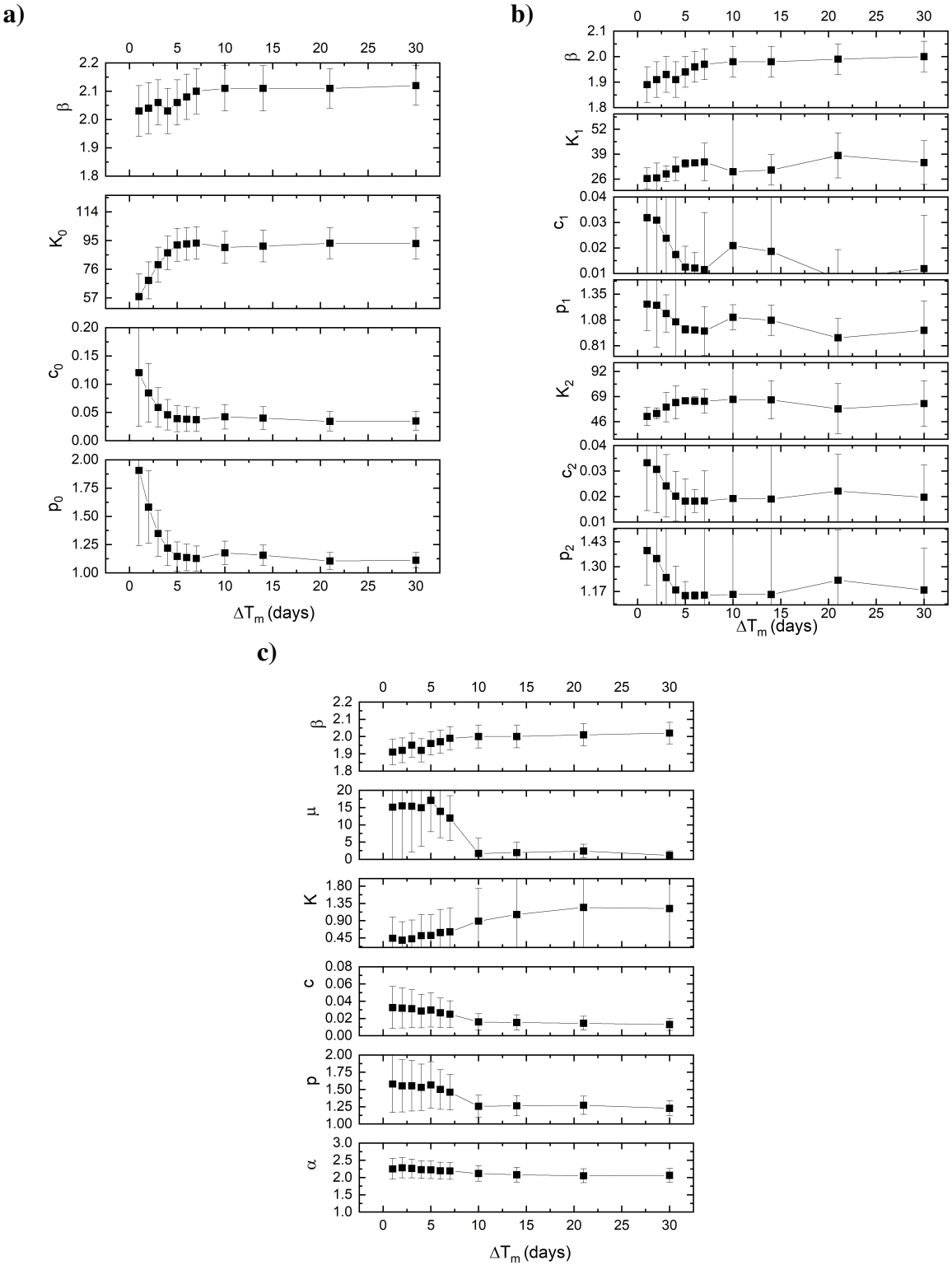

Figure 3.17: The model parameter estimates (black squares) for the Kumamoto sequence using the MLE for various training time intervals ending at ΔT_m with corresponding 95% confidence intervals. The aftershock rate models used are the a) MOL, b) CMOL, and c) ETAS model.

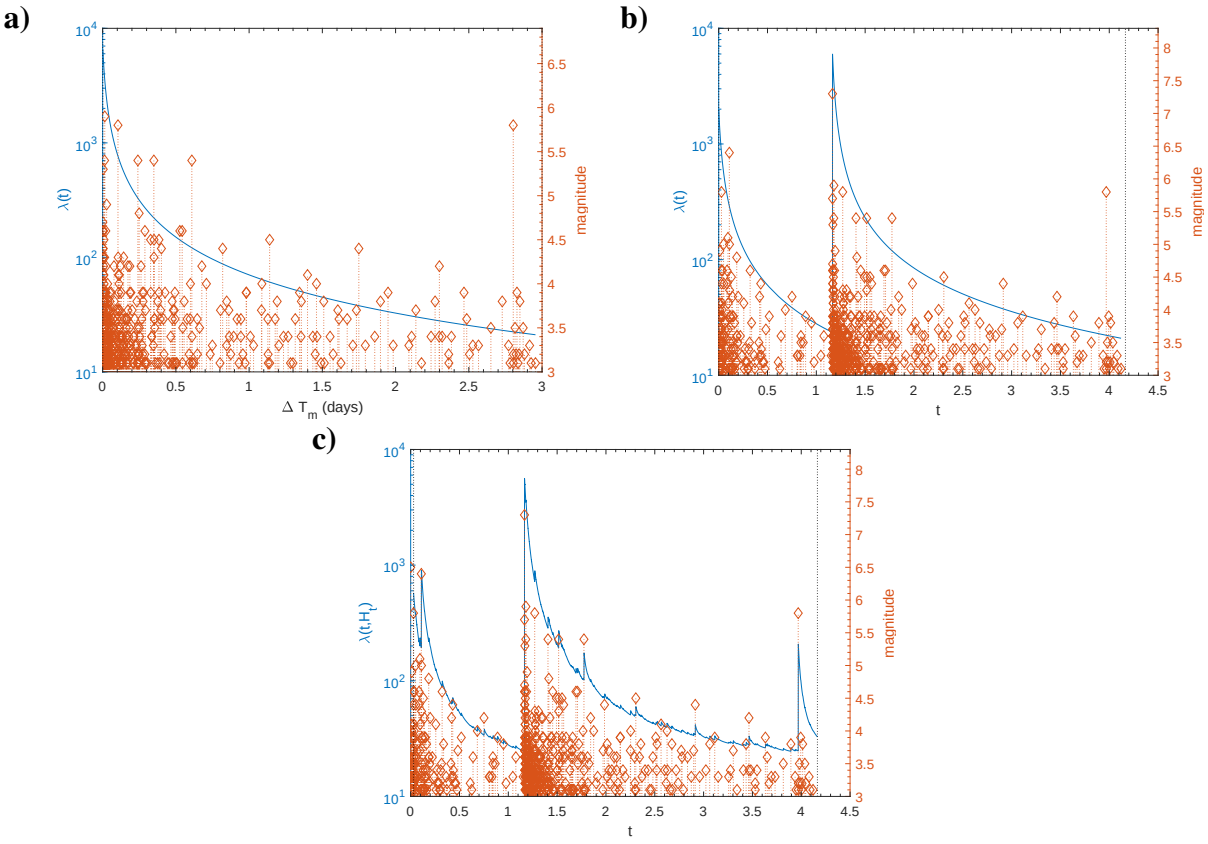

Figure 3.18: The aftershock model fit using the a) MOL, b) CMOL, and c) ETAS model to the Kumamoto sequence for $\Delta T_m = 3$ days. The CMOL and ETAS x-axis is aligned so that time t shows the number of days following the beginning of the foreshock sequence. The events during this training time interval are shown with orange markers, where markers indicate the magnitude of the events (denoted on the right axis). The blue lines indicate the seismicity rate (left axis).

The probability of the largest aftershocks corresponding to the training time intervals is presented in Figure 3.19. As with Shcherbakov et al. (2019), a large difference in the forecasted probabilities for the largest aftershock was found using the ETAS model, the MOL (BPD forecast), and the MOL (EVD forecast) (Fig. B.7 in Appendix B). For example, for forecasting $M \geq 6.0$, the probability of the MOL (BPD forecast) is nearly 40% smaller than the forecast produced by the EVD method for $\Delta T_m = 1$. The ETAS model forecast is closer to that of the MOL (EVD forecast). For training time intervals larger than $\Delta T_m = 1$ day, this difference between the MOL forecast from the BPD and the EVD method was narrowed.

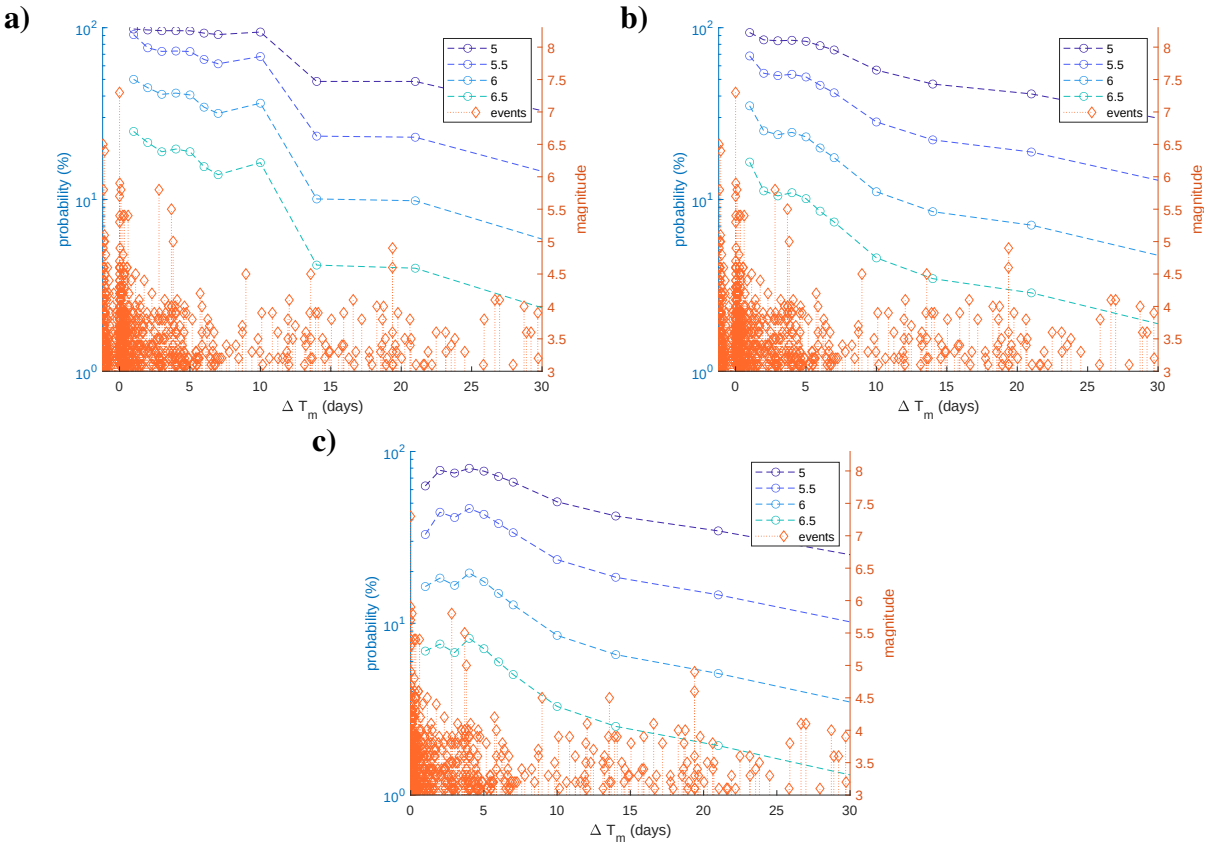

Figure 3.19: The probability of large aftershock of $M_{ex} = \{5.5, 6.0, 6.5\}$ during a seven-day forecast for the Kumamoto sequence using various target time intervals for the MOL, CMOL, and ETAS model in figures a), b) and c), respectively. The events are used in the training time intervals are shown with black diamonds, corresponding with their magnitudes (right axis). The probabilities are indicated at the corresponding training time interval.

Generally, the probability of large aftershocks decreased with increasing ΔT_m and the model probabilities began to converge at longer training time intervals. The ETAS model provided

the upper bound of the probabilities, and typically demonstrated fluctuations towards increased probabilities at the same time as the MOL and CMOL. The slight increased probability at $\Delta T_m = 10$ may be related to a smaller p-value, which would reduce the decay rate of the individual seismicity contributions from the aftershocks. Considering the mainshock magnitude of $M_{JMA} = 7.3$, intuitively, the probability of large aftershocks produced by the ETAS seemed rather large. However, when reviewing the β estimates from the GR law during the model parameter estimation, the β value changes as the sequence progresses. The lower β value may correspond to the high probability of large aftershocks seen close to the mainshock.

3.3.1 Forecast Test Results

The T-test indicate that the forecasts from ETAS model performed better than the MOL over the same training time periods (Fig. 3.20). However, the confidence intervals on the interpretation of the information gain indicated that the relative information gain is difficult to ascertain and the standard deviation for the number of events generated is very large. In addition, the R-test results are difficult to interpret, though the α scores appear to be paired in opposite values when comparing the ETAS model and the MOL. The CMOL vs. MOL fails the R-test more frequently than the reverse test (Table 3.2). In addition, the CMOL demonstrated negative information gain more frequently and was thus not as good as the MOL on these tests. The performance on the other forecasting tests is shown in Figure 3.21.

The N-test indicated that the ETAS model tended to overestimate the number of simulated events during all of the training time intervals evaluated. The MOL performance on the N-test was variable, sometimes overestimating and sometimes underestimating. During $\Delta T_m = 1 - 4$ days, the MOL underestimated the number of events during the forecast. The behaviour of the MOL was similar in the CMOL results, following the same pattern on the forecasting performance tests as the MOL. Considering the K_1 value was approximately $K_1 \approx 1/3K_0$, the contribution from the foreshock sequence in the CMOL may have been overestimated.

The M-test was consistently passed by the ETAS model (Fig. 3.21b). The MOL and CMOL performed similarly on the M-test, failing and passing for the same training time intervals. All

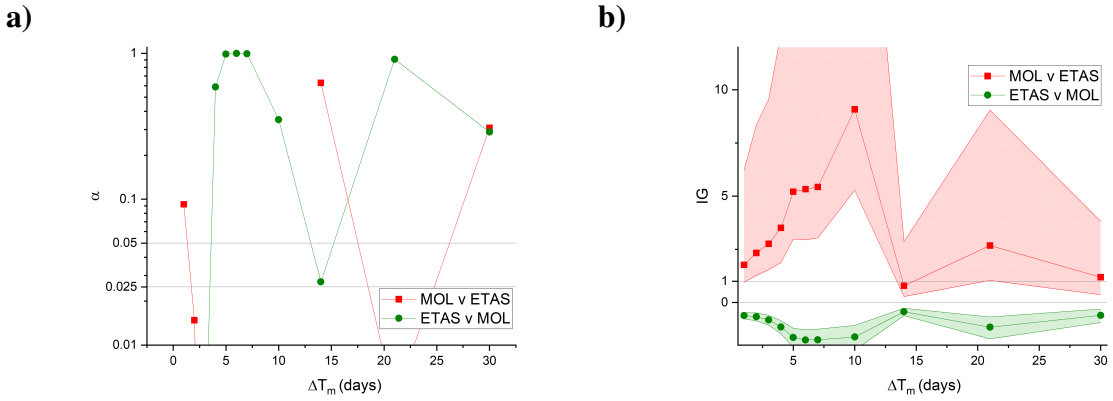

Figure 3.20: Results of the T-test and R-test for the Kumamoto sequence as shown using relative information gain and quantile score α for the MOL and the ETAS model in figures a) and b), respectively.

Table 3.2: Results of the T-test and R-test as shown using relative information gain and quantile score α for the MOL (M) and the CMOL (C) for the Kumamoto sequence. The 95% confidence intervals for the information gain are also provided. The confidence intervals are indicated by their lower (-) and upper (+) bounds.

ΔT_m	α_{CvM}	IG_{CvM}	IG_{CvM} -	IG_{CvM} +	α_{MvC}	IG_{MvC}	IG_{MvC} -	IG_{MvC}+
1	1.00	0.01	*0.01*	*0.01*	0.01	0.01	*0.01*	*0.01*
2	1.00	0.01	*0.01*	*0.01*	0.00	-0.01	*0.01*	*0.01*
3	0.28	-0.02	*0.01*	*0.01*	0.53	0.03	*0.01*	*0.01*
4	0.89	0.07	*0.02*	*0.02*	0.02	-0.06	*0.02*	*0.02*
5	0.66	0.04	*0.02*	*0.02*	0.18	-0.03	*0.02*	*0.02*
6	0.38	0.04	*0.03*	*0.03*	0.41	-0.03	*0.03*	*0.03*
7	0.26	0.03	*0.03*	*0.03*	0.56	-0.03	*0.03*	*0.03*
10	0.70	0.07	*0.03*	*0.03*	0.14	-0.07	*0.03*	*0.03*
14	0.96	0.06	*0.03*	*0.03*	0.01	-0.05	*0.03*	*0.03*
21	0.81	0.00	*0.04*	*0.03*	0.12	0.01	*0.03*	*0.04*
30	0.95	0.02	*0.03*	*0.02*	0.03	-0.01	*0.03*	*0.03*

models passed the p-test for every training time interval (Fig. 3.21c).

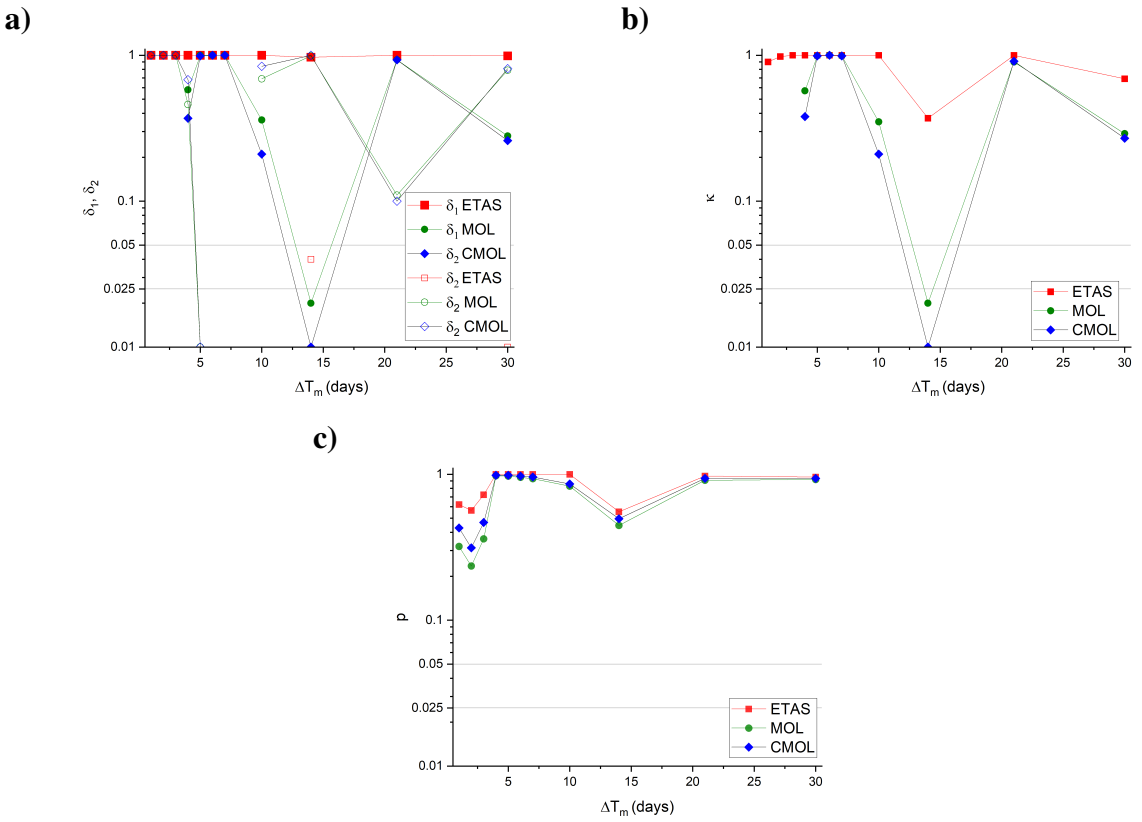

Figure 3.21: The performance of the MOL, CMOL, and ETAS model for various training time intervals for the Kumamoto sequence. Forecast performance scores are listed for the N-test (δ_1, δ_2), the M-test (κ), and the Bayesian p-test in figures a), b) and c), respectively.

3.4 The 2020 Monte Cristo Range, United States of America, Sequence

The Monte Cristo Range (MCR) sequence is one of the most recent active sequences that has been ongoing since the beginning of this work in 2020. The sequence began with a M_w = 6.5 at 11:03:27 UTC on May 15, 2020 northeast of the Mina deflection, in the Central Walker Lane, on a previously unmapped fault 56 km from Tonopah, Nevada. The MCR sequence began with a shallow crustal mainshock along a steeply dipping fault [Morton et al., 2020]. Subsequent events took place with right-lateral, left-lateral, and normal fault motions including aftershocks of $M \geq 5.0$ [Morton et al., 2020]. Prior to this incidence, the fault zone which ruptured had been unmapped. Previous events with $M > 6.0$ within the past 100 years and

a 50 km radius were both north of this event and took place in 1932 and 1934, respectively [Vigil et al., 2000].

No aftershock forecasting work has been produced on this sequence to date. A map outlining the sequence is shown in Figure 3.22. The latest version of the catalog for analysis was retrieved using the ComCat service on Nov 16, 2020. The GR law fitted to three days after the mainshock indicated that $M_c = 2.5$ (Fig. 3.23).

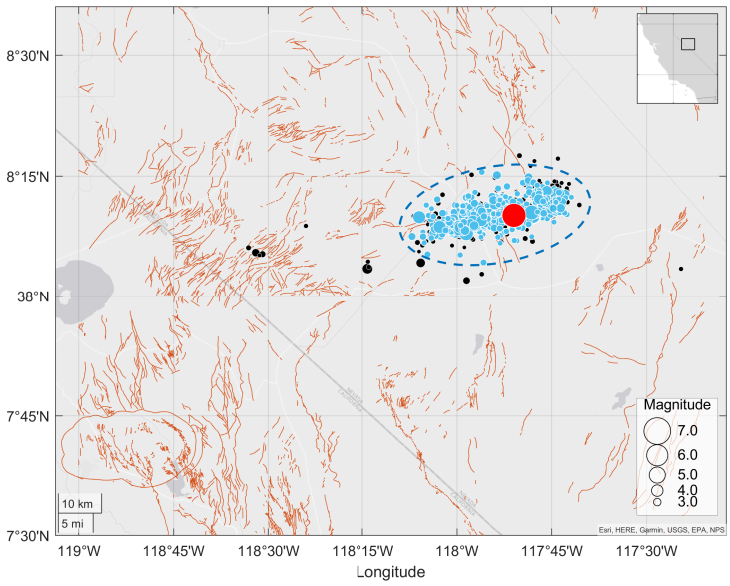

Figure 3.22: The 2020 Monte Cristo Range sequence during the first three days following the mainshock. The blue circles indicate the events that are included in the analysis, and the black circles indicate events outside of the study region, or below the magnitude cutoff threshold. The mainshock is indicated by the red circle. The inset map provides context for the MCR sequence location relative to the California and Nevada border.

Both the MOL and the ETAS model were applied to the MCR sequence with the training time period starting at the mainshock. The preparatory time period ended with $T_s = 0.001, 0.02$ for the MOL and ETAS model, respectively. The progressive parameter fit estimates for the GR law, MOL, and ETAS model are shown in Figure 3.24. The results of the MOL and the ETAS model fits with training days $\Delta T_m = 3$ days relative to the mainshock are shown in Figure 3.25. The point parameter estimates and the MCMC sampling are provided in Tables B.21 - B.27 in Appendix B. In this study, several of the MCR sequence model parameters for

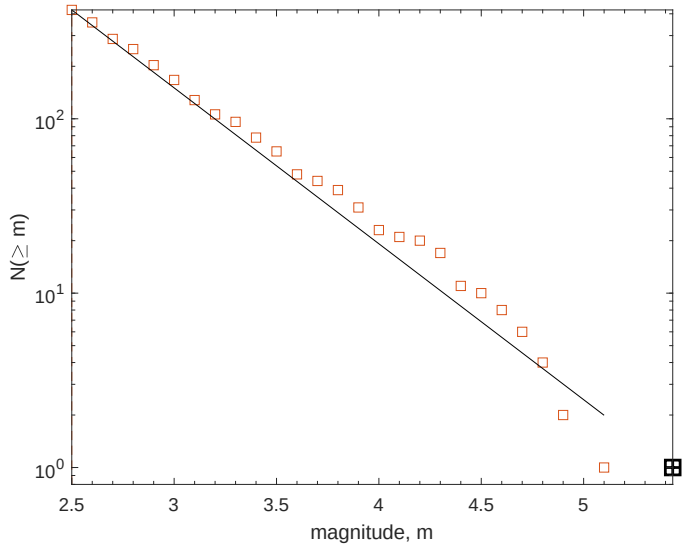

Figure 3.23: The 2020 Monte Cristo Range sequence during the first three days following the mainshock was fitted to the GR law. The events greater than the magnitude indicated on the x-axis are counted and plotted. The events were binned into $\Delta M = 0.01$ increments.

the ETAS model were fixed prior to analysis. When the ETAS model parameters were freely estimated, the model parameters were widely variable and the shorter training time interval solutions prevented the testing procedures from converging at a reasonable rate. To assist in parameter estimation stability, the ETAS model parameters μ and K were fixed to $\{0.0, 0.1\}$, respectively. To produce a normally shaped distribution for the prior, the MCMC prior mean for μ was set to $\mu = 0.001$. In addition, the training time periods ending with $\Delta T_m = 1, 2$ days had c values fixed to $c = 0.03$ prior to the MLE method as leaving these values free resulted in notably different model parameter estimates than the remaining training time intervals. The point parameter estimates for the ETAS model indicated that the MCR sequence behaviour is dominated by the mainshock, as suggested by the α parameter. Secondary aftershocks following large aftershocks were not observed. Thus, the MCR sequence was not found to be suitable for use with the CMOL.

The forecasted probabilities of the largest aftershock are shown in Figure 3.26. The probabilities produced from the BPD from the ETAS model provided the lower bound of the estimates and the MOL provided the upper bounds of the forecast probabilities for large after-

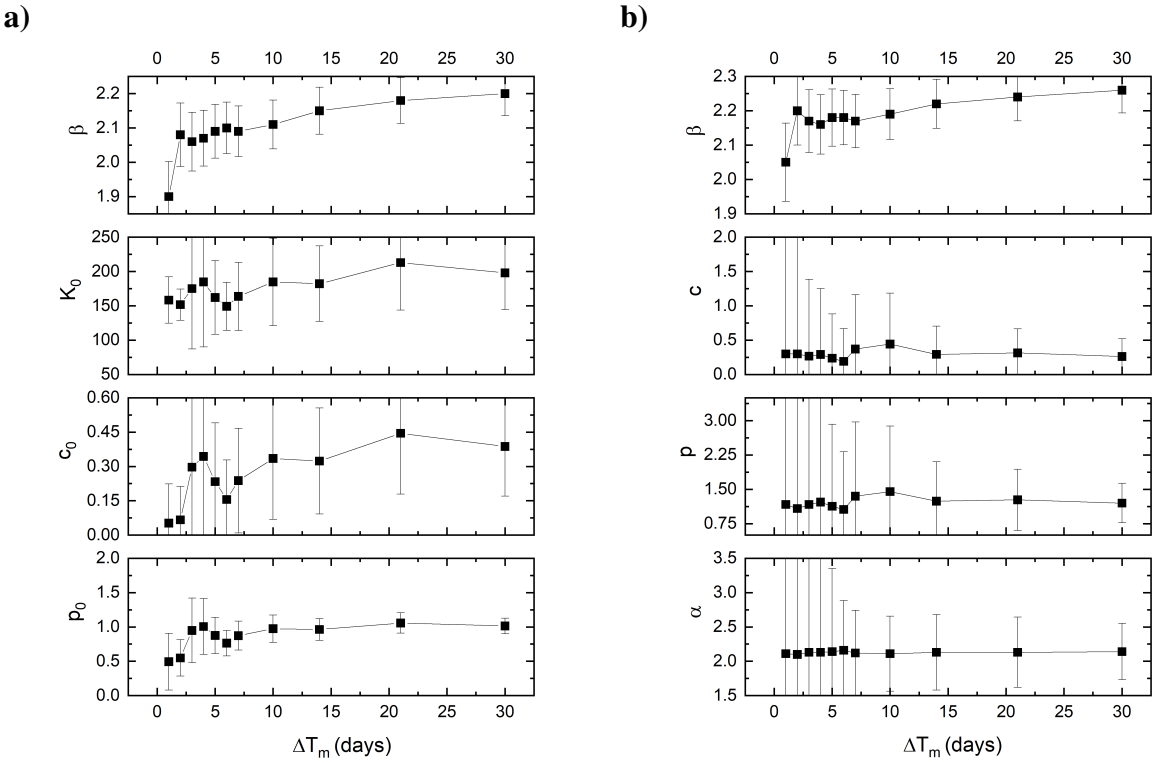

Figure 3.24: The model parameter estimates (black squares) for the Monte Cristo Range sequence using the MLE for various training time intervals ending at ΔT_m with corresponding 95% confidence intervals. The aftershock rate models used are the a) MOL and b) ETAS model.

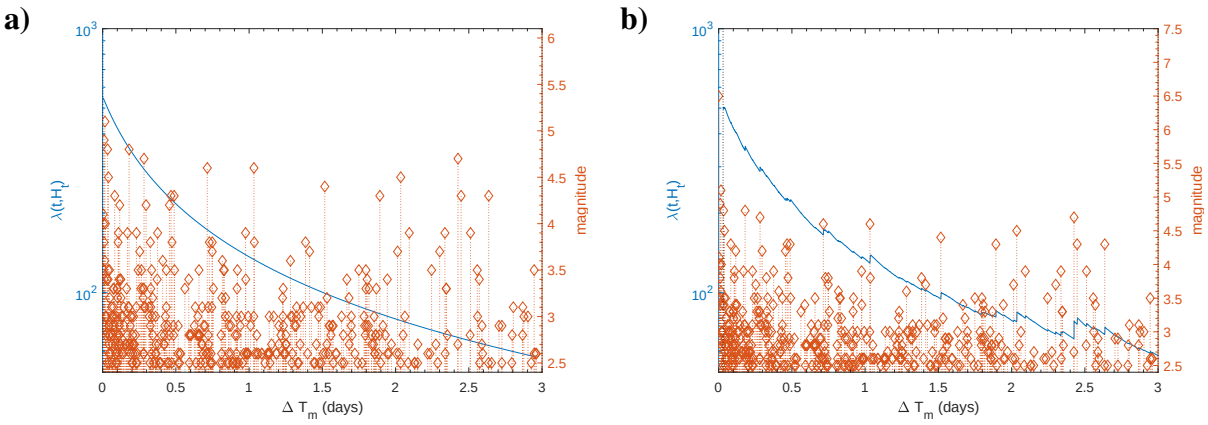

Figure 3.25: The aftershock model fit using the a) MOL and b) ETAS model to the Monte Cristo Range sequence for $\Delta T_m = 3$ days. The events during this training time interval are shown with orange markers, where markers indicate the magnitude of the events (denoted on the right axis). The blue lines indicate the seismicity rate (left axis).

shocks. The probabilities of the different models paralleled each other and began to converge with larger training time intervals.

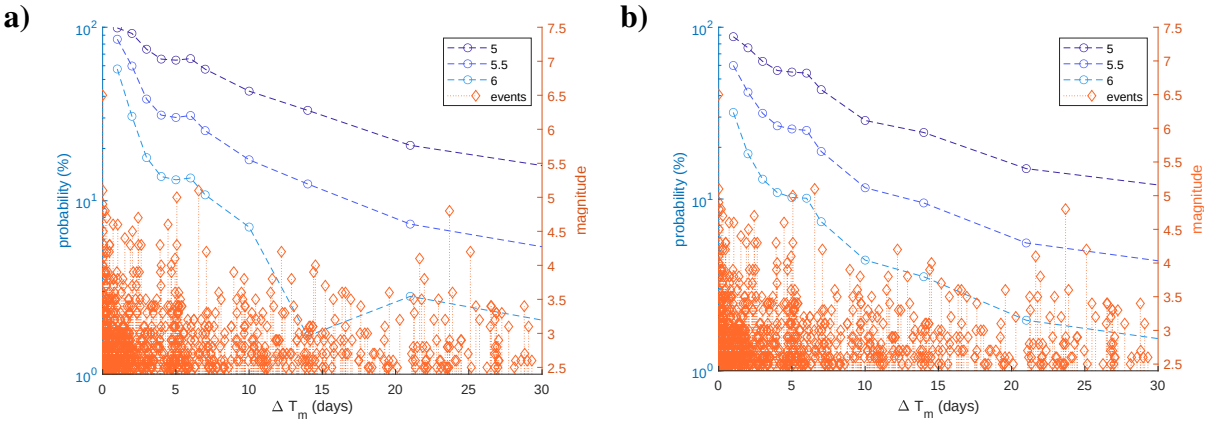

Figure 3.26: The probability of large aftershock of $M_{ex} = \{5.5, 6.0, 6.5\}$ during a seven-day forecast using various target time intervals for the Monte Cristo Range sequence is shown for the a) MOL and the b) ETAS model. The events are used in the training time intervals are shown with black diamonds, corresponding with their magnitudes (right axis). The probabilities are indicated at the end of the target time interval.

3.4.1 Forecast Test Results

The ETAS model indicated some information gain over the MOL as shown in Figure 3.27. In both ratio tests, most of the training time comparisons resulted in passing the R-test. For ETAS vs MOL, the ETAS model shows greater information gain, resulting in consistently negative values. For the MCR sequence, the α value for the ETAS model was particularly high, and provided an indicator that the sequence behaved similarly to the MOL. This was an early indicator for the sequence that the ETAS information gain over the MOL is likely to not be very large.

The forecast performance of the remaining tests can be found in Figure 3.28. The ETAS model tended to overestimate the number of forecasted events, though less frequently during the longer training time intervals. The MOL forecasted events varied between over- and underestimation of the number of events, indicating greater sensitivity to the sequence evolution. This can also be seen in the fluctuation of the MOL model parameter estimates (Table B.21). Both models typically performed well on the M-test, though the MOL failed during $\Delta T_m = 4$

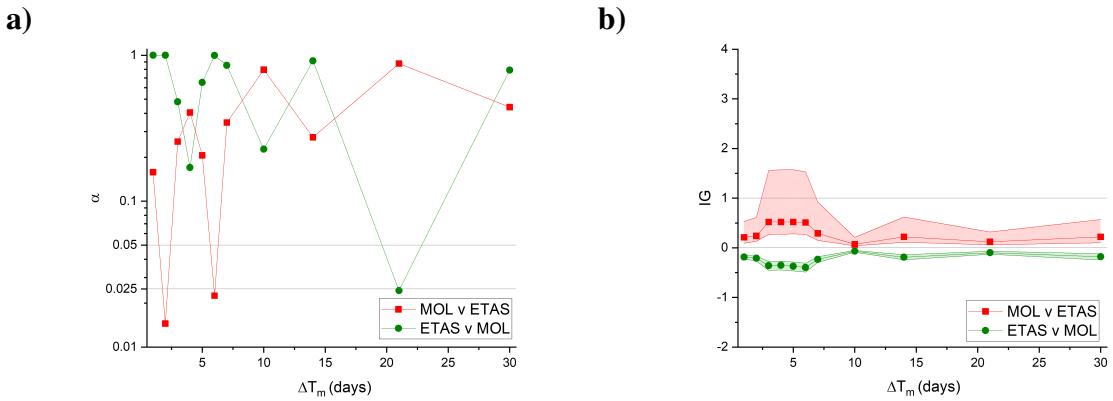

Figure 3.27: Results of the T-test and R-test as shown using relative information gain and quantile score α for the MOL and the ETAS model for the Monte Cristo Range sequence in figures a) and b), respectively.

days and ΔT_m = 21 days. These training time intervals coincides with the N-test performance, though there is no relationship between these two scores for the MOL test. Thus, the ETAS model forecast likely captured more details of the forecasted sequence and demonstrates this both in the N-test and the M-test. However, the information gain and R-test performance were not sufficient to reject the MOL forecast. The p-test performance for both models paralleled each other. The values on the p-test were slightly higher for that of the MOL.

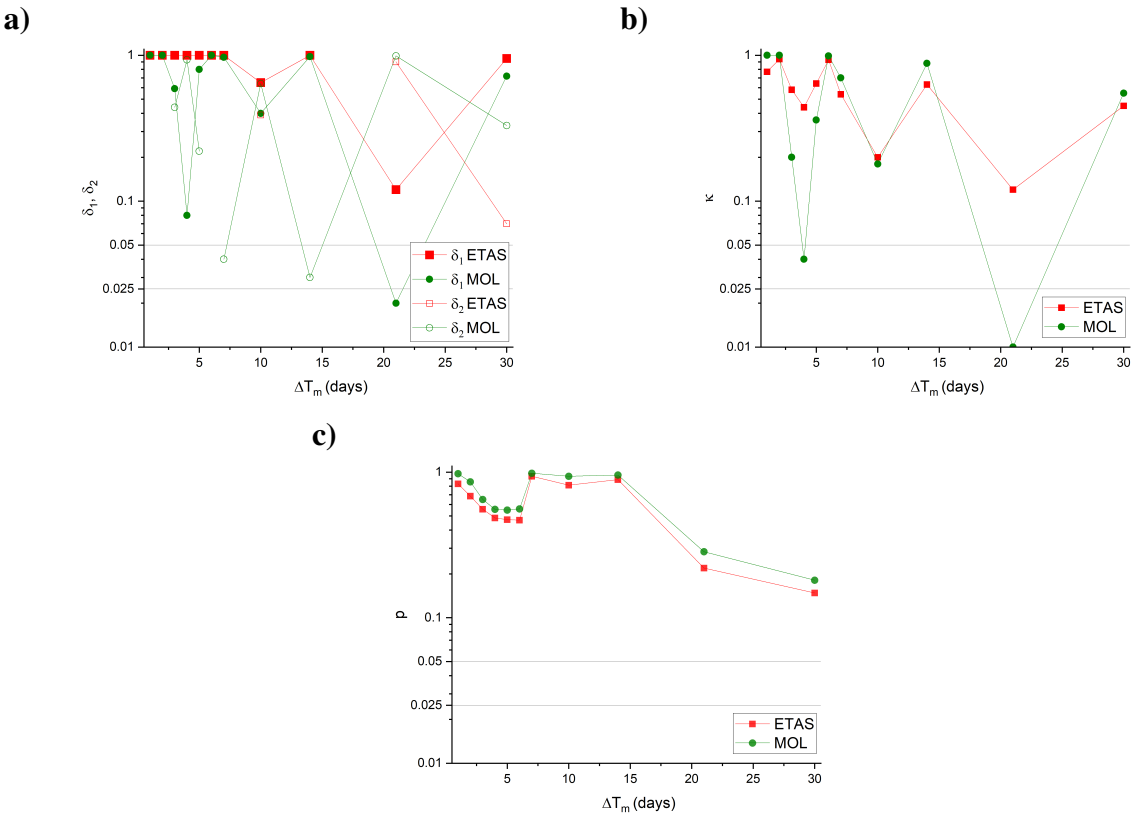

Figure 3.28: The performance of the ETAS and MOL models for various training time intervals for the Monte Cristo Range sequence. Forecast performance scores are listed for the N-test (δ_1, δ_2), the M-test (κ), and the Bayesian p-test in figures a), b) and c), respectively.

3.4.2 Discussion in Response to the Monte Cristo Range Sequence

Additional treatment for the Monte Cristo Range sequence was necessary in this work. This including the fixing of two parameters for the ETAS model, μ and K. In addition, the first two training time intervals also needed the c parameter to be fixed to produce MLE estimates similar to the remaining training time intervals. However, fixing one of the rate parameters implies knowledge of the sequence behaviour. During this work, the parameter estimates were also done using the MLE method with fixing only the μ parameter (see Tables B.22 and B.23 in Appendix B).

When only the μ was fixed, the target time intervals less than three days following the main-shock resulted in markedly different K parameter estimates in comparison to the remainder of the training time intervals. Thus, using the retroactive knowledge from generating the MLE

estimates for all of the training time intervals under consideration, the typical K parameter for this sequence was fixed to $K = 0.1$. Following this procedure, the c parameter was also found to be very different than the remaining time intervals. Thus, the c value for $\Delta T_m = 1, 2$ days was also fixed. Two potential explanations for necessary adjustments for this sequence are provided.

First, which is most natural, is that the sequence changes in behaviour such that the ETAS model parameters when solved find a different pattern in the data in the early aftershock sequence. This could be due to a physical change in the manner in which the earthquakes as part of the MCR sequence are being produced. Due to the changes in rupture pattern and seismicity, the data reflects the changes and leads to the model parameter estimates changing as well. Field work has shown that there are small surficial ruptures that are at an oblique angle to the main fault, demonstrating a physical irregularity [Zheng et al., 2020].

Second, the magnitude of completeness changes as the sequence develops. Based on personal communications, the additional seismic stations deployed to the site did not contribute to the catalog that was used in this work [Zeiler, 2021]. While the magnitude completeness could have been improved following the mainshock, this is not due to the additional stations that were added on site. Thus, the magnitude completeness assessed following data available from the first day after the mainshock should be considered suitable for the entire sequence. An improvement in catalog completeness is likely not the reason that the parameter estimation is unstable when using the MLE. However, it is also possible that the M_c estimation is incorrect and the early aftershock M_c is higher than was determined in this work.

The impact of these additional modifications was not evaluated in this study. However, the intermediate step which involving fixing of parameters would have directly impacted the forecasting and forecasting test results.

3.5 The 2010 Darfield Sequence and 2011 Christchurch Events, New Zealand

The 2010 Darfield sequence was initiated by a $M_w = 7.1$ mainshock on September 4, 2010. The mainshock and aftershocks took place along previously unmapped faults [Quigley et al., 2012]. The first 5 months of the sequence were relatively underproductive when compared to the New Zealand aftershock decay model [Fry et al., 2011]. On February 22, 2011 local time, 171 days later, the 2011 Christchurch earthquakes took place with two large aftershocks of $M_w = 6.2$ and $M_w = 6.0$ [Quigley et al., 2010, Shcherbakov et al., 2012]. The initial $M_3 = 7.3$ mainshock was associated with a surface rupture length of 29.5 ± 0.5 km [Quigley et al., 2012]. This mainshock and immediate aftershocks did not lead to any reported deaths. However, the 2011 Christchurch events lead to nearly 300 deaths [Fry et al., 2011].

The magnitude limit for large aftershocks during this sequence was also constrained in Shcherbakov et al. (2012) using the first 30 days of the catalog, though the probability of their occurrence was not evaluated. They also found that variation in the frequency-magnitude distribution was dependent on the time after the mainshock and was variable in different magnitude ranges. The confidence intervals for large aftershocks using the BPD for this sequence was estimated in [Shcherbakov, 2014]. In addition, this sequence was tested after the set up of the New Zealand Earthquake Forecast Testing Center using the GeoNet catalog [Gerstenberger and Rhoades, 2010]. The information gain for a three-month and one-day forecast compared in by Rhoades et al. (2018) indicated that the ETAS model showed the greatest information gain when compared to the other models, which were based on proximity to past earthquakes.

The 2010 Darfield earthquake sequence was analyzed in this work during the early aftershock sequence using the MOL and the ETAS models. The affected region is shown in the map (Fig. 3.29). The magnitude cutoff in the three days following the Darfield mainshock was found to be $M_c = 3.3$ by visual inspection (Fig. 3.30). As the sequence was prolific and had

many events above this magnitude, the same training time intervals were also evaluated for higher magnitude cutoffs of $M_0 = 3.5, 3.7$. By doing so, this sequence analysis addresses the limitations of the analysis methods for catalogs that have higher magnitude completeness.

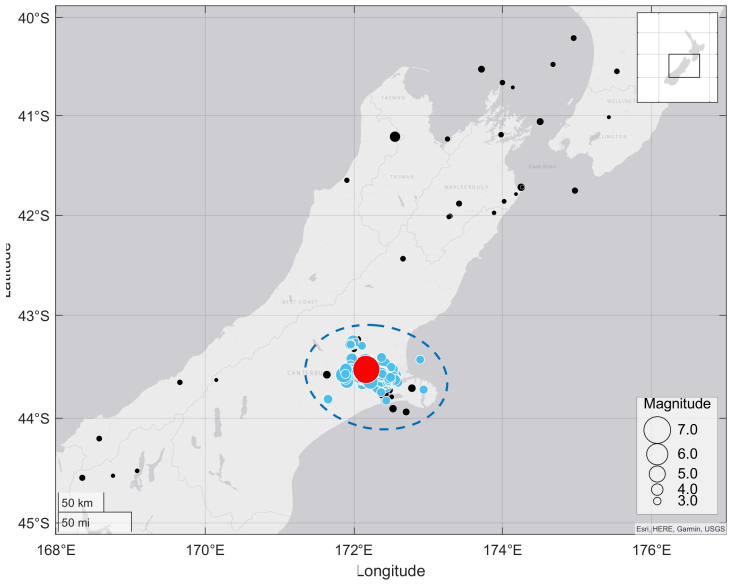

Figure 3.29: The 2010 Darfield sequence during the first three days following the mainshock for $M_0 = 3.3$. The blue circles indicate the events that are included in the analysis, and the black circles indicate events outside of the study region, or below the magnitude cutoff threshold. The mainshock is shown by the red circle. An inset map of New Zealand provides spatial context for the events.

The evolution of the sequence model parameter estimates for the MOL and the ETAS model with $M_0 = 3.3$ is presented in Figure 3.31. The corresponding point parameter estimates and MCMC sampling estimates are provided in Tables B.28 - B.32 in Appendix B. The results of the MOL and the ETAS model fits with training days $\Delta T_m = 3$ days relative to the mainshock are shown in Figure 3.32. The background seismicity rate was fixed to $\mu = 0.0$, and the prior mean for the MCMC sampling was set to $\mu = 0.001$. The model parameter estimates for $M_0 = 3.5$ and $M_0 = 3.7$ are available in Appendix B in Tables B.33 to B.36. Foreshocks for the Darfield sequence were not present and not included in the analysis. Both models begin at the mainshock with preparatory time intervals ending at $T_s = 0.001, 0.03$ for the MOL and ETAS model, respectively. This is consistent for all M_0 evaluated. As expected, the productivity

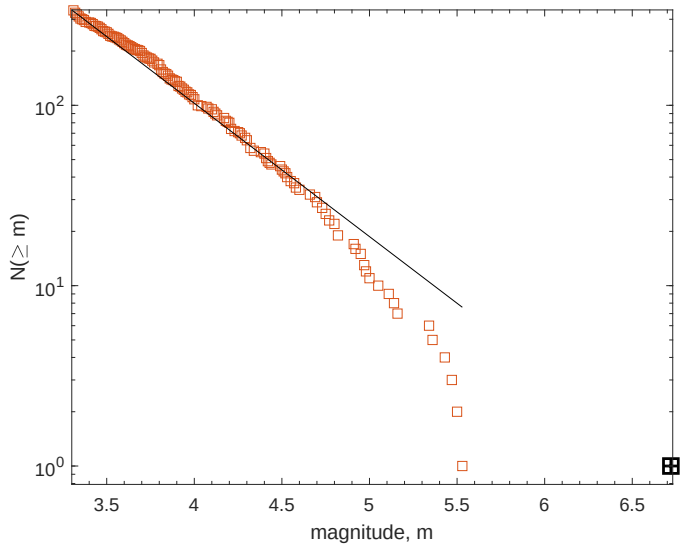

Figure 3.30: The 2010 Darfield sequence during the first three days following the mainshock for $M_0 = 3.3$ was fitted to the GR law. The events greater than the magnitude indicated on the x-axis are counted and plotted along a straight line.

parameters K_0, K, and α are different for the different magnitude cutoffs. K_0 decreases with increasing M_0. The relationship between K, α and M_0 is less obvious. However, K decreases from $M_0 = 3.3$ to $M_0 = 3.5$, while α increases. α decreases from $M_0 = 3.5$ to $M_0 = 3.7$. α is not related to the total number of events in the sequence, but rather the relationship between the events, which may be affected by changing M_0. The model parameters otherwise appear to be stable with increasing length of target time interval.

Forecasting using the different magnitude cutoffs demonstrated decreasing probability of large aftershocks as the training time interval increased (Fig. 3.33). A probability gain was seen in the ETAS model forecast for $M_0 = 3.3$ at $\Delta T_m = 2$ days and was likely due to model parameter stabilization as the parameter p decreased, resulting in slower seismicity decay. The MOL forecasts provide the upper bound for the probability of large aftershocks. The general behaviour of the probability of the largest aftershock was consistent across all of the M_0 (see Figures B.16 and B.17 in Appendix B).

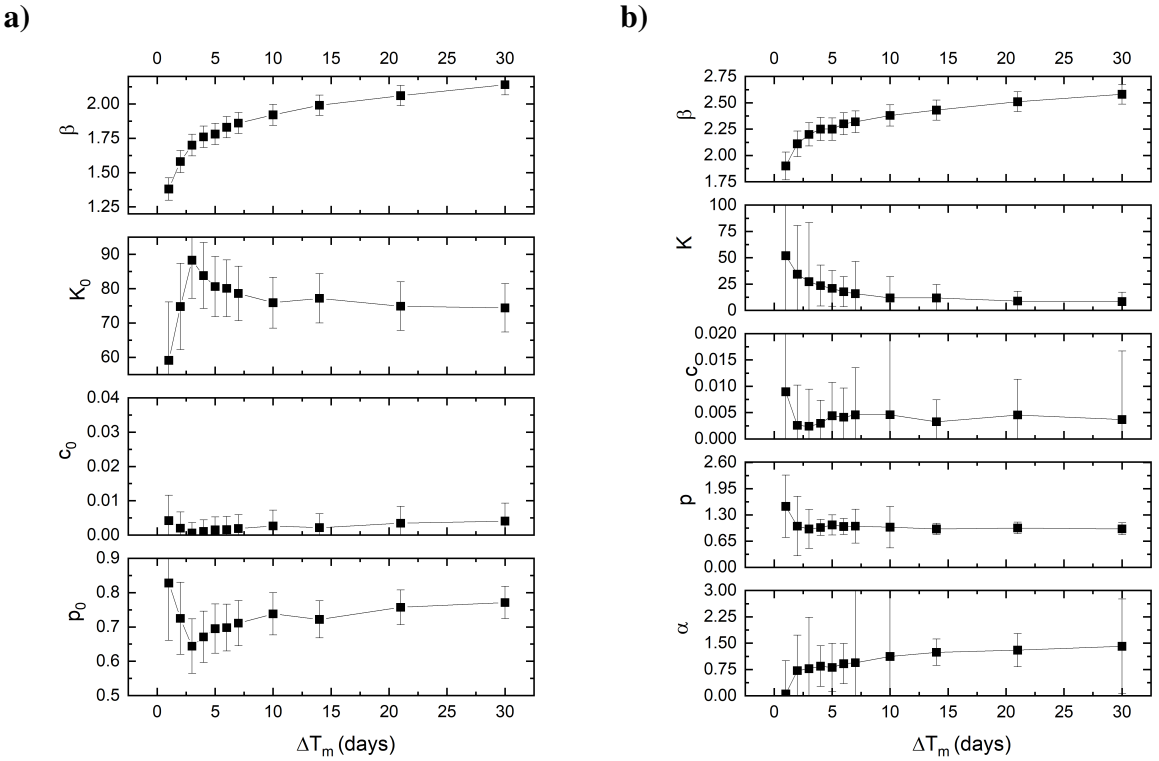

Figure 3.31: The model parameter estimates (black squares) for the Darfield sequence using the MLE with $M_0 = 3.3$ for various training time intervals ending at ΔT_m with corresponding 95% confidence intervals. The aftershock rate models used are the a)MOL and b)ETAS model.

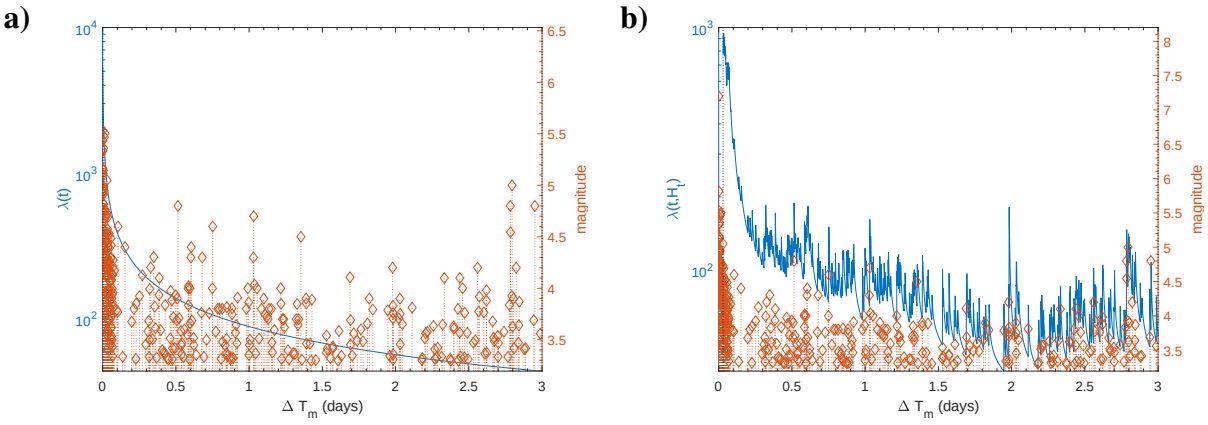

Figure 3.32: The aftershock model fit using the a) MOL and b) ETAS model to the Darfield sequence for $\Delta T_m = 3$ days. The events during this training time interval are shown with orange markers, where markers indicate the magnitude of the events (denoted on the right axis). The blue lines indicate the seismicity rate (left axis).

Considering the magnitude of the mainshock, the probability of large aftershocks such as $M \geq 6.0$ is surprisingly high. The high probability may be a reflection of the β estimates

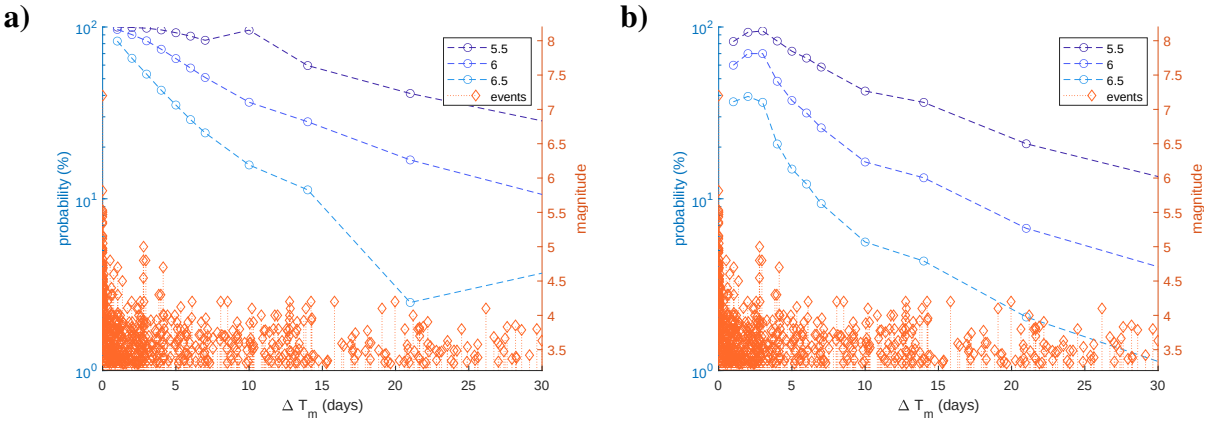

Figure 3.33: The probability of large aftershock of $M_{ex} = \{5.5, 6.0, 6.5\}$ during a seven-day forecast using various target time intervals for the Darfield sequence with $M_0 = 3.3$ is shown for the a) MOL and the b) ETAS model. The events are used in the training time intervals are shown with black diamonds, corresponding with their magnitudes (right axis). The probabilities are indicated at the end of the target time interval.

during the same training time intervals. The first training time interval for the MOL with $M_0 = 3.3$ returns an estimate of $\beta = 1.38$. At $\Delta T_m = 30$ days, $\beta = 2.14$. As the training time intervals result in similar magnitude distributions at the same training time interval, some general interpretations using the tests can be made. However, interpretations of the forecast test performance based on the evolution of the sequence will be affected by the evolution of β in addition to the rate models.

3.5.1 Forecasting Test Results

The forecast testing did not include the ETAS model for $\Delta T_m = 1$ day due to issues with model convergence not addressed in this thesis.

The ratio tests did not indicate whether one of the models was consistently superior. The information gain of the ETAS vs. MOL was consistently a negative value. However, in the MOL vs. ETAS test, the ETAS model was also rejected during some training time intervals as seen in Figure 3.34. This suggests that the ETAS model performs better than the MOL during specific training time intervals, but the comparative tests were not sufficient to identify the best model. This behaviour was consistent for all M_0 (Figs. B.20 and B.21 in Appendix B). The significance level α appeared to shift to lower or higher scores on the R-test with increasing

M_0, corresponding with the ETAS vs MOL and MOL vs ETAS comparisons, respectively.

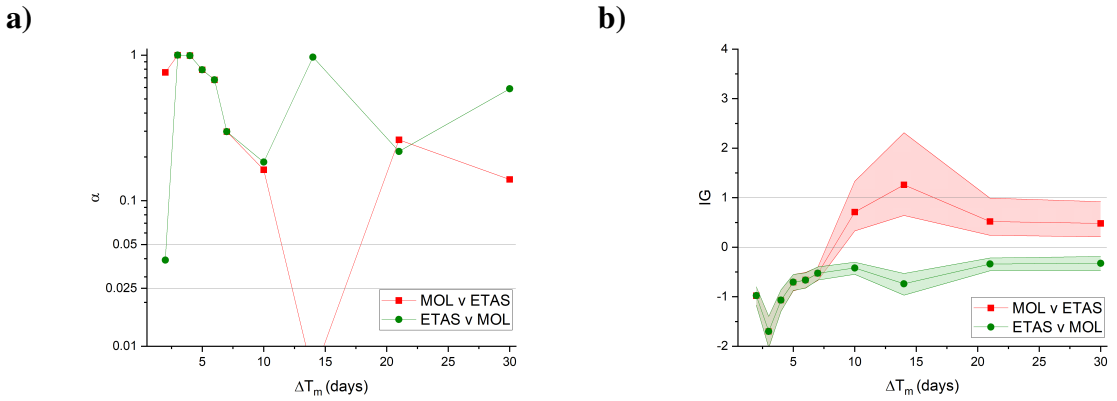

Figure 3.34: Results of the T-test and R-test as shown using relative information gain and quantile score α for the MOL and the ETAS model for the Darfield sequence with $M_0 = 3.3$ in figures a) and b), respectively.

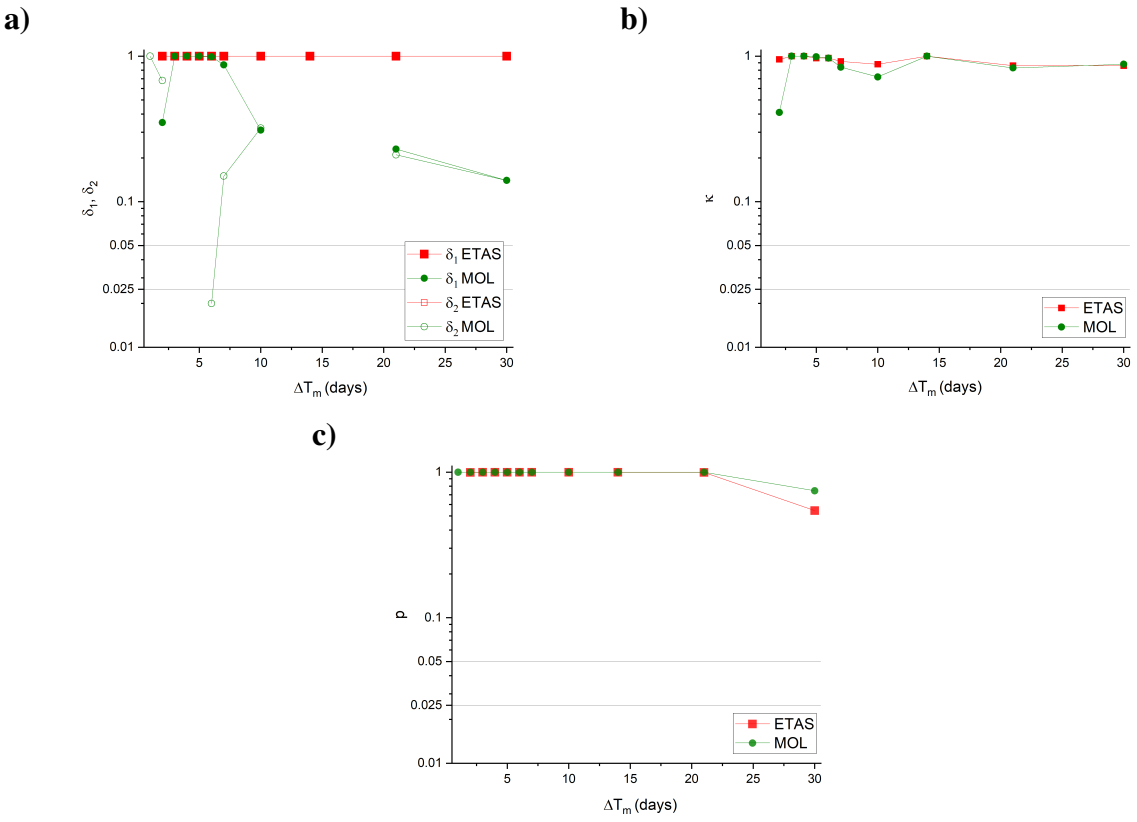

Figure 3.35: The performance of the ETAS and MOL models for various training time intervals for the Darfield sequence with $M_0 = 3.3$. Forecast performance scores are listed for the N-test (δ_1, δ_2), the M-test (κ), and the Bayesian p-test in figures a), b) and c), respectively.

The ETAS model consistently overestimated the number of events and the MOL demonstrated both over- and underestimation of the number of events during the forecast. Notably, the number of events was significantly overestimated at $\Delta T_m = 3$ days, providing context for the scoring on the comparative tests as $\Delta T_m = 3$ days coincides with the most extreme information gain on both comparisons. The MOL underestimated N_{obs} following $\Delta T_m = 1, 2$ days, suggesting that the sequence did not provide sufficient information for fitting to Omori-like behaviour during these training time intervals or the evolution of the sequence was not suitably accounted for using the MOL (Fig. B.15). Both models are unable to correctly forecast the decrease in N_{obs} following $\Delta T_m = 3, 14$ days. Both models also improved on the N-test with increasing M_0. The underestimation of events was greater for the MOL at $M_0 = 3.7$, which indicated that the magnitude cutoff and completeness may have had larger impact on the MOL.

Both models typically passed the M-test for $\Delta T_m \geq 1$ day. Performance on the p-test for both models at all M_0 was very high, with extreme quantile scores near or at 1.0. The evidence for the ETAS model as the best model was not as clear as the results demonstrated in Rhoades et al. (2018) for comparison to different models, though their results did not include a comparison to the MOL.

3.5.2 Forecasting the 2011 Christchurch Event

The forecasts using $T_e = 170$ days suggest that none of the models fitted to this prolonged segment of the sequence demonstrated predictive power for the $M_L = 6.2$ event. Neither the MOL nor the ETAS model forecasts indicated that there was an increased probability of large events shortly before the 2011 Christchurch earthquakes. The probability of a large aftershock occurring by using the target time interval $\Delta T_m = 170$ days, 1.3 days before the first Christchurch event, was 0.9% and 0.4% for the MOL and ETAS models with $M_0 = 3.3$, respectively.

It has been suggested that the occurrence of very large aftershocks that appear to be part of a separate aftershock distribution, as with the Darfield sequence and the subsequent Christchurch events, is likely because they take place on separate faults [Beavan et al., 2012,

Shcherbakov et al., 2012, Shcherbakov et al., 2018]. Thus, forecasting based on the aftershock distribution prior to the large Christchurch events may not be as useful when forecasting the aftershock on a separate fault.

Chapter 4

Discussion

In the previous chapter, five case studies were presented. These include the 2009 L'Aquila, Italy (LAQ), 2016 Amatrice, Italy (AMA), 2016 Kumamoto, Japan (KUM), 2020 Monte Cristo Range, USA (MCR), and 2010 Darfield, New Zealand (DFL) sequences. The sequences took place in a variety of tectonic settings and governance regions that use different approaches and models for forecasting. The forecast testing methods in this work were used to address some of the questions posed by the goals of this study. To do so, an analysis of the aftershock model forecasts for each sequence was provided. Scoring on the forecast performance tests indicated whether one of the models performed consistently better during forecasting. During this process, some limitations to the methods were observed. Lastly, the magnitude cutoff M_0 impact was reviewed by evaluating the Darfield sequence at three different M_0 values. By increasing the magnitude cutoff, the number of available events for analysis changed both the forecasted probability of large events, as well as the forecast test results.

In this thesis, the temporal aftershock rate models - the modified Omori law (MOL), compound Omori law (CMOL), and the Epidemic Type Aftershock Sequence (ETAS) model - were applied to all of the sequences where reasonable. Despite the large range of confidence intervals in the initial maximum likelihood estimate (MLE) method, the model parameter fits for the rate models appeared to be reasonably fitted based on the observed model parameter stabil-

ity with increased training time intervals and the associated error also tends to decrease. The frequency-magnitude as described by the Gutenberg-Richter (GR) law resulted in b-values and corresponding β in the typical range for events during the training time interval above M_c, with the exception of the Darfield sequence which is addressed separately. No special adjustments were needed for the MOL fitting procedure. The CMOL required user selection of the time of the second MOL instance when it was not associated with a mainshock. The ETAS model required adjustments to the training time interval and fixing of model parameters in some instances to stabilize the parameter estimates when using the MLE method. These adjustments naturally also impact the Markov Chain Monte Carlo (MCMC) sampling procedure as the prior for the MCMC sampling is based on the MLE estimates.

Forecasting for large aftershock probabilities was done with the extreme value distribution (EVD) and Bayesian predictive distribution (BPD) methods for the MOL and CMOL. The ETAS model forecasts were done using the BPD method. From the EVD and BPD forecasts for the MOL, it was evident that the model parameter estimates and forecasts do not require the BPD method, confirming that the EVD using the Gumbel distribution is a close representation of the BPD forecast [Shcherbakov, 2014, Shcherbakov et al., 2019]. This was also seen with the CMOL. When using the EVD, the probability of a large event is similar to that of using the BPD. Thus, for forecasting a large aftershock fitted to the MOL or the CMOL, the EVD is likely sufficient. One notable exception was the early training time intervals of the Kumamoto sequence where the forecast of the EVD and BPD produced different forecasts. During forecast performance tests, the EVD and the BPD resulted in slightly different scores, most notably close to the effective significance cut-off. Thus, for forecast testing, the BPD is necessary to evaluate the performance of the MOL and CMOL forecasts.

For the ETAS model, the BPD method is critical to fully integrate the uncertainty around the model parameters as the model rate is stochastic [Shcherbakov et al., 2019]. By using the BPD method for the ETAS model, there is an increase in the time required to estimate the model parameter distribution with a reasonable number of steps during MCMC sampling in

comparison to using the EVD for the MOL or CMOL. While no metric was developed to assess the computational cost of testing the ETAS model forecasting, using the full BPD forecast requires simulations for the ETAS model and will take more time producing the MOL and the CMOL, where each chain can be forecasted using the EVD. For example, using a desktop with Intel(R) Core(TM) i7-5829K CPU @3.30GHz with 6 cores and 12 logical processors required up to 30 hours for simulating the BPD for the 200,000 MCMC chains for certain training time intervals. The same simulation conditions for the MOL can be completed under 15 minutes as the forecasting procedure for the MOL takes advantage of the EVD method and does not require a full simulation as the forecasted rate can be directly calculated from the model parameters. During forecast testing, the full simulation produced by the MCMC chains is used. The ETAS model forecast testing takes on the order of 10 times more computational time than that of the MOL and the CMOL. The computational time is also affected by the model parameters themselves. For $\alpha \propto \beta$, it is expected that the ETAS model parameters lead to a critical simulation and the simulation runs until the number of events generated during the forecast reaches the user selected cutoff for simulation.

4.1 Interpretation of Forecast Tests

The results of the N-test are straight-forward to interpret. Since they are single-sided tests, it is clear when the percentage of simulations produce simulated events N_{sim} which exceed or are below the observed events N_{obs}. A good forecast will sometimes exceed and sometimes produce a lower number of forecasted events in comparison to the observed number of events. When determining the best model, the interpretation of the forecast tests and model forecast performance is likely to be correct if the N-test is passed on both sides. Since this was not the case for most of the forecasts for the case studies, with all models producing scores of $\delta_1 = 0$ or $\delta_2 = 0$ at various training time intervals, the δ scores were evaluated separately and the N-test results were used to support the results of the comparative R-test.

The M-test checks if the β value that was estimated is representative of the sequence during

the forecasting time period. The number of forecasted events is scaled to match the number of observed events, so the quantile score κ is not affected by the model rate parameters. While the GR law assumption is not tested explicitly by the M-test, and it is assumed that the frequency-magnitude distribution is correct, the M-test may provide context for the N- and p-test results. As the ETAS model forecast simulation for N_{sim} is dependent on the magnitude of simulated events, estimated β which does not reflect the ΔT portion of the sequence may lead to different results in the seismicity rate, and subsequently, the forecasted probability of large aftershocks. A poor score on the M-test for the ETAS model can also provide a partial explanation for the N-test performance as the parameters estimated during the target time interval are used for forecasting, and the forecast is related to the β values estimated during the training time interval. The model parameter estimates for the ETAS model do not account for the estimated β during the training time interval. Thus, if β does not match to the frequency-magnitude distribution during ΔT, the performance of the ETAS model on the N-test and p-test may be directly impacted. The MOL and CMOL seismicity rate are unaffected by β. Passing and failing of the N-test with the MOL or CMOL are dependent only on the rate parameters. However, the training time intervals for the MOL and CMOL are slightly longer than the ETAS model. Thus, difference in the estimated β value during the training time interval may also be reflected on the M-test scores.

The compiled results of the N-test performance for the case studies are shown in Figures 4.1 and 4.2. From the results, it can be seen that the ETAS model tends to overestimate the number of events during the forecast, and the MOL and CMOL forecast rate are variable as the sequences progress. This is expected as the ETAS model is self exciting whereas the MOL and CMOL describe a consistently decaying rate. In addition, some of the sequences maintain a persistent rate of background seismicity throughout the target time intervals that was not captured by either the MOL nor CMOL. The ETAS model was also found to be more suitable in terms of predicting the number of events that may occur when secondary aftershocks are present (i.e., when the CMOL can be applied). The ETAS model was good at estimating the

number of events when the sequence had Omori-like behaviour, such as in the case of the Monte Cristo Range sequence.

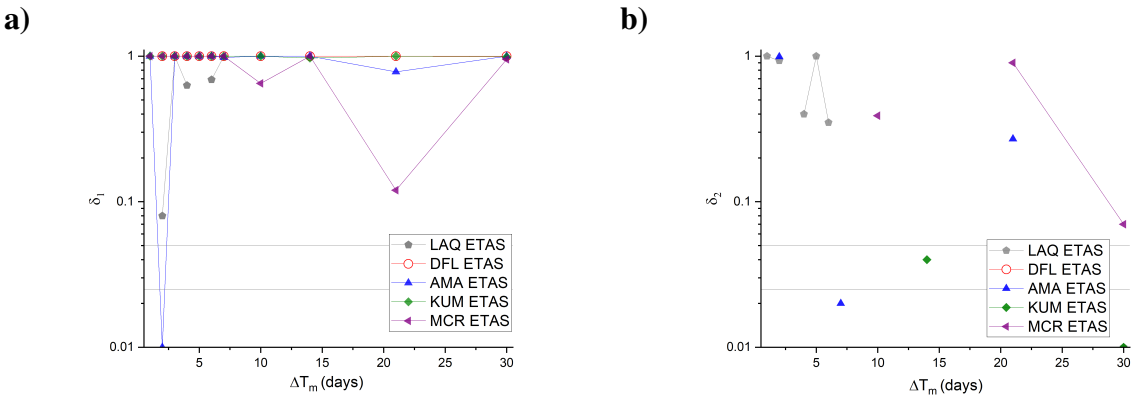

Figure 4.1: Plot of the N-test performance for all of the evaluated sequences when fitted and forecasted with the ETAS model using the BPD for forecasting. The abbreviations correspond to the following sequences: LAQ - 2009 L'Aquila sequence, DFL - 2010 Darfield sequence, AMA - 2010 Amatrice sequence, KUM - 2016 Kumamoto sequence, and MCR - 2020 Monte Cristo Range sequence. Note that forecasting was not completed for $T_e = 1$ day for the Darfield sequence. The remaining scores of the Darfield sequence are $\delta_1 = 1.0$ and hidden under the other scores. Values that are not plotted were calculated to be $\delta = 0.0$.

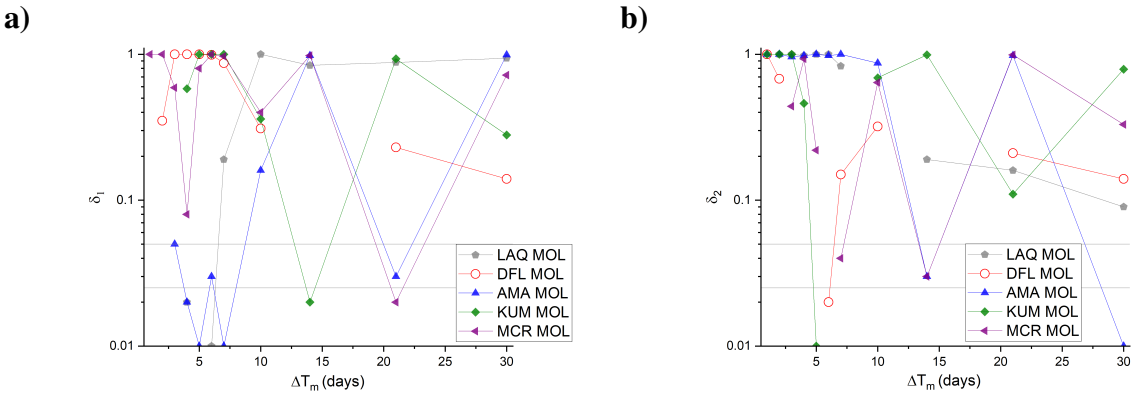

Figure 4.2: Plot of the N-test performance for all of the evaluated sequences when fitted and forecasted with the MOL using the BPD for forecasting. The abbreviations correspond to the following sequences: LAQ - 2009 L'Aquila sequence, DFL - 2010 Darfield sequence, AMA - 2010 Amatrice sequence, KUM - 2016 Kumamoto sequence, and MCR - 2020 Monte Cristo Range sequence. Note that values that are not plotted were calculated to be $\delta = 0.0$.

The ETAS model was found to pass the M-test more frequently than the MOL and CMOL. This is likely an artefact introduced from the training time interval selection which is inherent to

the modelling procedure. The trade-off of decreasing or increasing T_s and T_0, and subsequent impacts on κ was not investigated in this study. There were no significant differences of the β value from the MLE method to the MCMC method. Thus, the performance on the M-test is likely due to the training time intervals selected.

In addition, N_{avg} from the simulations for the ETAS model appeared to be closer to N_{obs} events. However, for shorter target time intervals the ETAS model typically failed the δ_2 side of the N-test and overestimated the number of events during the forecasting time interval. The MOL tended to underestimate the number of events during shorter target time intervals relative to that of the ETAS model. For longer training time periods, the CMOL underestimated the number of events close to the initiation of the second MOL instance. For longer training time intervals, the MOL and the CMOL produced similar forecasting results and test performance on the N and M-tests.

For the R-test and the T-test, the interpretation is done in conjunction. There were several instances where both models passed the R-test. Passing of the R-test is affected by M_0, as the performance on the N- and M-tests also changes with M_0. For the T-test, sample information gain per earthquake (IG) with positive values $IG \geq 0$ indicated that reference model performs better than the alternative model, and $IG \geq 1$ indicating significant information gain of the reference model when compared to the alternative model. In the case where IG is small, then the models do not differ significantly and it is unclear which of the models performs better.

The supporting T-test did not result in consistent information gain as the training time intervals increased for all of the sequences for comparison of the ETAS model and the MOL. This suggests that as the sequences evolved, the relative forecast performance of the models was not strongly consistent. For example, when the ETAS model demonstrates $IG \geq 1$ for a short training time interval, if the information gain drops below 1 at the next training time interval, then the ETAS model is not necessarily the "better" model for the sequence. During time intervals with very low information gain, neither model is considered better by the T-test. A negative information gain On the T-test, the ETAS model was found to perform better as

the information gain was positive for four of the five sequences on the MOL vs ETAS tests. However, most of the T-test IG values were not above one. Thus, it cannot be stated that the ETAS model is the better choice of model, even if the performance appears better on the test. In most cases, with the exception of the Darfield sequence which shows a shift between model performance, when the second model hypothesis produces a positive score during the first three training time intervals, the remaining training time intervals remain positive for that specific model comparison.

Considering that the T-test performance tends to be consistently positive or negative, the early T-test results can be used to determine which model is likely to have better performance for longer training time intervals. In particular, if the information gain indicates that the MOL performs better during the early aftershock sequence, then this model can be prioritized or used as the baseline model when evaluating forecasts. Use of the ETAS model for forecasting under these circumstances should be well justified with either incidences of clustering events or clear departure from Omori-like behaviour.

When the MOL demonstrates better performance based on the T-test (such as for the Monte Cristo Range sequence), the ETAS model still performed reasonably well on the N and M-tests. Thus, the ETAS model cannot be entirely disqualified based on the comparative tests as a "better" model for an ongoing or new sequence. In this study, there was no instance of the CMOL performing better than the ETAS model in the comparative tests. The performance of the ETAS and the CMOL on the other tests do not indicate that the CMOL is better than the ETAS model when forecasting.

Lastly, the Bayesian p-test evaluated whether the maximum magnitude earthquake in the observed events was likely to occur in the forecasted events from the simulation. This test is limited in the context it provides if the number of forecasted events is significantly greater or less than the number of observed events during ΔT. A value close to one, indicating a near perfect score, requires additional interpretation. In the results, it is apparent that most of the models in this study pass the p-test for most of the training time intervals. For extremely high

scores, such as those $\geq 99\%$, the scores can be related to the performance on the N-test and the average number of simulated events N_{sim}. Since the p-test is not scaled like the M-test to match the number of observed events, the high quantile score may be the result of simulating more events than were observed, and allowing for greater opportunity for an extreme event to happen. However, good performance on the p-test occurs even in instances where the model underestimates the number of forecasted events. The exception to this is for the MOL for very short training time intervals where the MOL greatly underestimates the number of forecasted events.

If both sides of the N-test are passed, and the p-test results in a high quantile score, then the model in question performs extremely well. If δ_1 is failed in the N-test and the p-test score remains high, this suggests that the performance on the p-test is unreliable and the score is artificially improved by the β-value which is non-representative of the forecasting time interval. If the model has failed the p-test and the δ_1 score on the N-test is below the significance level, then a failed p-test does not provide any additional information.

The results of the p-test suggest that the ETAS model typically passes and produces extreme values near one. In several instances, this can be explained by generating more events on average than N_{obs}. In addition, the choice of β may influence the magnitude of simulated events as evidenced by the M-test. On the other hand, the MOL typically passes the p-test as well, despite having fewer instances of forecasting more events than observed. Thus, the MOL is capable of achieving a high frequency of forecasting an event greater than or equal to the largest event observed even when the ETAS model demonstrates more information gain over the MOL and performs better on the M-test. The CMOL performance was similar to the MOL. When considering the performance of the p-test independently of the other tests, the p-test is not sufficient to distinguish which one of the models performs better. However, in conjunction with the N-test, the p-test can indicate whether the largest magnitude event was successfully forecasted due to overestimation as a consequence of the magnitude-frequency statistics from the training time interval, or good performance from the aftershock rate model.

In comparison of the CMOL to the MOL fitted to the first large shock, as with the L'Aquila sequence, the MOL forecasts performed better than the CMOL for the short duration and training time interval following the second large shock at time τ. Additionally, the probability of large magnitude events for the MOL forecast was typically higher than that of the CMOL with the exception of the immediate training interval following the second MOL instance.

In the case of the Kumamoto sequence, the CMOL demonstrated better forecasting test performance than the MOL for most of the training time intervals. This is unsurprising as the mainshock of the Kumamoto sequence is an order of magnitude larger than the shock that initiated the foreshock sequence. The large increase in seismicity cannot be easily "absorbed" by the MOL and greatly alters the parameter estimation.

When the MOL is fitted to the second large shock during an ongoing sequence, the MOL was more suitable for the training time period shortly after the large aftershock. Once the CMOL parameters were stabilized, then the CMOL shows slight information gain over the MOL. The short term secondary aftershocks in this instance do not warrant significant attention, as was with the L'Aquila sequence. For the L'Aquila sequence, the MOL performed better than the CMOL for shorter training time intervals and has similar performance for training time intervals $\Delta T_m \geq 10$. This was also evidenced by the ETAS models, where the parameters do not change near τ and sufficiently describe the remainder of the sequence. Thus, the CMOL is less suitable for forecasting shortly after a large aftershock unless the second MOL instance can be characterized well early on. This is not surprising, as there may be insufficient data close to the second shock to distinguish which events are contributed by which shock. This might be particularly difficult when the two shocks are close together.

This suggests that the CMOL is either more difficult to estimate and describes the second shock productivity inaccurately when there is limited data, or that the use of the CMOL introduces an artefact that suggests the second shock is associated with its own aftershock sequence, when the contributions to the rate are not significantly elevated to warrant a second instance of MOL. This result was also suggested in [Shcherbakov, 2021] for the Ridgecrest 2019 sequence

which also had the mainshock take place during the aftershock sequence.

4.2 Limitations and Assumptions

Several limitations of this work are noted. These include the impact of prior information, the expectation that the GR law sufficiently describes both the past and future magnitude distribution, the completeness of the catalog, and choice of forecasting time period ΔT.

The M_c sensitivity was explicitly explored with the Darfield sequence. M_0 was used as a proxy for the completeness of the catalog for the Darfield sequence. Based on the forecasted probabilities for large aftershocks, it is evident that increasing the M_0 reduces the probability of large events. The forecasting test results do not change dramatically and the interpretation of the tests remains the same. This suggests that the testing implemented in this work is applicable for catalogs and sequences with higher magnitude completeness. This includes catalogs not used in this work.

4.2.1 Completeness

The results in this study are based on the assumption that the catalogs are complete above M_c. Where possible, the M_c selected in this work are the same or greater than that of previous works. However, it may be that the true M_c is higher and the selected M_c are based on faulty assumptions which then impact the model parameters and subsequent analyses. To improve the completeness of a catalog and lower the M_c, it is possible to backfill events to a desired level of completeness [Zhuang et al., 2011].

As seen with the Darfield sequence, a shift in M_0 results in an adjustment with the rate based parameters K and K_0, ain addition to the α parameter. α changes in such a manner that the aftershock behaviour described by the ETAS model is different. If the M_0 is set higher, the Darfield sequence behaves more Omori-like. Based on this one example, it could be suggested that the MOL is sufficient to describe sequences with higher magnitude completeness of the catalogs. The uncertainty for the ETAS model parameters also increases with increased M_0. Previous works have shown that higher M_c reduces the contributions of the

ETAS model to the seismicity and results in lower probability estimates for large aftershocks [Helmstetter and Sornette, 2003].

While the forecasted probability of large events changes, the forecast testing indicates that the forecast performance was similar for all of the M_0. The training time intervals that fail the $N-$ and $M-$ forecasting tests are consistent across the M_0. The N_{avg} plots indicate over- and underestimation at consistent training time intervals. Thus, assuming that the catalogs are complete and there is sufficient events to fit the models, the effect of M_c is primarily on the probability of large events. None of the selected M_0 for the sequence were able to forecast with high probability known large events several months following the mainshock. When examining the R- and T-tests, there was a strong shift in the quantile score for the R-test and relatively scaled values on the information gain. This supports the suggestion that for regions with less complete catalogs and higher M_c, the probability of large aftershocks may be underestimated when using either the ETAS model or the MOL. Regardless, the ETAS model in this case still performs better than that of the MOL.

Given that the aftershock probability decreases for both models with increased M_0, the change in forecast appears to not be related to the choice of model and rather the data availability. The relative information gain between the competing models was also decreased at higher M_0, suggesting that with less data available, the difference between using the ETAS model and the MOL becomes less significant.

Completeness of the sequence is also dependent on the spatial selection of events. In this study, it was assumed that an elliptical shape was adequate to provide coverage and contain the events of interest. To account for events taking place on nearby faults and to include as many events related to the sequence as possible, the ellipse size was increased by including an additional buffer zone. Thus, it is possible that events not related to the sequence were also included during analysis. This was addressed by using several different elliptical regions prior to selecting the apparent best visual fit to minimize the impact of the regional selection. Some differences are noted: the Darfield region used in this study is larger than the zone

indicated in [Shcherbakov, 2014] and encompasses the 2011 Christchurch events; regions for the Amatrice sequence and the L'Aquila sequence used are elliptical in comparison to the spatiotemporal studies in [Marzocchi and Lombardi, 2009] which use a gridded system; and, the Kumamoto sequence shares the same elliptical region as [Shcherbakov et al., 2019] using an updated catalog with more events. Given the fairly short target time interval for the case studies, it is unlikely that the addition of a few small events greatly changes the parameter estimates.

The results of this work may have been impacted by both the spatial constraints imposed and the selected M_c. However, the impact of the catalog refinement was assumed to be minimal when considering the work done prior to the analysis to limit the impacts and the choice of M_c which aligns with previous analyses.

4.2.2 Prior Information

For all of the models, the BPD process is impacted by the use of prior information from the MLE parameter estimate. The MLE results in a point parameter estimate that does not reflect the other possible local minima results. Since the MLE results are used for setting the mean prior of the MCMC process and BPD method, poor solutions from the MLE method can affect the downstream processes, including the forecasting.

The specific BPD procedure for the ETAS model in this study would be restricted to real-time situations where one can be fairly confident that the MLE produces parameters which closely estimate the mean of the true model parameter distribution. This can be complicated by the choice of initiating parameters, as poor initiating parameters may lead to locally optimal solutions for the MLE. Use of prior and retrospective knowledge were also used in this work to assist in the convergence of model parameter estimates, which is not always representative of real-time forecasting conditions. In addition, the MCMC procedure uses a user determined variance in this work. If the prior distribution does not align with the true parameter distribution, then the fit will produce a forecast that is not representative of the training sequence. During this work, no obvious instances of this occurrence were observed.

In some instances, the MCMC sampling process shows that the sampling deviates from the prior despite the constraints for certain training time intervals (for example, α for the L'Aquila sequence ETAS fit for most training time intervals, see Table B.5 in Appendix B). This can show that either the MLE estimate is not representative of the other solutions that may better represent the sequence activity. This includes parameters with bimodal distributions and shifted sample distributions despite the strong prior constraints. Another concern during MCMC sampling is when the prior pushes the sample towards smaller values and results in changing the shape of the prior. This happens when the variance is too large relative to the mean. In this study, the prior distribution shape change occurred when the parameter estimation for some of the training time intervals was significantly different than the other point parameter estimates and was very small. The variances are chosen so that most of the Gamma priors will have a normal-shaped curve for the prior for all the training time intervals. In the instances where the variance was not sufficiently small to produce the normal-shaped curve, it was assumed that the MLE estimate did not represent the true behaviour of the sequence well. The impact this has on the probability for large aftershocks appears to be negligible in these case studies as the probabilities typically behave in a standard pattern of decreasing over time.

4.2.3 Background Seismicity Stationarity

It is assumed that μ is constant for the training time interval and is the same or close for the forecasting time interval. This is typically a reasonable assumption particularly when μ is a consistent value prior to and during the training time interval. For the Monte Cristo Range sequence, the μ estimates prior to fixing the value were unstable and varied widely (Table B.22 in Appendix B). This suggests that there are instances of μ that can be difficult to solve for and estimations of μ may change dramatically depending on the available sequence data. Thus, preconditioning of the model parameters may not always be suitable nor a good representation of the sequence. Depending on the sequence, it may be important to stabilize the model parameter estimates by extending the training time interval for estimation of μ, as with the L'Aquila sequence, or to fix μ to improve parameter estimation stability, as with the Monte Cristo Range

sequence. The fixed background rates were confirmed by estimating the background seismicity manually for the same region over long periods of non-sequence-like seismic behaviour. However, the productivity parameters may be elevated if the μ estimation is too low.

When μ varies before and during the sequence, such as with the Amatrice sequence which produces μ values slightly greater than zero in comparison to the little to no seismicity immediately prior to the sequence, then the assumption that μ is stationary may be inadequate, leading to poor estimates of other model parameters. The μ parameter for the BPD estimate is heavily affected by the prior value, and thus the variability in the parameter is not completely accounted for during the MCMC sampling [Shcherbakov et al., 2019]. If the background seismicity rate is not very high, the impact of this assumption is not very big in terms of forecasting.

4.2.4 Forecasting Time Interval

In this study, the length of the forecasting time interval was set to $\Delta T = 7$ days. $\Delta T = 7$ was considered a reasonable time frame to demonstrate the short-term forecasting and investigate whether the forecasts could account for potential future variability in the sequence. This provides an obvious limitation to the forecast test performance evaluation, as the characteristics of the forecasting may not be well represented by only one interval. While the limitation is not addressed directly, the evolution of the sequence, events during the forecasting time interval, and the corresponding analysis were incorporated by using incremental increases in the training time intervals.

The overestimation in the forecasts which is more commonly seen with the ETAS model may be due to the parameter estimates during the very productive early sequence. By adjusting the forecasting time to be longer, the simulated events may result in a closer average to the observed events. Reducing the forecasting time interval may lead to poor estimations in the very short term but may demonstrate how well each model performs when forecasting imminent aftershocks and their behaviour.

Due to time restrictions, this work does not include analysis for both shorter and longer forecasting time intervals. However, the methods used in this work applicable to other ΔT. An

example of the impact of ΔT can be found in [Shcherbakov et al., 2019]. It is expected that if the model parameters fit well, then there would be a general tendency for the forecast to perform better on these tests as irregularities and punctuation of events can be averaged out over a longer forecasting time period. To compensate for reduced performance on longer training time intervals, the use of greater ΔT may result in a better in better forecasting. While this reduces the functionality of short-term forecasting, this is a sensible approach once the sequence has progressed for a longer period of time and the concern of imminent large aftershocks is lower.

4.2.5 Additional Temporal Conditions

Temporal models are dependent on the time intervals selected for training. The estimates of the model parameters are based on the events taking place in the entirety of the training period. This includes the often high density events in the early aftershocks close to the mainshock. As was seen in Chapter 3, the parameter estimates for all of the models have instances where the parameters change, particularly around three days after the mainshock. The change in parameter is moderated by the fit close to the mainshock, even when it is clear that there is a distinct or rapid taper towards the tail end of the aftershock sequence. For longer aftershocks sequences, such as those that continue for over a month and demonstrate clustering of events, use of the MOL is not recommended as the p-value may change to account for new events, but still lead to very low probability of future events.

In terms of the ETAS model, the model has a built in conditioning statement that is based on past seismicity. Due to the construction of the ETAS model, it is possible to not condition the rate if there is a sufficient justification to do so. In [Gerstenberger et al., 2005], they assume that each shock above $M \geq 3.0$ could potentially have an aftershock sequence. The ETAS model better incorporates this possibility.

4.2.6 Limited Use of Compound Omori Law

One of the limitations of this study is the infrequent use of the CMOL. In the case studies, the clear secondary aftershock sequence following a large aftershock that is not the mainshock is not always seen and the CMOL is applied only to two of the five case studies. Because of the limited results with the CMOL, the interpretations are limited. As many of the case studies did not demonstrate aftershock activity indicative of secondary aftershocks strongly associated with a large event, the CMOL was unnecessarily complex for most of the sequences and did not need to be implemented for forecasting. The exception to this is if the MOL drastically changes in model parameters following a large aftershock, such as in the case of the delayed mainshock.

For real-time applications, the choice of applying the CMOL as the best model for the situation has additional complications. Firstly, there is no prescribed method to choose which event that is producing the apparent secondary aftershocks. This is the case of the Amatrice sequence, where the large aftershocks did not produce distinct sequences when fitted to the CMOL for the target time periods considered. The only obvious case for fitting the second instance of MOL for the CMOL is when the mainshock takes place later than the sequence initiating shock. As seen with the Kumamoto sequence, some time needs to pass from the initiation of the second aftershock sequence for the model to distinguish the components of the CMOL.

Chapter 5

Conclusions

For many sequences, the Epidemic Type Aftershock Sequence (ETAS) model describes the rate better [Ogata, 1988, Shcherbakov et al., 2018]. As the most popular stochastic model describing earthquake occurrence [Lombardi, 2015], the choice of the ETAS model over the modified Omori law (MOL), a commonly observed law, should be justified in a quantified means. In this work, the compound Omori law (CMOL) forecast performance was also shown. As both the CMOL and the ETAS model are extensions of the MOL,there is a trade-off between the increasing complexity of the model and the potential the information gain. In addition, the forecasting method for the ETAS model is necessarily the Bayesian predictive distribution (BPD), which is significantly greater in complexity and more computationally demanding than solving the BPD for both the MOL and the CMOL. The BPD process results in a similar forecast to that of the extreme value distribution (EVD) for the MOL and CMOL, so it is not necessary to use the BPD method for those two models. Lastly, the ETAS model may also require more expert knowledge or prior information for stable parameter estimates than the other two models. When choosing which model to use for forecasting, it would be ideal if the model has been tested using standard tests and there is high confidence that it performs better than the other options.

Based on the results in Chapter 4, there is no single model that is consistently superior

to the other models. However, in most of the case studies, the ETAS model performs better than the MOL and CMOL on the ratio tests with at least marginal information gain. When the CMOL was applied to a foreshock-mainshock sequence, the CMOL typically performed better than the MOL for longer training time periods on the R and T-tests when the MOL was applied starting at the mainshock. These interpretations are generally in agreement of the results seen for the 2019 Ridgecrest sequence [Shcherbakov, 2021]. For a sequence with a large aftershock that appeared to produce its own aftershock sequence, the MOL fitted starting at the mainshock was found to have better performance than the CMOL. These results were limited as only one example was shown for each case.

In this study, the forecasting of known large aftershocks was also evaluated. The ETAS model did not present significant predictive power in terms of estimating large events, nor did the ETAS model show greater predictive power than the MOL or CMOL. This is not surprising as there was no obvious increase in seismicity prior to the forecasting time intervals. The probabilities for these known large aftershocks were all very small.

During shorter time intervals, it may be advisable to use both the MOL and ETAS models and consider the highest forecast probabilities if there is no prior information available for selecting the most suitable model for forecasting. When there is prior information available, such as a foreshock sequence or known background seismicity rates, the ETAS model parameter estimates produced by the MLE estimate better accounts for the early aftershock behaviour than the MOL. Regardless, the higher probability for large aftershocks should be considered for real-time forecasting as there was no consistent relationship between the probability forecasts between the ETAS and the MOL.

5.1 Summary of Work

In this work, the three goals provided in the Introduction were achieved by comparison of the forecasting test performance. As noted in the Introduction, for a model to be useful in the forecasting process, it must fit to the training data well, then demonstrate some forecasting

ability. Quantified scores from forecasting tests were analyzed to demonstrate each model's forecasting skill. In addition, testing of competing models and relative performance was done. The scope of this work was targeted towards the short-term forecasts for the week following immediately afterwards. The evolution of the model parameter fit, forecasting probability, and forecast test scores were produced. For the Amatrice, Kumamoto, and Darfield sequences, the probability of large aftershocks at known times were calculated.

In this study, four of the five case studies demonstrated that the ETAS model was the superior choice for forecasting by performing better on the individual tests. The forecast performance on the tests was consistent when increasing the magnitude cutoff M_0, indicating that the models and forecasting methods would be valid for catalogs with greater incompleteness. However, the probability of large aftershocks decreased when M_0 increased, suggesting that all of the models may underestimate the probability of large aftershocks. Some of the limitations of this study and comparison to previous forecasting results were addressed in Chapters 3 and 4. None of the models tested indicated forecasting ability for known aftershocks outside of the "short-term". This work also confirms that the EVD and BPD methods for the MOL and CMOL produce similar forecast results and thus, perform similarly on the forecasting tests.

Retrospective testing is not entirely representative of real-time testing. The goal of this study was not to present a specific framework to implement for real-time decision making. Instead, the aim was to present a method in which to evaluate a variety of models and to demonstrate how to interpret the statistical testing.

Based on these results, I would suggest that the first step during a forecast is to implement either the MOL or, the ETAS model and the MOL, depending on prior experience and information available. When in doubt, or if the ETAS model does not fit well and the prior conditions are not well established, the MOL should be prioritized and used for early forecasting. If the ETAS model appears to fit well, or the background rate in an area is well understood, then it can be used. However, both the ETAS and MOL can be used to forecast to estimate a range of different forecast probabilities for large aftershocks as the MOL forecast is relatively computa-

tionally inexpensive. The CMOL is not recommended in cases with a strong aftershock unless the mainshock occurs during the sequence or there is strong evidence for elevated seismicity levels following a large aftershock that results in a shift in the MOL parameters. Caution is recommended as the parameter estimation during the early secondary aftershocks may not be stable and the contributions from the first and second large shocks may be difficult to separate out. The MOL, CMOL, and the ETAS model can all be run at the same time for forecasting purposes. Assuming the computational capacity is available, there will be a span of probabilities produced by different models that can then be evaluated for risk.

5.2 Suggestions

The results of this work do suggest that the ETAS model in conjunction with the BPD is a closer representation of the sequences during forecasting. The implication is that the ETAS model is potentially more suitable for real-time forecasting as well. However, the ETAS model tends to take on the order of 10 times longer than the MOL to run, and even in the retrospective analyses, the ETAS model parameter estimates were assisted by knowledge of the background seismicity in advance. The number of sampling steps for the MCMC procedure cannot be reduced significantly either. In addition, for the Monte Cristo Range sequence, without fixing the K parameter, the model parameter estimates did not converge. Based on these two major reasons, the ETAS model should be well justified in its use for real-time forecasting. For example, it can be applied to sequences with complex fault rupture areas which are expected to potentially rupture, leading to bursts of seismic clustering. Alternatively, if the MOL clearly cannot capture the behaviour of the sequence, then the ETAS model can be applied. Additional work such as that done by [van der Elst et al., 2022] comparing the ETAS model to the standard Reasenberg-Jones method of forecasting should be done regularly where resources are available.

In anticipation of computational time usage, two suggestions to address ETAS forecasting concerns are provided. The first is to determine in more detail a range of standard parameters

for the ETAS model in areas of concern. As the ETAS model is stochastic in nature, the MLE method is more sensitive to the initiating model parameters that the solver is provided. More work can be done to develop these reference parameter ranges. Previously published parameter values are limited to large regions and may not be entirely descriptive of the regions that have recently experienced changes to the local stress field. The database of parameters and simulations can be updated regularly to be associated with the latest events. Standard expected ETAS parameters can also be used for the MLE method during a real-time forecast as the initiating values when solving the optimization problem. As the parameter values (either the standard ones, or the MLE solution) are used as prior values in the BPD, further study is well justified. For example, initiating parameter values may be related to the physical conditions of the region of interest.

Second, the behaviour of existing sequences can be analyzed in a similar fashion to this study to identify specific traits in the early aftershock sequence that may provide more context for prioritizing the ETAS model, or knowledge that the MOL will be sufficient, in describing the sequence and producing a more reliable forecast. Further work may include development of indices for clustering, smoothness, and other metrics to assist in the choice of aftershock model without requiring retrospective knowledge.

Based on the results in this work, it appears that the CMOL does not serve any additional purpose. As the CMOL can only be applied following a second large shock, it is less useful than the ETAS model and the MOL in forecasting during the early sequence. However, the CMOL can easily be included in the automated forecasting methods already in place. Following a second large event that is part of an ongoing sequence, the CMOL can be run parallel to the MOL. To reduce the complexity in τ selection, a suggestion regarding automatic use of the CMOL is provided. The CMOL can automatically be fitted to any instances of large aftershocks taking place at least one day from the initiating event, with magnitude $M > M_{main} - 1.5$ and when the number of observed events during $[\tau, \tau+0.5days]$ is larger than that during $[\tau-0.5, \tau]$. Any large discrepancies can be resolved by adding a layer of review consisting of experts who

can analyze the model results. At this point, the ETAS model may also be a good choice for better characterization of the sequence if it was not previously in use.

Further analysis of the CMOL is recommended. The CMOL performed reasonably well in the instance of the Kumamoto sequence, and better than the MOL did when applied to the mainshock. Comparisons of the CMOL to the MOL for foreshock-aftershock sequences may reveal patterns or conditions under which the CMOL may perform better with the additional contributions from the foreshocks. Additional analysis will also provide better constraints under when the CMOL should be automatically implemented.

An implicit assumption of this work is the expectation that the GR law sufficiently describes the past and forecasted magnitude distribution. The method used in this work assumes that the β value is stationary in time. Based on the split between the frequency-magnitude and rate models, the expectation would be that impacts on the forecast test performance would be negligible. Specifically for the MOL and the CMOL forecasts, the rate is determined independently of the magnitude of the events, assuming the M_c is selected appropriately. During the forecasting procedure, the magnitude of events is randomly drawn from the frequency-magnitude distribution as described by the β. However, the ETAS model requires simulation including sampling from the distribution and thus would result in a different rate depending on β. To address the the change in b-value as the sequence progresses, an adaptive β estimation method can be introduced.

The use of Bayesian methods in this work, while powerful and accounts for model parameter uncertainty, is also strongly affected by the choice of prior values for the model parameters. Model parameters which affect the rate such as μ, K for the ETAS model and K_0, K_1, and K_2 for the MOL and CMOL strongly influence the distribution during the MCMC sampling process, though [Shcherbakov et al., 2019] suggests that β, K, c, p, α should be stable when the prior changes, μ is the most impacted. Interpretation of results with fixed μ should be evaluated carefully.

Lastly, the Bayesian p-test can be implemented with an upper limit for "passing", as ex-

treme success should be considered a "pass with caution" as the number of events in the forecast is not scaled to the number of events in the observed period. Examples of limits could be $p \leq 0.99$ as an upper limit to passing and $p \geq 0.95$ as passing, but with caution.

5.3 Final Remarks

This work is also intended to encourage more work in terms of reviewing the statistics of the forecasting results when the opportunity to do retrospective work is available. The regular testing and analysis of model fits is common practice in other fields which implement the use of models to fit behaviour of complex data. In the case of earthquakes, the data quality is variable and may be difficult to access. In addition, each earthquake sequence is different even during retrospective analysis. Thus, unlike with some other data heavy fields, it may be necessary to evaluate the results for individual sequences instead of searching for a singular model to apply for multiple sequences. The statistical analyses will provide further direction for future forecasting developments. In particular, it may be possible to identify certain features of sequences associated with better forecasting performance using specific models. Some of the limitations and suitability for using these models and methods were discussed, and suggestions for future work provided.

The questions presented at the beginning of this thesis were partially addressed. I presented the first instance of compiled probability comparisons using Bayesian methods in forecasting that involves the use of statistical tests modified from CSEP and the additional Bayesian p-test for several sequences. These test results show that the ETAS model tends to forecast the behaviour of the sequences in a more similar manner to that of the true sequence in short forecasts. However, the results of the work do not clearly indicate which forecast is better in terms of forecasting large aftershocks. The method in which the aftershock magnitudes are selected is based on assumed knowledge of the frequency-magnitude distribution. By modifying the method in which the GR law is sampled, or forecasting the change in β, the forecast of large aftershocks may become more accurate.

More sequences should be reviewed with these statistical tests, particularly under the circumstances of low magnitude completeness or those of doublet form. The results can be extended to spatiotemporal versions of models in a straight-forward fashion.

Bibliography

[Abercrombie et al., 2006] Abercrombie, R. E., McGarr, A., Di Toro, G., and Kanamori, H. (2006). *Earthquakes: Radiated Energy and the Physics of Faulting*. American Geophysical Union, Washington, DC.

[Agnew, 2015] Agnew, D. C. (2015). Equalized Plot Scales for Exploring Seismicity Data. *Seismological Research Letters*, 86(5):1412–1423.

[Aki, 1965] Aki, K. (1965). 17. Maximum Likelihood Estimate of b in the Formula logN = a-bM and its Confidence Limits. *Bulletin of the Earthquake Research Institute, University of Tokyo*, 43(2):237–239.

[Aki, 1969] Aki, K. (1969). Analysis of the seismic coda of local earthquakes as scattered waves. *Journal of Geophysical Research*, 74(2):615–631.

[Allen et al., 2009] Allen, R. M., Gasparini, P., Kamigaichi, O., and Böse, M. (2009). The Status of Earthquake Early Warning around the World: An Introductory Overview. *Seismological Research Letters*, 80(5):682–693.

[Anzidei et al., 2009] Anzidei, M., Boschi, E., Cannelli, V., Devoti, R., Esposito, A., Galvani, A., Melini, D., Pietrantonio, G., Riguzzi, F., Sepe, V., and Serpelloni, E. (2009). Coseismic deformation of the destructive April 6, 2009 L'Aquila earthquake (central Italy) from GPS data. *Geophysical Research Letters*, 36(17).

[Atzori et al., 2009] Atzori, S., Hunstad, I., Chini, M., Salvi, S., Tolomei, C., Bignami, C., Stramondo, S., Trasatti, E., Antonioli, A., and Boschi, E. (2009). Finite fault inversion of DInSAR coseismic displacement of the 2009 L'Aquila earthquake (central Italy). *Geophysical Research Letters*, 36(15):15305.

[Båth, 1981] Båth, M. (1981). Earthquake magnitude - recent research and current trends. *Earth Science Reviews*, 17(4):315–398.

[Beauval et al., 2008] Beauval, C., Bard, P. Y., Hainzl, S., and Guéguen, P. (2008). Can Strong-Motion Observations be Used to Constrain Probabilistic Seismic-Hazard Estimates? *Bulletin of the Seismological Society of America*, 98(2):509–520.

[Beavan et al., 2012] Beavan, J., Motagh, M., Fielding, E. J., Donnelly, N., and Collett, D. (2012). Fault slip models of the 2010–2011 Canterbury, New Zealand, earthquakes from geodetic data and observations of postseismic ground deformation. *New Zealand Journal of Geology and Geophysics*, 55(3):207–221.

[Bender, 1983] Bender, B. (1983). MAXIMUM LIKELIHOOD ESTIMATION OF b VALUES FOR MAGNITUDE GROUPED DATA. *Bulletin of the Seismological Society of America*, 73(3):831–851.

[Bindi et al., 2005] Bindi, D., Spallarossa, D., Eva, C., and Cattaneo, M. (2005). Local and duration magnitudes in northwestern Italy, and seismic moment versus magnitude relationships. *Bulletin of the Seismological Society of America*, 95(2):592–604.

[Campbell, 1982] Campbell, K. W. (1982). BAYESIAN ANALYSIS OF EXTREME EARTHQUAKE OCCURRENCES. PART I. PROBABILISTIC HAZARD MODEL. *Bulletin of the Seismological Society of America*, 72(5):1689–1705.

[Chiarabba et al., 2009] Chiarabba, C., Amato, A., Anselmi, M., Baccheschi, P., Bianchi, I., Cattaneo, M., Cecere, G., Chiaraluce, L., Ciaccio, M. G., De Gori, P., De Luca, G., Di

Bona, M., Di Stefano, R., Faenza, L., Govoni, A., Improta, L., Lucente, F. P., Marchetti, A., Margheriti, L., Mele, F., Michelini, A., Monachesi, G., Moretti, M., Pastori, M., Piana Agostinetti, N., Piccinini, D., Roselli, P., Seccia, D., and Valoroso, L. (2009). The 2009 L'Aquila (central Italy) M W 6.3 earthquake: Main shock and aftershocks. *Geophysical Research Letters*, 36(18):L18308.

[Chiaraluce et al., 2011] Chiaraluce, L., Valoroso, L., Piccinini, D., Stefano, R. D., and Gori, P. D. (2011). The anatomy of the 2009 L'Aquila normal fault system (central Italy) imaged by high resolution foreshock and aftershock locations. *Journal of Geophysical Research: Solid Earth*, 116(B12):12311.

[Chung et al., 2020] Chung, A. I., Meier, M. A., Andrews, J., Böse, M., Crowell, B. W., McGuire, J. J., and Smith, D. E. (2020). ShakeAlert Earthquake Early Warning System Performance during the 2019 Ridgecrest Earthquake Sequence. *Bulletin of the Seismological Society of America*, 110(4):1904–1923.

[Daley and Vere-Jones, 2003] Daley, D. J. and Vere-Jones, D. (2003). *An Introduction to the Theory of Point Processes*. Springer-Verlag.

[Delavaud et al., 2012] Delavaud, E., Cotton, F., Akkar, S., Scherbaum, F., Danciu, L., Beauval, C., Drouet, S., Douglas, J., Basili, R., Sandikkaya, M. A., Segou, M., Faccioli, E., and Theodoulidis, N. (2012). Toward a ground-motion logic tree for probabilistic seismic hazard assessment in Europe. *Journal of Seismology*, 16(3):451–473.

[di Bona, 2016] di Bona, M. (2016). A local magnitude scale for Crustal Earthquakes in Italy. *Bulletin of the Seismological Society of America*, 106(1):242–258.

[Dieterich, 1994] Dieterich, J. (1994). A constitutive law for rate of earthquake production and its application to earthquake clustering. *Journal of Geophysical Research: Solid Earth*, 99(B2):2601–2618.

[Earthquake Research Committee, 2016] Earthquake Research Committee (2016). ERC Aug 19, 2016 Report. Technical report.

[Ebrahimian and Jalayer, 2017] Ebrahimian, H. and Jalayer, F. (2017). Robust seismicity forecasting based on Bayesian parameter estimation for epidemiological spatio-temporal aftershock clustering models. *Scientific Reports*, 7(1):1–15.

[Ebrahimian et al., 2014] Ebrahimian, H., Jalayer, F., Asprone, D., Lombardi, A. M., Marzocchi, W., Prota, A., and Manfredi, G. (2014). Adaptive daily forecasting of seismic aftershock hazard. *Bulletin of the Seismological Society of America*, 104(1):145–161.

[Elter et al., 2003] Elter, P., Grasso, M., Parotto, M., and Vezzani, L. (2003). Structural setting of the Apennine-Maghrebian thrust belt. *Episodes Journal of International Geoscience*, 26(3):205–211.

[Evison and Rhoades, 2004] Evison, F. F. and Rhoades, D. A. (2004). Demarcation and Scaling of Long-term Seismogenesis. *Pure and Applied Geophysics*, 161:21–45.

[Field et al., 2009] Field, E. H., Dawson, T. E., Felzer, K. R., Frankel, A. D., Gupta, V., Jordan, T. H., Parsons, T., Petersen, M. D., Stein, R. S., Weldon, R. J., and Wills, C. J. (2009). Uniform California Earthquake Rupture Forecast, Version 2 (UCERF 2). *Bulletin of the Seismological Society of America*, 99(4):2053–2107.

[Frohlich and Davis, 1993] Frohlich, C. and Davis, S. D. (1993). Teleseismic b values; Or, much ado about 1.0. *Journal of Geophysical Research: Solid Earth*, 98(B1):631–644.

[Fry et al., 2011] Fry, B., Benites, R., Reyners, M., Holden, C., Kaiser, A., Bannister, S., Gerstenberger, M., Williams, C., Ristau, J., and Beavan, J. (2011). Strong shaking in recent New Zealand earthquakes. *Eos, Transactions American Geophysical Union*, 92(41):349–351.

[Geller, 1997] Geller, R. J. (1997). Special section - Assessment of schemes for earthquake prediction Earthquake prediction: A critical review. *Geophysical Journal International*, 131(3):425–450.

[Geller et al., 1997] Geller, R. J., Jackson, D. D., Kagan, Y. Y., and Mulargia, F. (1997). Earthquakes cannot be predicted. *Science*, 275(5306):1616–1617.

[Gerstenberger and Rhoades, 2010] Gerstenberger, M. C. and Rhoades, D. A. (2010). New Zealand Earthquake Forecast Testing Centre. *Seismogenesis and Earthquake Forecasting: The Frank Evison Volume II*, pages 23–38.

[Gerstenberger et al., 2005] Gerstenberger, M. C., Wiemer, S., Jones, L. M., and Reasenberg, P. A. (2005). Real-time forecasts of tomorrow's earthquakes in California. *Nature*, 435(7040):328–331.

[Gutenberg and Richter, 1944] Gutenberg, B. and Richter, C. F. (1944). FREQUENCY OF EARTHQUAKES IN CALIFORNIA*. *Bulletin of the Seismological Society of America*, 34:185–188.

[Gutenberg and Richter, 1955] Gutenberg, B. and Richter, C. F. (1955). Magnitude and Energy of Earthquakes. *Nature*, 176.

[Guttorp and Hopkins, 1986] Guttorp, P. and Hopkins, D. (1986). ON ESTIMATING VARYING b VALUES. Technical Report 3.

[Hainzl, 2016a] Hainzl, S. (2016a). Apparent triggering function of aftershocks resulting from rate-dependent incompleteness of earthquake catalogs. *Journal of Geophysical Research: Solid Earth*, 121(9):6499–6509.

[Hainzl, 2016b] Hainzl, S. (2016b). Rate-dependent incompleteness of earthquake catalogs. *Seismological Research Letters*, 87(2A):337–344.

[Hanks and Kanamori, 1979] Hanks, T. C. and Kanamori, H. (1979). A moment magnitude scale. *Journal of Geophysical Research B: Solid Earth*, 84(B5):2348–2350.

[Hardebeck et al., 2019] Hardebeck, J. L., Llenos, A. L., Michael, A. J., Page, M. T., and van der Elst, N. (2019). Updated California Aftershock Parameters. *Seismological Research Letters*, 90(1):262–270.

[Harte and Vere-Jones, 2005] Harte, D. and Vere-Jones, D. (2005). The Entropy Score and its Uses in Earthquake Forecasting. *Pure and Applied Geophysics*, 162:1229–1253.

[Helmstetter and Sornette, 2003] Helmstetter, A. and Sornette, D. (2003). Predictability in the ETAS Model of Interacting Triggered Seismicity. Technical report.

[Jordan, 2006] Jordan, T. H. (2006). Earthquake predictability, Brick by Brick. *Seismological Research Letters*, 77(1):3–6.

[Kagan, 1991] Kagan, Y. Y. (1991). Likelihood analysis of earthquake catalogues. *Geophys. J. Int*, 106:135–148.

[Kagan, 2002] Kagan, Y. Y. (2002). Aftershock Zone Scaling. *Bulletin of the Seismological Society of America*, 92(2):641–655.

[Kagan, 2004] Kagan, Y. Y. (2004). Short-term properties of earthquake catalogs and models of earthquake source. *Bulletin of the Seismological Society of America*, 94(4):1207–1228.

[Kagan and Jackson, 1995] Kagan, Y. Y. and Jackson, D. D. (1995). New seismic gap hypothesis: five years after. *Journal of Geophysical Research*, 100(B3):3943–3959.

[Kanamori, 1977] Kanamori, H. (1977). The energy release in great earthquakes. *Journal of Geophysical Research*, 82(20):2981–2987.

[Kanamori, 1983] Kanamori, H. (1983). Magnitude scale and quantification of earthquakes. *Tectonophysics*, 93(3-4):185–199.

[Kanamori and Anderson, 1975] Kanamori, H. and Anderson, D. L. (1975). Theoretical basis of some empirical relations in seismology. *Bulletin of the Seismological Society of America*, 65(5):1073–1095.

[Kawamoto et al., 2016] Kawamoto, S., Hiyama, Y., Ohta, Y., and Nishimura, T. (2016). First result from the GEONET real-time analysis system (REGARD): the case of the 2016 Kumamoto earthquakes. *Earth, Planets and Space*, 68(1):1–12.

[King et al., 1994] King, G. C. P., Stein, R. S., and Lin, J. (1994). Static stress changes and the triggering of earthquakes. *Bulletin of the Seismological Society of America*, 84(3):935–953.

[Kossobokov, 2013] Kossobokov, V. G. (2013). Earthquake prediction: 20 years of global experiment. *Natural Hazards*, 69(2):1155–1177.

[Lippiello et al., 2007] Lippiello, E., Bottiglieri, M., Godano, C., and De Arcangelis, L. (2007). Dynamical scaling and generalized Omori law.

[Lolli et al., 2011] Lolli, B., Gasperini, P., and Boschi, E. (2011). Time variations of aftershock decay parameters of the 2009 April 6 L'Aquila (central Italy) earthquake: Evidence of the emergence of a negative exponential regime superimposed to the power law. *Geophysical Journal International*, 185(2):764–774.

[Lombardi, 2015] Lombardi, A. M. (2015). Estimation of the parameters of ETAS models by Simulated Annealing. *Scientific Reports 2015 5:1*, 5(1):1–11.

[Lombardi, 2016] Lombardi, A. M. (2016). Some reasoning on the improvement of the ETAS modeling at the occurrence of the 2016 central Italy seismic sequence. *Annals of Geophysics*, 59(FASTTRACK5).

[Lombardi and Marzocchi, 2010a] Lombardi, A. M. and Marzocchi, W. (2010a). THE ETAS MODEL FOR DAILY FORECASTING OF ITALIAN SEISMICITY IN CSEP EXPERIMENT. Technical report.

[Lombardi and Marzocchi, 2010b] Lombardi, A. M. and Marzocchi, W. (2010b). The ETAS model for daily forecasting of italian seismicity in the CSEP experiment. *Annals of Geophysics*, 53(3):155–164.

[Mancini et al., 2019] Mancini, S., Segou, M., Werner, M. J., and Cattania, C. (2019). Improving Physics-Based Aftershock Forecasts During the 2016–2017 Central Italy Earthquake Cascade. *Journal of Geophysical Research: Solid Earth*, 124(8):8626–8643.

[Márquez-Ramírez et al., 2015] Márquez-Ramírez, V. H., Nava, F. A., and Zúñiga, F. R. (2015). Correcting the Gutenberg–Richter b-value for effects of rounding and noise. *Earthquake Science*, 28:129–134.

[Marzocchi and Lombardi, 2009] Marzocchi, W. and Lombardi, A. M. (2009). Real-time forecasting following a damaging earthquake. *Geophysical Research Letters*, 36(21):L21302.

[Mignan et al., 2011] Mignan, A., Werner, M. J., Wiemer, S., Chen, C. C., and Wu, Y. M. (2011). Bayesian Estimation of the Spatially Varying Completeness Magnitude of Earthquake CatalogsBayesian Estimation of the Spatially Varying Completeness Magnitude of Earthquake Catalogs. *Bulletin of the Seismological Society of America*, 101(3):1371–1385.

[Milliner et al., 2020] Milliner, C., Bürgmann, R., Inbal, A., Wang, T., and Liang, C. (2020). Resolving the Kinematics and Moment Release of Early Afterslip Within the First Hours Following the 2016 M w 7.1 Kumamoto Earthquake: Implications for the Shallow Slip Deficit and Frictional Behavior of Aseismic Creep. *Journal of Geophysical Research: Solid Earth*, 125(9).

[Morton et al., 2020] Morton, E. A., Ruhl, C. J., Bormann, J. M., Hatch-Ibarra, R., Ichinose, G., and Smith, K. D. (2020). The 2020 Mww 6.5 Monte Cristo Range , NV Earthquake and Aftershock Sequence.

[Mueller, 2019] Mueller, C. S. (2019). (DATA) Earthquake catalogs for the USGS national seismic hazard maps. *Seismological Research Letters*, 90(1):251–261.

[N/A, 2020] N/A (2020). Personal Communication. Correspondence during American Geophysical Union Fall Meeting, 2020.

[Nanjo et al., 2016] Nanjo, K. Z., Izutsu, J., Orihara, Y., Furuse, N., Togo, S., Nitta, H., Okada, T., Tanaka, R., Kamogawa, M., and Nagao, T. (2016). Seismicity prior to the 2016 Kumamoto earthquakes. *Earth, Planets and Space*, 68(1):1–10.

[Nanjo et al., 2012] Nanjo, K. Z., Tsuruoka, H., Yokoi, S., Ogata, Y., Falcone, G., Hirata, N., Ishigaki, Y., Jordan, T. H., Kasahara, K., Obara, K., Schorlemmer, D., Shiomi, K., and Zhuang, J. (2012). Predictability study on the aftershock sequence following the 2011 Tohoku-Oki, Japan, earthquake: first results. *Geophysical Journal International*, 191(2):653–658.

[Nanjo and Yoshida, 2017] Nanjo, K. Z. and Yoshida, A. (2017). Anomalous decrease in relatively large shocks and increase in the p and b values preceding the April 16, 2016, M7.3 earthquake in Kumamoto, Japan. *Earth, Planets and Space*, 69(1):1–8.

[Ogata, 1978] Ogata, Y. (1978). The asymptotic behaviour of maximum likelihood estimators for stationary point processes. *Annals of the Institute of Statistical Mathematics*, 30(2):243–261.

[Ogata, 1981] Ogata, Y. (1981). On Lewis' Simulation Method for Point Processes. *IEEE Transactions on Information Theory*, 27(1):23–31.

[Ogata, 1983] Ogata, Y. (1983). Estimation of the Parameters in the Modified Omori Formula for Aftershock Frequencies. *Journal of Physics of the Earth*, 31:115–124.

[Ogata, 1988] Ogata, Y. (1988). Statistical Models for Earthquake Occurrences and Residual Analysis for Point Processes. *Journal of the American Statistical Association*, 83(401):9–27.

[Ogata, 1998] Ogata, Y. (1998). Space-time point-process models for earthquake occurrences. *Annals of the Institute of Statistical Mathematics*, 50(2):379–402.

[Ogata, 1999] Ogata, Y. (1999). Seismicity Analysis through Point-process Modeling: A Review. *Pure and Applied Geophysics*, 155:471–507.

[Ogata, 2017] Ogata, Y. (2017). Statistics of Earthquake Activity: Models and Methods for Earthquake Predictability Studies. *Annual Review of Earth and Planetary Sciences*, 45:497–527.

[Ogata and Katsura, 1986] Ogata, Y. and Katsura, K. (1986). Point-process models with linearly parametrized intensity for application to earthquake data. *Journal of Applied Probability*, 23(A):291–310.

[Ogata and Zhuang, 2006] Ogata, Y. and Zhuang, J. (2006). Space-time ETAS models and an improved extension. *Tectonophysics*, 413(1-2):13–23.

[Omi et al., 2019] Omi, T., Aihara, K., Ogata, Y., Shiomi, K., Sawazaki, K., and Enescu, B. (2019). Implementation of a real-time system for automatic aftershock forecasting in Japan. *Seismological Research Letters*, 90(1):242–250.

[Omi et al., 2016] Omi, T., Ogata, Y., Shiomi, K., Enescu, B., Sawazaki, K., and Aihara, K. (2016). Automatic aftershock forecasting: A test using real-time seismicity data in Japan. *Bulletin of the Seismological Society of America*, 106(6):2450–2458.

[Omori, 1894] Omori, F. (1894). On the aftershocks of earthquakes. *Journal of the College of Science, Imperial University of Tokyo*, 7:111–200.

[Page et al., 2016] Page, M. T., van Der Elst, N., Hardebeck, J., Felzer, K., and Michael, A. J. (2016). Three ingredients for improved global aftershock forecasts: Tectonic region, time-dependent catalog incompleteness, and intersequence variability. *Bulletin of the Seismological Society of America*, 106(5):2290–2301.

[Papadopoulos et al., 2010] Papadopoulos, G. A., Charalampakis, M., Fokaefs, A., and Minadakis, G. (2010). Strong foreshock signal preceding the L'Aquila (Italy) earthquake (Mw 6.3) of 6 April 2009. *Natural Hazards and Earth System Science*, 10(1):19–24.

[Peng et al., 2006] Peng, Z., Vidale, J. E., and Houston, H. (2006). Anomalous early aftershock decay rate of the 2004 Mw6.0 Parkfield, California, earthquake. *Geophysical Research Letters*, 33(17):L17307.

[Petersen et al., 2020] Petersen, M. D., Shumway, A. M., Powers, P. M., Mueller, C. S., Moschetti, M. P., Frankel, A. D., Rezaeian, S., McNamara, D. E., Luco, N., Boyd, O. S., Rukstales, K. S., Jaiswal, K. S., Thompson, E. M., Hoover, S. M., Clayton, B. S., Field, E. H., and Zeng, Y. (2020). The 2018 update of the US National Seismic Hazard Model: Overview of model and implications. *Earthquake Spectra*, 36(1):5–41.

[Quigley et al., 2012] Quigley, M., Dissen, R. V., Litchfield, N., Villamor, P., Duffy, B., Barrell, D., Furlong, K., Stahl, T., Bilderback, E., and Noble, D. (2012). Surface rupture during the 2010 Mw 7.1 Darfield (Canterbury) earthquake: Implications for fault rupture dynamics and seismic-hazard analysis. *Geology*, 40(1):55–58.

[Quigley et al., 2010] Quigley, M., Villamor, P., Furlong, K., Beavan, J., Van Dissen, R., Litchfield, N., Stahl, T., Duffy, B., Bilderback, E., Noble, D., Barrell, D., Jongens, R., and Cox, S. (2010). Previously Unknown Fault Shakes New Zealand's South Island. *Eos, Transactions American Geophysical Union*, 91(49):469–470.

[Reasenberg and Jones, 1989] Reasenberg, P. A. and Jones, L. M. (1989). Earthquake hazard after a mainshock in California. *Science*, 243(4895):1173–1176.

[Renard et al., 2013] Renard, B., Sun, X., and Lang, M. (2013). Bayesian Methods for Non-stationary Extreme Value Analysis. In *Extremes in a Changing Climate*, pages 39–95. Springer, Dordrecht.

[Rhoades et al., 2017] Rhoades, D. A., Christophersen, A., and Gerstenberger, M. C. (2017). Multiplicative earthquake likelihood models incorporating strain rates. *Geophysical Journal International*, 208(3):1764–1774.

[Rhoades et al., 2018] Rhoades, D. A., Christophersen, A., Gerstenberger, M. C., Liukis, M., Silva, F., Marzocchi, W., Werner, M. J., and Jordan, T. H. (2018). Highlights from the first ten years of the New Zealand earthquake forecast testing center. *Seismological Research Letters*, 89(4):1229–1237.

[Rhoades and Evison, 2004] Rhoades, D. A. and Evison, F. F. (2004). Long-range Earthquake Forecasting with Every Earthquake a Precursor According to Scale. *pure and applied geophysics*, 161(1):47–72.

[Rhoades et al., 2011] Rhoades, D. A., Schorlemmer, D., Gerstenberger, M. C., Christophersen, A., Zechar, J. D., and Imoto, M. (2011). Efficient testing of earthquake forecasting models. *Acta Geophysica*, 59(4):728–747.

[Richter, 1935] Richter, C. F. (1935). An instrumental earthquake magnitude scale. *Bulletin of the Seismological Society of America*, 25(1):1–32.

[Rogers et al., 1991] Rogers, A. M., Harmsen, S. C., Corbett, E. J., Priestley, K., and DePolo, D. (1991). The seismicity of Nevada and some adjacent parts of the Great Basin. In *Neotectonics of North America*, volume Decade Map, pages 153–184. Geological Society of America.

[Rydelek and Sacks, 1989] Rydelek, P. A. and Sacks, I. S. (1989). Testing the completeness of earthquake catalogues and the hypothesis of self-similarity. *Nature*, 337(6204):251–253.

[Scholz, 1968] Scholz, C. H. (1968). The frequency-magnitude relation of microfracturing in rock and its relation to earthquakes. *Bulletin of the Seismological Society of America*, 58(1):399–415.

[Scholz, 2002] Scholz, C. H. (2002). *The Mechanics of Earthquakes and Faulting*. Cambridge University Press, Cambridge, 2 edition.

[Schorlemmer et al., 2007] Schorlemmer, D., Gerstenberger, M. C., Wiemer, S., Jackson, D. D., and Rhoades, D. A. (2007). Earthquake likelihood model testing. *Seismological Research Letters*, 78(1):17–29.

[Schorlemmer et al., 2010] Schorlemmer, D., Mele, F., and Marzocchi, W. (2010). A completeness analysis of the National Seismic Network of Italy. *Journal of Geophysical Research: Solid Earth*, 115(B4308).

[Schorlemmer et al., 2018] Schorlemmer, D., Werner, M. J., Marzocchi, W., Jordan, T. H., Ogata, Y., Jackson, D. D., Mak, S., Rhoades, D. A., Gerstenberger, M. C., Hirata, N., Liukis, M., Maechling, P. J., Strader, A., Taroni, M., Wiemer, S., Zechar, J. D., and Zhuang, J. (2018). The collaboratory for the study of earthquake predictability: Achievements and priorities. *Seismological Research Letters*, 89(4):1305–1313.

[Serpelloni et al., 2005] Serpelloni, E., Anzidei, M., Baldi, P., Casula, G., and Galvani, A. (2005). Crustal velocity and strain-rate fields in Italy and surrounding regions: new results from the analysis of permanent and non-permanent GPS networks. *Geophysical Journal International*, 161(3):861–880.

[Shcherbakov, 2014] Shcherbakov, R. (2014). Bayesian confidence intervals for the magnitude of the largest aftershock. *Geophysical Research Letters*, 41(18):6380–6388.

[Shcherbakov, 2021] Shcherbakov, R. (2021). Statistics and Forecasting of Aftershocks During the 2019 Ridgecrest, California, Earthquake Sequence. *Journal of Geophysical Research: Solid Earth*, 126(2).

[Shcherbakov, 2022] Shcherbakov, R. (2022). Personal Communication. Notes on temporal ETAS model log-likelihood function with normalization by Harte 2010.

[Shcherbakov et al., 2012] Shcherbakov, R., Nguyen, M., and Quigley, M. (2012). Statistical analysis of the 2010 M W 7.1 Darfield Earthquake aftershock sequence. *New Zealand Journal of Geology and Geophysics*, 55(3):305–311.

[Shcherbakov et al., 2004] Shcherbakov, R., Turcotte, D. L., and Rundle, J. B. (2004). A generalized Omori's law for earthquake aftershock decay. *Geophysical Research Letters*, 31(11):n/a–n/a.

[Shcherbakov et al., 2005a] Shcherbakov, R., Turcotte, D. L., and Rundle, J. B. (2005a). Aftershock Statistics. *pure and applied geophysics 2005 162:6*, 162(6):1051–1076.

[Shcherbakov et al., 2015] Shcherbakov, R., Turcotte, D. L., and Rundle, J. B. (2015). Complexity and Earthquakes. In *Treatise on Geophysics: Second Edition*, volume 4, pages 627–653. Elsevier B.V.

[Shcherbakov et al., 2005b] Shcherbakov, R., Yakovlev, G., Turcotte, D. L., and Rundle, J. B. (2005b). Model for the Distribution of Aftershock Interoccurrence Times. *Physical Review Letters*, 95(21):218501.

[Shcherbakov et al., 2018] Shcherbakov, R., Zhuang, J., and Ogata, Y. (2018). Constraining the magnitude of the largest event in a foreshock-main shock-aftershock sequence. *Geophysical Journal International Geophys. J. Int*, 212:1–13.

[Shcherbakov et al., 2019] Shcherbakov, R., Zhuang, J., Zöller, G., and Ogata, Y. (2019). Forecasting the magnitude of the largest expected earthquake. *Nature Communications*, 10(4051).

[Shebalin et al., 2012] Shebalin, P., Narteau, C., and Holschneider, M. (2012). From Alarm-Based to Rate-Based Earthquake Forecast Models. *Bulletin of the Seismological Society of America*, 102(1):64–72.

[Shebalin et al., 2011] Shebalin, P., Narteau, C., Holschneider, M., and Schorlemmer, D. (2011). Short-term earthquake forecasting using early aftershock statistics. *Bulletin of the Seismological Society of America*, 101(1):297–312.

[Shi and Bolt, 1982] Shi, Y. and Bolt, B. A. (1982). THE STANDARD ERROR OF THE MAGNITUDE-FREQUENCY b VALUE. *Bulletin of the Seismological Society of America*, 72(5):1677–1687.

[Strader et al., 2017] Strader, A., Schneider, M., and Schorlemmer, D. (2017). Prospective and retrospective evaluation of five-year earthquake forecast models for California. *Geophysical Journal International*, 211(1):239–251.

[Sykes et al., 1999] Sykes, L. R., Shaw, B. E., and Scholz, C. H. (1999). Rethinking earthquake prediction. *Pure and Applied Geophysics*, 155(2-4):207–232.

[Tamaribuchi, 2018] Tamaribuchi, K. (2018). Evaluation of automatic hypocenter determination in the JMA unified catalog. *Earth, Planets and Space*, 70(141):1–10.

[Taroni et al., 2018] Taroni, M., Marzocchi, W., Schorlemmer, D., Werner, M. J., Wiemer, S., Zechar, J. D., Heiniger, L., and Euchner, F. (2018). Prospective CSEP Evaluation of 1-Day, 3-Month, and 5-Yr Earthquake Forecasts for Italy. *Seismological Research Letters*, 89(4):1251–1261.

[Tinti et al., 1987] Tinti, S., Rimondi, R., and Mulargia, F. (1987). On estimating frequency-magnitude relations from heterogeneous catalogs. *Pure and Applied Geophysics PAGEOPH*, 125(1):1–18.

[Utsu, 1961] Utsu, T. (1961). A statistical study on the occurrence of aftershocks. *Geophys.Mag.*, 30:521–605.

[Utsu, 1965] Utsu, T. (1965). A method for determining the value of "b" in a formula log n = a-bM showing the magnitude-frequency relation for earthquakes. *Geophys. Bull. Hokkaido Univ.*, 13:99–103.

[Utsu, 1970] Utsu, T. (1970). Aftershocks and Earthquake Statistics (II) - Further Investigation of Aftershocks and Other Earthquake Sequences Based on a New Classification of Earthquake Sequences. *Journal of the Faculty of Science, Hokkaido University, Ser. VII (Geophysics)*, III(4):197–266.

[Utsu, 1971] Utsu, T. (1971). Aftershocks and Earthquake Statistics (II) Further Investigation of Aftershocks and Other Earthquake Sequences Based on a New Classification of Earthquake Sequences. *Journal of the Faculty of Science, Hokkaido University. Series 7, Geophysics*, 3(4):197–266.

[Utsu et al., 1995] Utsu, T., Ogata, Y., S, R., and Matsu'ura (1995). The Centenary of the Omori Formula for a Decay Law of Aftershock Activity. *Journal of Physics of the Earth*, 43(1):1–33.

[Utsu and Seki, 1955] Utsu, T. and Seki, A. (1955). A Relation between the Area of Aftershock Region and the Energy of Main-shock. *Zisin (2)*, 7(4):233–240.

[van der Elst et al., 2022] van der Elst, N. J., Hardebeck, J. L., Michael, A. J., McBride, S. K., and Vanacore, E. (2022). Prospective and Retrospective Evaluation of the U.S. Geological Survey Public Aftershock Forecast for the 2019–2021 Southwest Puerto Rico Earthquake and Aftershocks. *Seismological Research Letters*, 93(2A):620–640.

[Vere-Jones, 1975] Vere-Jones, D. (1975). Stochastic Models for Earthquake Sequences. *Geophysical Journal of the Royal Astronomical Society*, 42(2):811–826.

[Vere-Jones, 2010] Vere-Jones, D. (2010). Foundations of statistical seismology. *Pure and Applied Geophysics*, 167(6):645–653.

[Vere-Jones and Ozaki, 1982] Vere-Jones, D. and Ozaki, T. (1982). SOME EXAMPLES OF STATISTICAL ESTIMATION APPLIED TO EARTHQUAKE DATA I. CYCLIC POISSON AND SELF-EXCITING MODELS. *Ann. Inst. Statist. Math*, 34:189–207.

[Vigil et al., 2000] Vigil, J. F., Pike, R. J., and Howell, D. G. (2000). A Tapestry of Time and Terrain Pamphlet to accompany Geologic Investigations Series I-2720. Technical report.

[Walters et al., 2009] Walters, R. J., Elliott, J. R., D'Agostino, N., England, P. C., Hunstad, I., Jackson, J. A., Parsons, B., Phillips, R. J., and Roberts, G. (2009). The 2009 L'Aquila earthquake (central Italy): A source mechanism and implications for seismic hazard. *Geophysical Research Letters*, 36(17):17312.

[Wells and Coppersmith, 1994] Wells, D. L. and Coppersmith, K. J. (1994). New Empirical Relationships among Magnitude, Rupture Length, Rupture Width, Rupture Area, and Surface Displacement. *Bulletin of the Seismological Society of America*, 84(4):974–1002.

[Woessner et al., 2015] Woessner, J., Laurentiu, D., Giardini, D., Crowley, H., Cotton, F., Grünthal, G., Valensise, G., Arvidsson, R., Basili, R., Demircioglu, M. B., Hiemer, S., Meletti, C., Musson, R. W., Rovida, A. N., Sesetyan, K., Stucchi, M., and The SHARE Consortium (2015). The 2013 European Seismic Hazard Model: key components and results. *Bulletin of Earthquake Engineering*, 13:3553–3596.

[Woessner and Wiemer, 2005] Woessner, J. and Wiemer, S. (2005). Assessing the Quality of Earthquake Catalogues: Estimating the Magnitude of Completeness and Its Uncertainty. *Bulletin of the Seismological Society of America*, 95(2):684–698.

[Wyss, 1973] Wyss, M. (1973). Towards a Physical Understanding of the Earthquake Frequency Distribution. *Geophysical Journal of the Royal Astronomical Society*, 31(4):341–359.

[Zechar et al., 2010] Zechar, J. D., Gerstenberger, M. C., and Rhoades, D. A. (2010). Likelihood-based tests for evaluating space-rate-magnitude earthquake forecasts. *Bulletin of the Seismological Society of America*, 100(3):1184–1195.

[Zechar and Jordan, 2008] Zechar, J. D. and Jordan, T. H. (2008). Testing alarm-based earthquake predictions. *Geophysical Journal International*, 172(2):715–724.

[Zechar et al., 2009] Zechar, J. D., Schorlemmer, D., Liukis, M., Yu, J., Euchner, F., Maechling, P. J., and Jordan, T. H. (2009). The Collaboratory for the Study of Earthquake Predictability perspective on computational earthquake science. *Concurrency and Computation: Practice and Experience*, 22(12):1836–1847.

[Zeiler, 2021] Zeiler, C. P. (2021). Personal Communication.

[Zhang et al., 2018] Zhang, L., Werner, M. J., and Goda, K. (2018). Spatiotemporal Seismic Hazard and Risk Assessment of Aftershocks of M 9 Megathrust EarthquakesSpatiotemporal Seismic Hazard and Risk Assessment of Aftershocks of M 9 Megathrust Earthquakes. *Bulletin of the Seismological Society of America*, 108(6):3313–3335.

[Zheng et al., 2020] Zheng, A., Chen, X., and Xu, W. (2020). Present-Day Deformation Mechanism of the Northeastern Mina Deflection Revealed by the 2020 M w 6.5 Monte Cristo Range Earthquake. *Geophysical Research Letters*, 47(22).

[Zhuang et al., 2012] Zhuang, J., Harte, D., Werner, M. J., Hainzl, S., and Zhou, S. (2012). Basic models of seismicity: Temporal models.

[Zhuang and Ogata, 2006] Zhuang, J. and Ogata, Y. (2006). Properties of the probability distribution associated with the largest event in an earthquake cluster and their implications to foreshocks. *Physical Review E*, 73:046134.

[Zhuang et al., 2004] Zhuang, J., Ogata, Y., and Vere-Jones, D. (2004). Analyzing earthquake clustering features by using stochastic reconstruction. *Journal of Geophysical Research: Solid Earth*, 109(B5):5301.

[Zhuang et al., 2011] Zhuang, J., Werner, M. J., Hainzl, S., Harte, D., Zhou, S., Zhuang, J., Werner, M. J., Hainzl, S., Harte, D., and Zhou, S. (2011). Theme V-Models and Techniques for Analyzing Seismicity Basic models of seismicity: Spatiotemporal models.

Appendix A

Functions and MATLAB Settings

A.1 Log-Likelihood Functions

To solve the aftershock model parameters, the negative log-likehood functions of the aftershock models are minimized, thus maximizing the log-likelihood. For a typical aftershock decay that can be described by the MOL, the log-likelihood of the MOL was proposed as a solution by Ogata (1983), Ogata1978 and is shown as

$$\ln L(\theta) = \sum_{i=1}^{N} \ln \lambda_{\omega}(t_i) - \int_{T_s}^{T_e} \lambda(t)dt \tag{A.1}$$

[Ogata and Zhuang, 2006, Zhuang and Ogata, 2006] estimated over the training time interval $[T_s, T_e]$ for N events during the time interval. This solution is also valid for the CMOL. The likelihood function for the ETAS model is similar and dependency on time is included. Then generically, the rate function can be replaced by $\lambda_{\omega}(t|H_t)$ for a stationary process [Ogata and Zhuang, 2006]. If the ETAS model is a non-homogeneous Poisson process, the likelihood function for time-dependent $\lambda_{\omega}(t|H_t)$ and event magnitudes described by $F_{\theta}(m)$ is

$$L(M_n|\theta, \omega) = e^{-\Lambda_{\omega}(T_s,T_e)} \prod_{j=1}^{n} \lambda_{\omega}(t_{k+j}) \prod_{j=1}^{n} f_{\theta}(m_{k+j}) \tag{A.2}$$

[Daley and Vere-Jones, 2003]. $f_\theta(m) = \frac{dF_\theta(m)}{dm}$ is the probability density function, $\Lambda_\omega(T_s, T_e)$ is the productivity function during the training time interval $[T_s, T_e]$, and k denotes the events occuring prior to T_s. The magnitude and time of n events is given by $M_n = \{(t_{k+j}, m_{k+j}) for j = 1, \dots n\}$ during the training time interval. The productivity function can be described explicitly with

$$\Lambda_\omega(T_s, T_e) = \mu(T_e - T_s) + \frac{Kc}{p-1} \sum_{i=1}^{k} e^{\alpha(m_i - m_0)} \left[\left(\frac{T_s - t_i}{c} + 1 \right)^{1-p} - \left(\frac{T_e - t_i}{c} + 1 \right)^{1-p} \right] \tag{A.3}$$

$$+ \frac{Kc}{p-1} \sum_{i=k+1 : T_s \le t_i \le T_e}^{N_{T_e}} e^{\alpha(m_i - m_0)} \left[1 - \left(\frac{T_e - t_i}{c} + 1 \right)^{1-p} \right] \tag{A.4}$$

when $p \neq 1$. For $p = 1$, the productivity function is

$$\Lambda_\omega(T_s, T_e) = \mu(T_e - T_s) + Kc \sum_{i=1}^{k} \log \left(\frac{\frac{T_e - t_i}{c} + 1}{\frac{T_s - t_i}{c} + 1} \right) \tag{A.5}$$

$$+ Kc \sum_{i=k+1 : T_s \le t_i \le T_e}^{N_{T_e}} e^{\alpha(m_i - m_0)} \log \left(\frac{T_e - t_i}{c} + 1 \right) \tag{A.6}$$

[Shcherbakov, 2022] which can then be substituted into the log-likelihood function resulting in

$$\ln[L(M_n | \theta, \omega)] = -\Lambda_\omega(T_s, T_e) + + \sum_{j=1}^{n} \ln[\lambda_\omega(t_{k+j})] + \sum_{j=1}^{n} \ln[f_\theta(m_{k+j})] \tag{A.7}$$

$$= -\Lambda_\omega(T_s, T_e) + \sum_{j=1}^{n} \ln \left[\mu + K \sum_{i=t_i < t_{k+j}}^{N_{t_{k+j}}} \frac{e^{\alpha(m_i - m_0)}}{\left(\frac{t_{k+j} - t_i}{c} + 1 \right)^p} \right] \tag{A.8}$$

$$+ n \ln \beta - \beta \sum_{j=1} n(\bar{m} - m_c) \tag{A.9}$$

where the productivity function is substituted in for each case.

A.2 fmincon() Settings

To use the fmincon() function, lower and upper boundaries for the parameter estimates are set, and initializing parameters ω_{init} are provided.

For all of the aftershock models, the parameter estimate range can only be positive, thus setting the lower boundary for all parameters at 0. The upper boundary for MOL estimates is limited by a maximum value for individual parameters of $\omega_{upp} = \{10000.0, 10.0, 10.0\}$. When initiating the function to solve for the MLE, the initial parameters are set to $\omega_{init} = \{100.0, 0.05, 1.1\}$. For the CMOL, the upper bound on the parameter estimates is $\omega_{upp} = \{1000.0, 10.0, 10.0, 1000.0, 10.0, 10.0\}$ and the MLE estimation is initiated with parameter estimates $\omega_{init} = \{100.0, 0.2, 1.1, 38.0, 0.4, 1.6\}$. For the ETAS model, $\omega_{upp} = \{100.0, 1000.0, 10.0, 10.0, 10.0\}$ and the MLE estimation is initiated with parameter estimates $\omega_{init} = \{0.05, 0.1, 0.1, 0.1, 1.6\}$.

Appendix B

Additional Tables and Figures

B.1 The 2009 L'Aquila, Italy Sequence

Table B.1: The 2009 L'Aquila sequence model parameter estimates for the MOL using the MLE method and associated errors using 95% confidence intervals.

ΔT_m	β	±	K_0	±	c_0	±	p_0	±
1	2.66	*0.12*	309.57	*968.97*	0.61	*1.21*	2.49	*3.29*
2	2.55	*0.11*	209.46	*212.58*	0.44	*0.44*	2.05	*1.05*
3	2.50	*0.10*	141.82	*45.68*	0.21	*0.17*	1.38	*0.39*
4	2.43	*0.09*	134.01	*24.56*	0.11	*0.09*	1.05	*0.21*
5	2.43	*0.09*	134.57	*25.84*	0.12	*0.09*	1.09	*0.20*
6	2.43	*0.09*	133.65	*23.98*	0.11	*0.08*	1.05	*0.17*
7	2.45	*0.09*	132.53	*22.17*	0.10	*0.07*	1.01	*0.15*
10	2.44	*0.08*	130.59	*19.48*	0.08	*0.06*	0.95	*0.11*
14	2.46	*0.08*	132.46	*20.62*	0.10	*0.06*	0.99	*0.10*
21	2.47	*0.08*	133.60	*20.75*	0.10	*0.06*	1.01	*0.09*
30	2.48	*0.08*	136.72	*21.61*	0.12	*0.06*	1.04	*0.08*

Table B.2: The 2009 L'Aquila sequence model parameter estimates for the CMOL using the MLE method and associated errors using 95% confidence intervals.

ΔT_m	β	±	K_1	±	c_1	±	p_1	±
4	2.43	*0.09*	151.41	*210.35*	0.26	*4.95*	1.54	*126.69*
5	2.43	*0.09*	150.50	*68.60*	0.26	*0.28*	1.53	*0.72*
6	2.43	*0.09*	148.10	*61.39*	0.25	*0.18*	1.51	*0.40*
7	2.45	*0.09*	147.88	*17.18*	0.25	*0.11*	1.52	*0.41*
10	2.44	*0.08*	152.90	*27.35*	0.28	*0.10*	1.59	*0.31*
14	2.46	*0.08*	147.06	*1.92*	0.25	*0.01*	1.52	*0.02*
21	2.47	*0.08*	145.11	*15.13*	0.24	*0.06*	1.49	*0.17*
30	2.48	*0.08*	138.46	*733.39*	0.21	*6.31*	1.40	*2.56*

ΔT_m	K_2	±	c_2	±	p_2	±
4	212.09	*71.55*	0.05	*11.26*	1.10	*198.20*
5	12.38	*14.59*	0.04	*0.11*	1.05	*0.58*
6	17.18	*17.68*	0.02	*0.12*	0.75	*0.47*
7	21.08	*14.53*	0.01	*0.02*	0.61	*0.25*
10	26.21	*5.70*	0.002	*0.01*	0.46	*0.25*
14	23.95	*0.41*	0.004	*0.01*	0.53	*0.02*
21	23.12	*3.63*	0.01	*0.02*	0.55	*0.04*
30	21.12	*91.06*	0.01	*0.74*	0.61	*3.25*

Table B.3: The 2009 L'Aquila sequence model parameter estimates for the ETAS model using the MLE method and associated errors using a 95% confidence intervals.

ΔT_m	β	±	μ	±	K	±	c	±	p	±	α	±
1	2.54	*0.12*	0.17	*0.16*	0.74	*0.98*	0.48	*0.84*	3.21	*3.78*	1.97	*0.40*
2	2.46	*0.11*	0.19	*0.17*	16.00	*11.10*	0.04	*0.05*	2.12	*0.96*	1.01	*0.23*
3	2.43	*0.10*	0.18	*0.17*	10.50	*6.90*	0.06	*0.07*	2.17	*0.94*	1.15	*0.22*
4	2.37	*0.09*	0.18	*0.16*	11.00	*6.77*	0.05	*0.05*	2.05	*0.76*	1.14	*0.21*
5	2.37	*0.09*	0.17	*0.16*	9.96	*5.99*	0.05	*0.05*	1.99	*0.65*	1.18	*0.20*
6	2.38	*0.09*	0.16	*0.16*	10.40	*6.07*	0.04	*0.03*	1.80	*0.47*	1.18	*0.19*
7	2.40	*0.09*	0.15	*0.15*	11.00	*6.24*	0.03	*0.03*	1.66	*0.37*	1.18	*0.19*
10	2.39	*0.08*	0.14	*0.15*	10.20	*5.49*	0.03	*0.02*	1.52	*0.27*	1.21	*0.18*
14	2.41	*0.08*	0.13	*0.15*	8.32	*4.40*	0.03	*0.02*	1.48	*0.22*	1.29	*0.18*
21	2.42	*0.08*	0.13	*0.15*	4.87	*2.70*	0.03	*0.02*	1.40	*0.17*	1.47	*0.18*
30	2.44	*0.08*	0.13	*0.15*	2.68	*1.62*	0.04	*0.02*	1.34	*0.14*	1.68	*0.19*

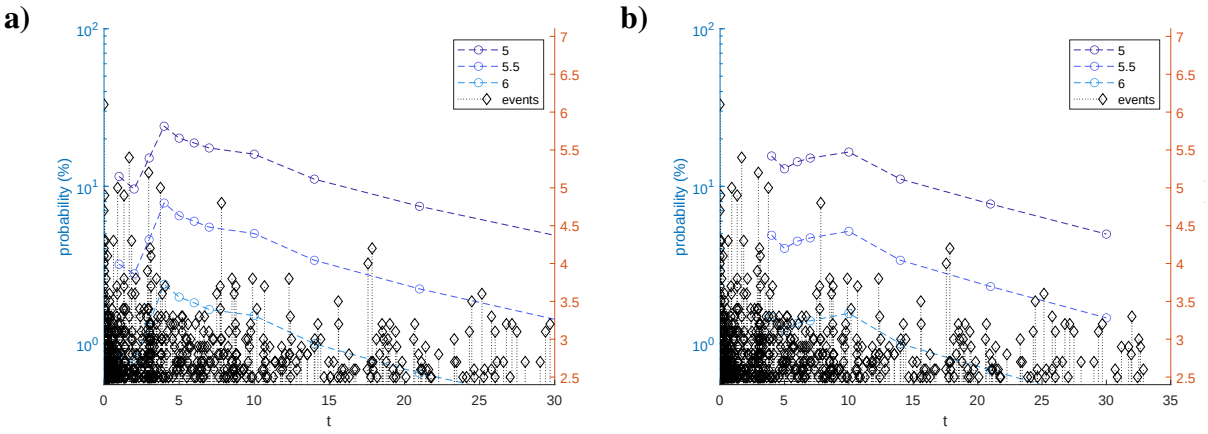

Figure B.1: Probability of large aftershocks for the L'Aquila sequence using the a) MOL and b) CMOL produced by the EVD.

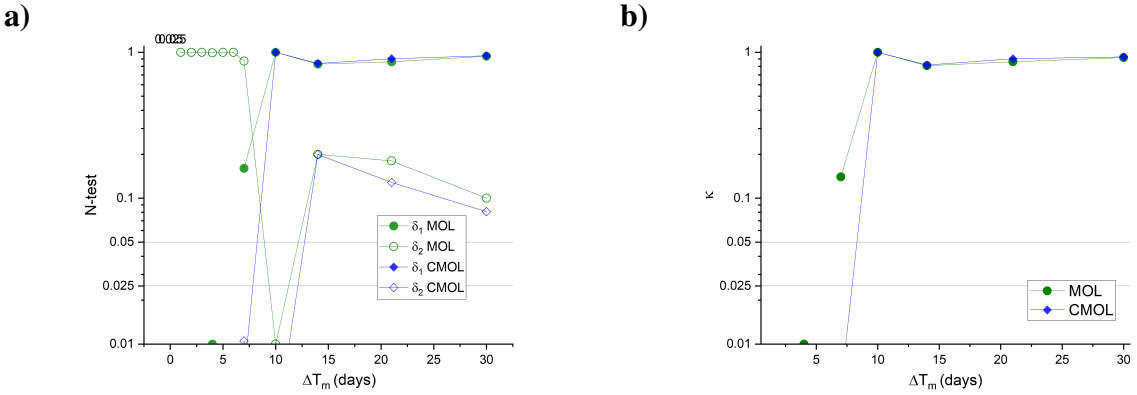

Figure B.2: The performance of the MOL and CMOL for various training time intervals for the L'Aquila sequence using the EVD method for forecasting. Forecast performance scores are listed for the a) N-test (δ_1, δ_2) and the b) M-test (κ).

Table B.4: Variance for 2009 L'Aquila sequence Gamma priors. Gamma prior means are provided using the MLE point parameter estimate. In order, the priors are for the MOL, CMOL, and ETAS model.

K	c	p
10.0	1e-3	0.01

K_1	c_1	p_1	K_2	c_2	p_2
1.0	1e-4	0.01	0.5	1e-7	0.01

μ	K	c	p	α
0.1	0.01	0.0001	0.05	0.1

Table B.5: MCMC sampling of model parameter estimates for the L'Aquila sequence fitted to the MOL. The 95% confidence intervals are indicated by the lower (-) and upper (+) bounds of the model parameter distribution.

ΔT_m	β	β -	β +	K	K -	K +	c	c -	c +	p	p -	p +
1	2.65	2.41	2.89	309.50	303.50	315.50	0.61	0.58	0.64	2.49	2.31	2.67
2	2.54	2.32	2.77	209.30	203.20	215.50	0.44	0.41	0.48	2.04	1.89	2.20
3	2.49	2.29	2.70	141.80	136.00	147.80	0.21	0.17	0.25	1.37	1.25	1.51
4	2.42	2.23	2.62	133.90	128.10	140.10	0.11	0.08	0.15	1.04	0.94	1.15
5	2.42	2.23	2.61	134.30	128.40	140.20	0.12	0.09	0.16	1.08	0.98	1.18
6	2.42	2.24	2.61	133.50	127.80	139.50	0.11	0.08	0.15	1.05	0.96	1.14
7	2.44	2.26	2.62	132.50	126.90	138.30	0.10	0.07	0.13	1.01	0.93	1.10
10	2.43	2.26	2.61	130.20	134.40	136.00	0.08	0.06	0.11	0.95	0.88	1.02
14	2.45	2.28	2.62	132.40	126.80	138.10	0.10	0.07	0.13	0.99	0.93	1.05
21	2.46	2.29	2.63	133.50	127.90	139.20	0.10	0.08	0.13	1.01	0.95	1.06
30	2.47	2.31	2.64	136.80	131.10	142.60	0.12	0.09	0.15	1.04	0.99	1.09

Table B.6: MCMC sampling of model parameter estimates for the L'Aquila sequence fitted to the CMOL. The 95% confidence intervals are indicated by the lower (-) and upper (+) bounds of the model parameter distribution.

ΔT_m	β	β-	β+	K_1	K_1-	K_1+	c_1	c_1-	c_1+	p_1	p_1-	p_1+
4	2.43	2.29	2.57	151.30	149.50	153.20	0.26	0.24	0.28	1.53	1.42	1.64
5	2.42	2.28	2.57	150.50	148.70	152.40	0.27	0.25	0.28	1.54	1.43	1.64
6	2.43	2.29	2.57	147.90	146.00	150.00	0.25	0.24	0.28	1.51	1.41	1.62
7	2.45	2.31	2.59	147.80	146.00	149.50	0.25	0.24	0.27	1.51	1.42	1.61
10	2.43	2.30	2.57	152.80	150.80	154.90	0.28	0.27	0.29	1.60	1.50	1.70
14	2.45	2.32	2.59	147.00	145.10	148.80	0.25	0.23	0.27	1.51	1.41	1.60
21	2.46	2.33	2.60	145.10	143.00	146.90	0.24	0.22	0.26	1.47	1.39	1.56
30	2.62	2.49	2.75	138.60	136.70	140.40	0.21	0.19	0.22	1.39	1.31	1.48

ΔT_m	K_2	K_2-	K_2+	c_2	c_2-	c_2+	p_2	p_2-	p_2+
4	12.10	10.76	13.37	0.050	0.049	0.051	1.09	0.96	1.22
5	12.40	11.00	13.84	0.040	0.039	0.041	1.03	0.89	1.17
6	17.19	15.79	18.57	0.020	0.019	0.021	0.75	0.62	0.88
7	21.07	19.69	22.42	0.008	0.007	0.009	0.60	0.49	0.72
10	26.20	24.92	27.56	0.003	0.002	0.004	0.45	0.34	0.56
14	23.87	22.56	25.23	0.005	0.004	0.006	0.53	0.44	0.62
21	23.08	21.77	24.46	0.006	0.005	0.007	0.56	0.47	0.65
30	21.07	19.85	22.41	0.009	0.008	0.010	0.62	0.53	0.70

Table B.7: MCMC sampling of model parameter estimates for the L'Aquila sequence fitted to the ETAS. The 95% confidence intervals are indicated by the lower (-) and upper (+) bounds of the model parameter distribution.

ΔT_m	β	β -	β +	μ	μ -	μ +	K	K -	K +	c	c -	c +	p	p -	p +	α	α -	α +
1	2.53	2.29	2.78	0.17	0.15	0.19	0.75	0.57	0.94	0.48	0.46	0.50	3.20	2.89	3.53	1.97	1.87	2.07
2	2.45	2.24	2.68	0.19	0.17	0.21	16.05	15.86	16.25	0.04	0.03	0.05	2.12	1.83	2.46	1.01	0.87	1.13
3	2.42	2.21	2.64	0.18	0.16	0.20	10.48	10.29	10.67	0.06	0.05	0.07	2.19	1.94	2.48	1.14	1.02	1.25
4	2.36	2.17	2.56	0.18	0.16	0.20	10.96	10.76	11.15	0.05	0.04	0.06	2.07	1.82	2.36	1.13	1.02	1.24
5	2.36	2.17	2.55	0.17	0.15	0.19	9.96	9.77	10.16	0.05	0.04	0.06	2.00	1.77	2.27	1.17	1.06	1.28
6	2.37	2.18	2.56	0.16	0.14	0.18	10.38	10.19	10.58	0.04	0.03	0.05	1.82	1.61	2.08	1.17	1.05	1.28
7	2.39	2.20	2.57	0.15	0.13	0.17	10.98	10.79	11.18	0.03	0.02	0.04	1.66	1.46	1.90	1.17	1.05	1.29
10	2.38	2.21	2.56	0.14	0.12	0.16	10.19	10.00	10.39	0.03	0.02	0.04	1.55	1.38	1.75	1.20	1.07	1.31
14	2.40	2.23	2.57	0.13	0.11	0.15	8.32	8.13	8.52	0.03	0.02	0.04	1.50	1.35	1.66	1.27	1.16	1.39
21	2.41	2.25	2.58	0.13	0.11	0.15	4.87	4.68	5.07	0.03	0.02	0.05	1.39	1.27	1.53	1.47	1.37	1.58
30	2.43	2.27	2.60	0.13	0.11	0.15	2.68	2.49	2.88	0.04	0.03	0.05	1.34	1.25	1.45	1.68	1.58	1.77

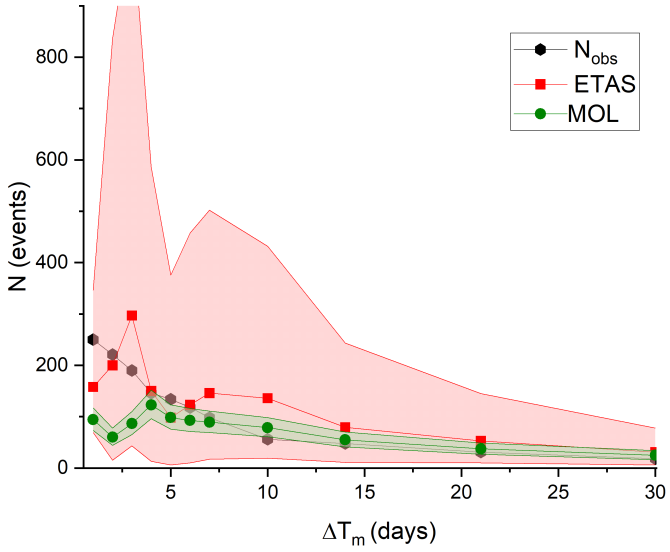

Figure B.3: Average number of events generated during seven day forecast for L'Aquila sequence using the BPD method.

B.2 The 2016 Amatrice, Italy Sequence

Table B.8: The 2016 Amatrice sequence model parameter estimates for the MOL using the MLE method and associated errors using a 95% confidence intervals.

ΔT_m	β	$\pm$	K_0	$\pm$	c_0	$\pm$	p_0	$\pm$
1	2.15	*0.10*	120.87	*36.42*	0.19	*0.24*	1.52	*0.91*
2	2.19	*0.09*	122.65	*44.34*	0.22	*0.18*	1.66	*0.58*
3	2.28	*0.09*	120.50	*19.31*	0.09	*0.07*	1.12	*0.23*
4	2.30	*0.09*	121.52	*18.70*	0.09	*0.07*	1.09	*0.19*
5	2.28	*0.09*	121.59	*18.77*	0.09	*0.06*	1.09	*0.17*
6	2.30	*0.08*	121.59	*18.03*	0.08	*0.06*	1.07	*0.15*
7	2.32	*0.08*	121.64	*18.60*	0.09	*0.06*	1.09	*0.14*
10	2.31	*0.08*	120.91	*17.27*	0.08	*0.05*	1.05	*0.11*
14	2.31	*0.08*	120.70	*16.46*	0.07	*0.04*	1.02	*0.10*
21	2.33	*0.08*	122.21	*17.28*	0.08	*0.04*	1.05	*0.09*
30	2.33	*0.07*	120.31	*16.03*	0.07	*0.04*	1.02	*0.07*

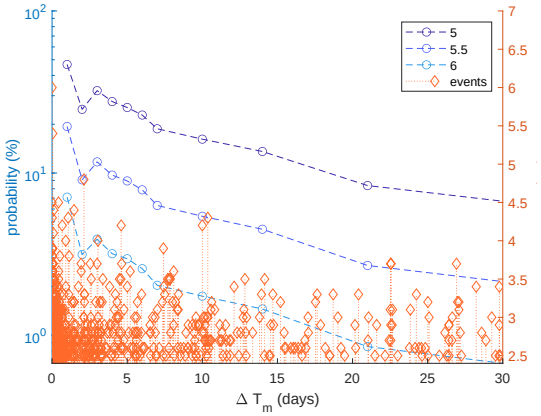

Figure B.4: Probability of large aftershocks for the Amatrice sequence using the MOL produced by the EVD.

Table B.9: The Amatrice sequence ETAS model parameters estimated using the MLE method without fixing of model parameters with associated 95% confidence intervals.

ΔT_m	β	±	μ	±	K	±	c	±	p	±	α	±
1	2.33	*0.11*	0.00	*303.00*	0.19	*1.40*	0.05	*0.21*	1.15	*2.01*	2.64	*2.08*
2	2.35	*0.10*	0.00	*57.80*	1.36	*2.85*	0.06	*0.12*	1.55	*1.36*	2.05	*0.67*
3	2.43	*0.10*	0.00	*36.90*	3.28	*4.45*	0.02	*0.04*	1.29	*0.68*	1.92	*0.44*
4	2.45	*0.10*	0.00	*23.90*	4.45	*5.03*	0.02	*0.03*	1.27	*0.52*	1.87	*0.37*
5	2.41	*0.09*	0.00	*18.50*	2.65	*3.13*	0.02	*0.03*	1.24	*0.46*	2.00	*0.38*
6	2.43	*0.09*	5.22	*13.70*	2.17	*2.58*	0.03	*0.04*	1.31	*0.48*	2.03	*0.38*
7	2.45	*0.09*	2.77	*11.30*	2.38	*2.69*	0.02	*0.03*	1.27	*0.41*	2.02	*0.37*
10	2.43	*0.09*	4.89	*7.33*	1.31	*1.56*	0.03	*0.04*	1.28	*0.37*	2.17	*0.37*
14	2.42	*0.08*	2.90	*5.44*	0.96	*1.11*	0.03	*0.03*	1.21	*0.29*	2.27	*0.36*
21	2.44	*0.08*	0.00	*3.58*	0.75	*0.90*	0.02	*0.03*	1.10	*0.22*	2.38	*0.38*
30	2.43	*0.08*	0.00	*2.31*	1.82	*1.62*	0.01	*0.01*	1.05	*0.15*	2.29	*0.28*

Table B.10: The 2016 Amatrice sequence model parameter estimates for the ETAS model using the MLE method and associated errors using a 95% confidence intervals where $\mu = 0.03$ is fixed. These model parameters were used as the Gamma prior mean during the MCMC sampling procedure.

ΔT_m	β	±	K	±	c	±	p	±	α	±
1	2.33	*0.11*	0.19	*1.40*	0.05	*0.21*	1.15	*2.01*	2.64	*2.08*
2	2.35	*0.10*	1.36	*2.85*	0.06	*0.12*	1.55	*1.36*	2.05	*0.67*
3	2.43	*0.10*	3.28	*4.45*	0.02	*0.04*	1.29	*0.68*	1.92	*0.44*
4	2.45	*0.10*	4.45	*5.02*	0.02	*0.03*	1.27	*0.52*	1.86	*0.37*
5	2.41	*0.09*	2.65	*3.13*	0.02	*0.03*	1.24	*0.46*	2.00	*0.38*
6	2.43	*0.09*	2.44	*2.91*	0.02	*0.03*	1.18	*0.39*	2.05	*0.38*
7	2.45	*0.09*	2.53	*2.88*	0.02	*0.02*	1.19	*0.37*	2.04	*0.37*
10	2.43	*0.09*	1.61	*1.92*	0.02	*0.02*	1.11	*0.28*	2.20	*0.37*
14	2.42	*0.08*	1.08	*1.27*	0.02	*0.02*	1.10	*0.24*	2.29	*0.36*
21	2.44	*0.08*	0.75	*0.90*	0.02	*0.03*	1.10	*0.22*	2.38	*0.38*
30	2.43	*0.08*	1.81	*1.61*	0.01	*0.01*	1.05	*0.15*	2.29	*0.28*

Table B.11: Variance for 2010 Amatrice sequence Gamma priors. Gamma prior means are provided using the MLE point parameter estimate. In order, the priors are for the MOL, and ETAS model.

	K	c	p	
	10.0	0.001	0.01	
μ	K	c	p	α
1e-7	0.001	1e-4	0.05	0.05

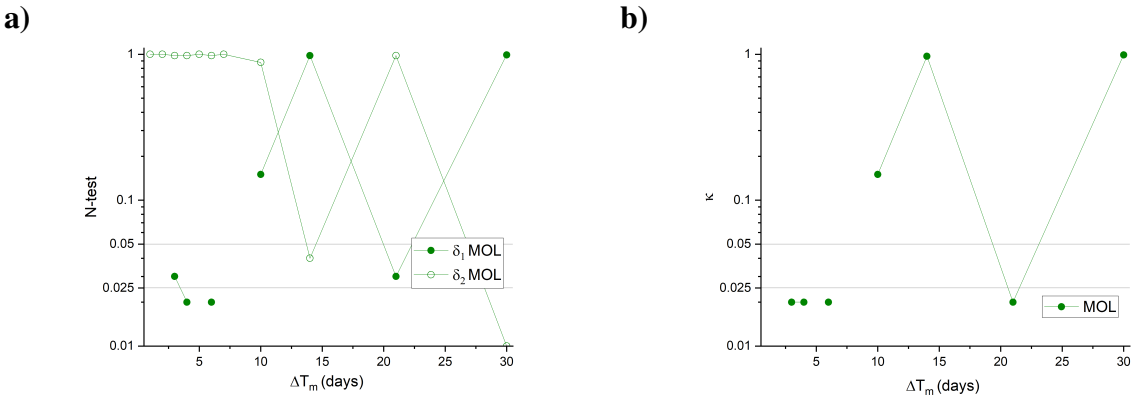

(a) *M*-test

Figure B.5: The performance of the MOL for various training time intervals for the Amatrice sequence using the EVD method for forecasting. Forecast performance scores are listed for the a) *N*-test (δ_1, δ_2) and the b) *M*-test (κ).

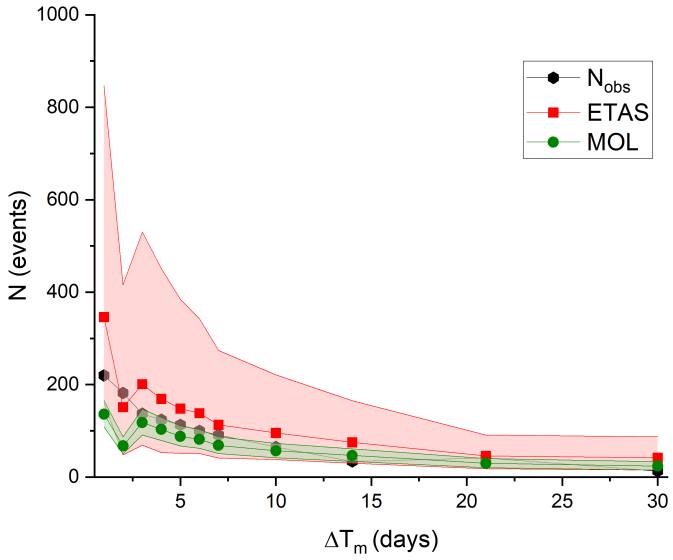

Figure B.6: Average number of events generated during seven day forecast for Amatrice sequence using the BPD method.

Table B.12: MCMC sampling of model parameter estimates for the Amatrice sequence fitted to the MOL. The 95% confidence intervals are indicated by the lower (-) and upper (+) bounds of the model parameter distribution.

ΔT_m	β	β -	β +	K	K -	K +	c	c -	c +	p	p -	p +
1	2.14	1.95	2.35	120.90	114.80	126.90	0.19	0.15	0.23	1.52	1.36	1.68
2	2.18	1.99	2.38	122.50	116.50	128.70	0.22	0.18	0.26	1.66	1.51	1.81
3	2.27	2.09	2.46	120.50	114.70	126.30	0.09	0.06	0.13	1.11	1.00	1.24
4	2.29	2.11	2.48	121.40	115.90	127.10	0.09	0.06	0.12	1.09	0.98	1.20
5	2.27	2.09	2.45	121.60	116.00	127.30	0.09	0.06	0.12	1.09	0.99	1.19
6	2.29	2.12	2.47	121.40	115.70	127.10	0.08	0.06	0.11	1.06	0.97	1.16
7	2.31	2.14	2.49	121.40	115.70	127.10	0.09	0.06	0.12	1.09	1.00	1.18
10	2.30	2.13	2.48	120.80	115.20	126.60	0.08	0.05	0.10	1.05	0.97	1.12
14	2.30	2.14	2.47	120.50	115.10	126.10	0.07	0.05	0.09	1.02	0.95	1.08
21	2.32	2.16	2.49	122.10	116.50	127.70	0.08	0.06	0.10	1.05	1.00	1.11
30	2.32	2.17	2.48	120.10	114.70	125.80	0.07	0.05	0.09	1.02	0.97	1.07

Table B.13: MCMC sampling of model parameter estimates for the Amatrice sequence fitted to the ETAS model. The 95% confidence intervals are indicated by the lower (-) and upper (+) bounds of the model parameter distribution.

ΔT_m	β	β -	β +	μ	μ -	μ +	K	K -	K +	c	c -	c +	p	p -	p +	α	α -	α +
1	2.32	2.11	2.54	0.03	0.03	0.03	0.19	0.13	0.26	0.05	0.03	0.07	1.13	0.97	1.31	2.65	2.52	2.77
2	2.34	2.14	2.55	0.03	0.03	0.03	1.36	1.30	1.42	0.06	0.04	0.08	1.54	1.37	1.73	2.05	1.96	2.14
3	2.42	2.23	2.63	0.03	0.03	0.03	3.28	3.22	3.34	0.02	0.01	0.04	1.29	1.11	1.51	1.93	1.78	2.09
4	2.44	2.25	2.64	0.03	0.03	0.03	4.45	4.39	4.51	0.02	0.01	0.03	1.29	1.13	1.50	1.85	1.70	2.00
5	2.40	2.22	2.60	0.03	0.03	0.03	2.65	2.59	2.71	0.02	0.01	0.04	1.25	1.09	1.44	2.00	1.85	2.17
6	2.42	2.24	2.61	0.03	0.03	0.03	2.44	2.38	2.50	0.02	0.01	0.03	1.19	1.07	1.35	2.04	1.89	2.20
7	2.44	0.26	2.63	0.03	0.03	0.03	2.53	2.47	2.59	0.02	0.01	0.03	1.20	1.08	1.35	2.03	1.89	2.19
10	2.42	2.24	2.60	0.03	0.03	0.03	1.61	1.55	1.67	0.02	0.01	0.03	1.12	1.01	1.24	2.20	2.05	2.37
14	2.41	2.24	2.58	0.03	0.03	0.03	1.08	1.02	1.14	0.02	0.01	0.03	1.10	1.01	1.20	2.29	2.16	2.44
21	2.43	2.26	2.60	0.03	0.03	0.03	0.75	0.69	0.81	0.02	0.01	0.03	1.09	1.01	1.17	2.40	2.28	2.56
30	2.42	2.26	2.59	0.03	0.03	0.03	1.81	1.75	1.87	0.01	0.00	0.02	1.05	0.99	1.13	2.30	2.13	2.47

B.3 The 2016 Kumamoto, Japan, Sequence

Table B.14: The 2016 Kumamoto sequence model parameter estimates for the MOL using the MLE method and associated errors using a 95% confidence intervals.

ΔT_m	β	$\pm$	K_0	$\pm$	c_0	$\pm$	p_0	$\pm$
1	2.03	*0.09*	60.42	*17.11*	0.02	*0.02*	1.26	*0.24*
2	2.04	*0.09*	63.50	*11.69*	0.02	*0.01*	1.22	*0.17*
3	2.06	*0.08*	71.62	*10.40*	0.02	*0.01*	1.12	*0.12*
4	2.03	*0.08*	78.27	*9.77*	0.01	*0.01*	1.05	*0.10*
5	2.06	*0.08*	82.85	*9.35*	0.01	*0.01*	1.01	*0.09*
6	2.08	*0.08*	82.91	*8.94*	0.01	*0.01*	1.01	*0.08*
7	2.10	*0.08*	83.06	*8.67*	0.01	*0.01*	1.01	*0.08*
10	2.11	*0.08*	78.88	*8.11*	0.01	*0.01*	1.05	*0.07*
14	2.11	*0.08*	79.25	*7.85*	0.01	*0.01*	1.05	*0.07*
21	2.11	*0.07*	81.20	*7.65*	0.01	*0.01*	1.02	*0.06*
30	2.12	*0.07*	80.48	*7.57*	0.01	*0.01*	1.03	*0.05*

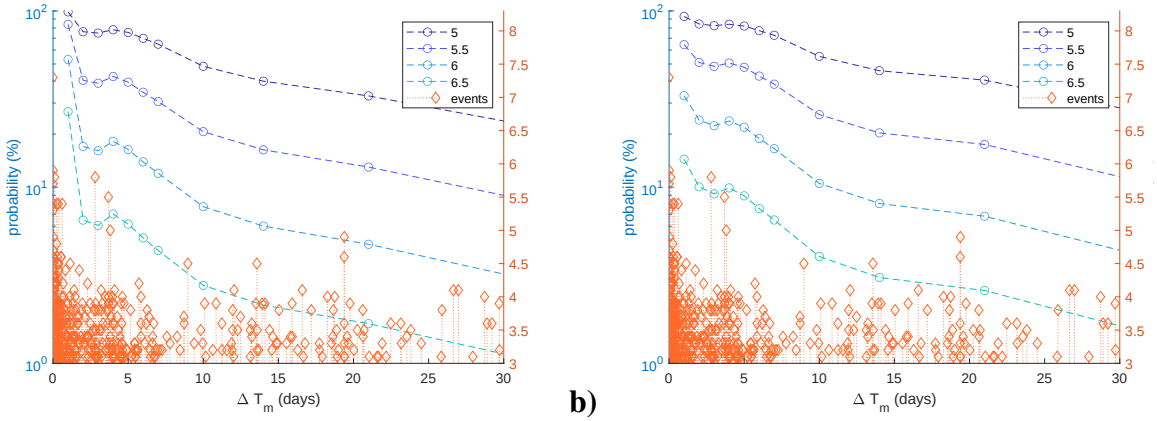

Figure B.7: Probability of large aftershocks for the Kumamoto sequence using the a) MOL and b) CMOL produced by the EVD.

Table B.15: The 2016 Kumamoto sequence model parameter estimates for the CMOL using the MLE method and associated errors using a 95% confidence intervals.

ΔT_m	β	±	K_1	±	c_1	±	p_1	±
1	1.89	*0.07*	26.28	*5.54*	0.03	*0.05*	1.25	*0.28*
2	1.91	*0.07*	26.55	*7.77*	0.03	*0.03*	1.23	*0.44*
3	1.93	*0.07*	28.65	*4.16*	0.02	*0.02*	1.15	*0.20*
4	1.91	*0.07*	31.26	*6.04*	0.02	*0.22*	1.06	*1.78*
5	1.94	*0.06*	34.18	*2.07*	0.01	*0.01*	0.98	*0.04*
6	1.96	*0.06*	34.47	*1.69*	0.01	*0.01*	0.97	*0.02*
7	1.97	*0.06*	34.93	*9.82*	0.01	*0.02*	0.96	*0.26*
10	1.98	*0.06*	29.81	*33.17*	0.02	*0.22*	1.11	*0.13*
14	1.98	*0.06*	30.71	*7.99*	0.02	*0.10*	1.08	*0.16*
21	1.99	*0.06*	38.30	*11.77*	0.01	*0.01*	0.89	*0.20*
30	2.00	*0.06*	34.59	*11.44*	0.01	*0.02*	0.97	*0.30*

ΔT_m	K_2	±	c_2	±	p_2	±
1	50.84	*8.19*	0.03	*0.02*	1.38	*0.18*
2	53.49	*5.07*	0.03	*0.02*	1.34	*0.92*
3	59.42	*13.45*	0.02	*0.01*	1.24	*0.36*
4	63.54	*15.03*	0.02	*0.01*	1.18	*0.12*
5	65.19	*2.89*	0.02	*0.01*	1.15	*0.07*
6	65.03	*3.88*	0.02	*0.00*	1.15	*0.02*
7	64.72	*10.90*	0.02	*0.01*	1.15	*0.62*
10	66.42	*52.98*	0.02	*0.04*	1.15	*1.21*
14	65.98	*17.50*	0.02	*0.08*	1.15	*0.74*
21	57.78	*23.04*	0.02	*0.01*	1.23	*0.26*
30	62.61	*20.95*	0.02	*0.01*	1.18	*0.22*

Table B.16: The 2016 Kumamoto sequence model parameter estimates for the ETAS model using the MLE method and associated errors using a 95% confidence intervals.

ΔT_m	β	±	μ	±	K	±	c	±	p	±	α	±
1	1.91	*0.07*	15.10	*18.30*	0.44	*0.55*	0.03	*0.02*	1.58	*0.41*	2.25	*0.30*
2	1.92	*0.07*	15.50	*16.60*	0.39	*0.49*	0.03	*0.02*	1.55	*0.38*	2.28	*0.29*
3	1.95	*0.07*	15.40	*13.30*	0.43	*0.49*	0.03	*0.02*	1.55	*0.37*	2.26	*0.27*
4	1.92	*0.07*	15.00	*11.20*	0.51	*0.55*	0.03	*0.02*	1.53	*0.34*	2.23	*0.26*
5	1.96	*0.07*	17.10	*9.13*	0.51	*0.55*	0.03	*0.02*	1.56	*0.34*	2.22	*0.25*
6	1.97	*0.07*	13.90	*7.65*	0.59	*0.61*	0.03	*0.02*	1.50	*0.29*	2.20	*0.25*
7	1.99	*0.07*	11.90	*6.52*	0.61	*0.62*	0.02	*0.02*	1.46	*0.26*	2.19	*0.24*
10	2.00	*0.07*	1.69	*4.42*	0.89	*0.85*	0.02	*0.01*	1.26	*0.16*	2.12	*0.23*
14	2.00	*0.07*	1.95	*2.96*	1.06	*0.97*	0.02	*0.01*	1.26	*0.15*	2.08	*0.22*
21	2.01	*0.06*	2.39	*1.96*	1.24	*1.06*	0.01	*0.01*	1.27	*0.13*	2.05	*0.20*
30	2.02	*0.06*	1.17	*1.31*	1.22	*1.01*	0.01	*0.01*	1.23	*0.11*	2.06	*0.20*

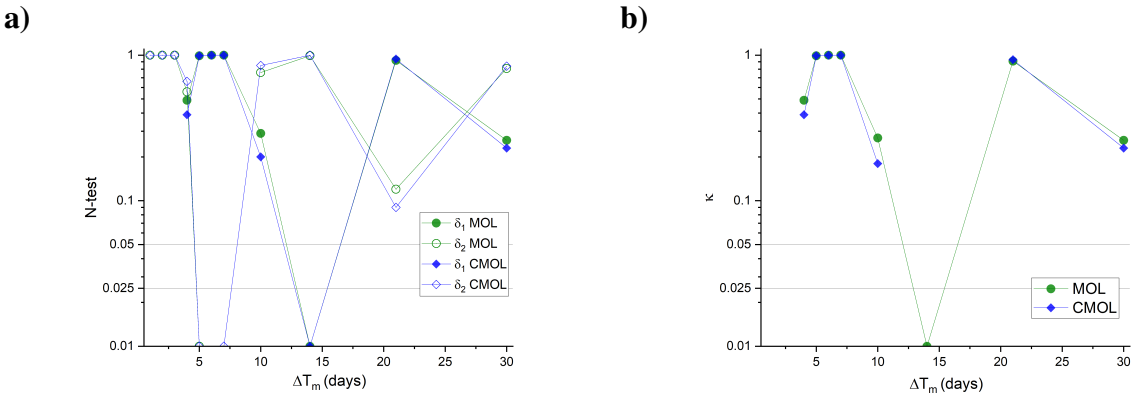

Figure B.8: The performance of the MOL and CMOL for various training time intervals for the Kumamoto sequence using the EVD method for forecasting. Forecast performance scores are listed for the a) N-test (δ_1, δ_2) and the b) M-test (κ).

Table B.17: Variance for 2016 Kumamoto sequence Gamma priors. Gamma prior means are provided using the MLE point parameter estimate. In order, the priors are for the MOL, CMOL, and ETAS model.

K	c	p
10.0	1e-5	0.01

K_1	c_1	p_1	K_2	c_2	p_2
1.0	1e-6	0.005	1.0	1e-4	0.01

μ	K	c	p	α
0.1	0.01	1e-7	0.01	0.1

Table B.18: MCMC sampling of model parameter estimates for the Kumamoto sequence fitted to the MOL. The 95% confidence intervals are indicated by the lower (-) and upper (+) bounds of the model parameter distribution.

ΔT_m	β	β -	β +	K	K -	K +	c	c -	c +	p	p -	p +
1	1.78	1.68	1.89	91.54	84.73	98.66	0.08	0.07	0.10	1.88	1.74	2.02
2	2.04	1.86	2.22	63.43	58.37	68.64	0.02	0.02	0.03	1.21	1.14	1.28
3	2.06	1.89	2.24	71.73	66.64	77.04	0.02	0.01	0.02	1.14	1.08	1.21
4	2.02	18.58	2.19	78.11	73.30	83.24	0.01	0.01	0.00	1.04	0.98	1.10
5	2.06	1.90	2.23	82.84	78.20	87.88	0.01	0.01	0.02	1.01	0.95	1.07
6	2.08	1.91	2.24	82.89	78.43	87.93	0.01	0.01	0.02	1.01	0.95	1.06
7	2.10	1.93	2.26	82.92	77.87	87.83	0.01	0.01	0.02	1.00	0.95	1.06
10	2.10	1.94	2.27	78.58	73.95	83.87	0.01	0.01	0.02	1.04	0.99	1.10
14	2.10	1.94	2.27	78.96	74.34	84.07	0.01	0.01	0.02	1.04	0.99	1.09
21	2.10	1.95	2.26	80.97	76.53	85.16	0.01	0.01	0.02	1.02	0.97	1.06
30	2.11	1.96	2.27	80.22	75.83	84.98	0.01	0.01	0.02	1.03	0.98	1.07

Table B.19: MCMC sampling of model parameter estimates for the Kumamoto sequence fitted to the CMOL. The 95% confidence intervals are indicated by the lower (-) and upper (+) bounds of the model parameter distribution.

ΔT_m	β	β-	β+	K_1	K_1-	K_1+	c_1	c_1-	c_1+	p_1	p_1-	p_1+
1	1.88	1.74	2.04	26.11	24.26	28.02	0.030	0.028	0.032	1.24	1.17	1.31
2	1.90	1.76	2.05	26.45	24.61	28.41	0.030	0.028	0.032	1.23	1.16	1.30
3	1.93	1.79	2.07	28.51	26.65	30.34	0.020	0.018	0.022	1.12	1.06	1.18
4	1.91	1.77	2.05	31.11	29.16	33.12	0.020	0.018	0.022	1.08	1.01	1.14
5	1.94	1.80	2.08	34.09	32.17	36.07	0.010	0.008	0.012	0.96	0.90	1.02
6	1.95	1.82	2.09	34.30	32.33	36.24	0.010	0.008	0.012	0.96	0.90	1.02
7	1.97	1.83	2.11	34.76	32.69	36.79	0.010	0.008	0.012	0.95	0.89	1.01
10	1.97	1.84	2.12	29.76	27.74	31.62	0.020	0.018	0.022	1.10	1.04	1.17
14	1.98	1.85	2.12	30.54	28.66	32.46	0.020	0.018	0.022	1.09	1.02	1.15
21	1.99	1.86	2.12	37.94	36.01	39.97	0.010	0.008	0.012	0.91	0.85	0.97
30	1.99	1.86	2.13	34.52	32.65	36.46	0.010	0.008	0.012	0.96	0.90	1.02

ΔT_m	K_2	K_2-	K_2+	c_2	c_2-	c_2+	p_2	p_2-	p_2+
1	50.84	48.86	52.75	0.032	0.022	0.046	1.37	1.27	1.49
2	53.34	51.37	55.33	0.031	0.021	0.044	1.34	1.25	1.45
3	59.40	57.50	61.32	0.024	0.015	0.034	1.24	1.15	1.33
4	63.54	61.64	65.49	0.020	0.013	0.030	1.18	1.10	1.25
5	65.14	63.19	67.06	0.019	0.012	0.028	1.15	1.07	1.24
6	64.98	63.09	66.92	0.019	0.012	0.028	1.15	1.07	1.23
7	64.70	62.77	66.67	0.019	0.012	0.028	1.15	1.08	1.24
10	66.40	64.55	68.32	0.020	0.012	0.029	1.16	1.09	1.24
14	66.00	64.08	67.81	0.019	0.012	0.028	1.15	1.08	1.23
21	57.81	55.91	59.79	0.021	0.014	0.031	1.22	1.14	1.31
30	62.57	60.65	64.49	0.020	0.013	0.029	1.18	1.11	1.26

Table B.20: MCMC sampling of model parameter estimates for the Kumamoto sequence fitted to the ETAS model. The 95% confidence intervals are indicated by the lower (-) and upper (+) bounds of the model parameter distribution.

ΔT_m	β	β -	β +	μ	μ -	μ +	K	K -	K +	c	c -	c +	p	p -	p +	α	α -	α +
1	1.90	1.74	2.07	15.11	14.49	15.76	0.46	0.30	0.66	0.03	0.03	0.03	1.55	1.45	1.65	2.26	2.15	2.36
2	1.92	1.76	2.08	15.49	14.88	16.14	0.41	0.27	0.62	0.03	0.03	0.03	1.53	1.45	1.63	2.28	2.16	2.39
3	1.94	1.79	2.10	15.37	14.84	16.00	0.43	0.27	0.62	0.03	0.03	0.03	1.54	1.46	1.63	2.27	2.16	2.38
4	1.92	1.77	2.07	14.95	14.35	15.59	0.52	0.36	0.71	0.03	0.03	0.03	1.55	1.47	1.63	2.22	2.12	2.32
5	1.95	1.81	2.10	17.10	16.49	17.74	0.51	0.35	0.71	0.03	0.03	0.03	1.57	1.48	1.65	2.23	2.22	2.33
6	1.97	1.82	2.12	13.91	13.30	14.54	0.58	0.42	0.78	0.03	0.03	0.03	1.54	1.46	1.62	2.19	2.10	2.28
7	1.98	1.84	2.14	12.92	12.31	13.55	0.63	0.45	0.83	0.02	0.02	0.02	1.41	1.34	1.48	2.22	2.13	2.31
10	1.99	1.85	2.14	16.60	16.00	17.23	0.87	0.69	1.07	0.02	0.02	0.02	1.48	1.41	1.55	2.14	2.07	2.21
14	1.99	1.85	2.14	2.00	1.43	2.69	1.04	0.86	1.23	0.02	0.02	0.02	1.32	1.27	1.37	2.05	1.98	2.11
21	2.00	1.86	2.15	2.33	1.79	2.94	1.27	1.08	1.47	0.01	0.01	0.01	1.21	1.17	1.25	2.10	2.04	2.16
30	2.01	1.87	2.15	1.17	0.68	1.75	1.24	1.05	1.44	0.01	0.01	0.01	1.19	1.15	1.23	2.06	2.04	2.16

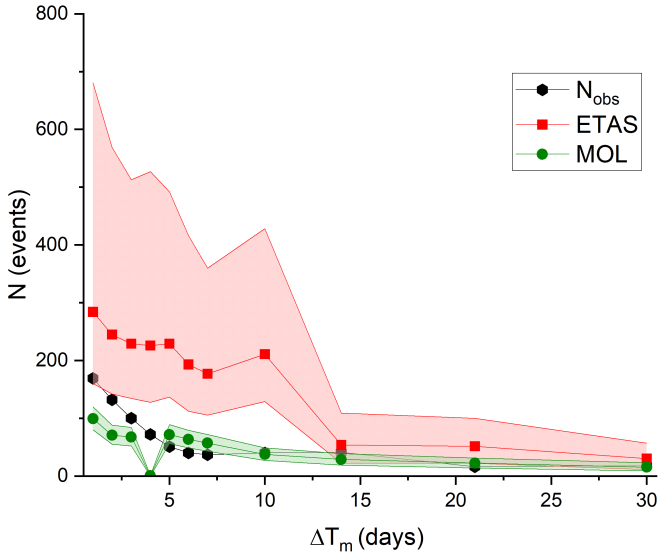

Figure B.9: Average number of events generated during seven day forecast for Kumamoto sequence using the BPD method.

B.4 The 2020 Monte Cristo Range, United States of America, Sequence

Table B.21: The 2020 Monte Cristo Range sequence model parameter estimates for the MOL using the MLE method and associated errors using a 95% confidence intervals.

ΔT_m	β	$\pm$	K_0	$\pm$	c_0	$\pm$	p_0	$\pm$
1	0.82	*0.10*	33.82	*17.11*	0.17	*0.02*	0.49	*0.41*
2	0.90	*0.09*	22.69	*11.69*	0.15	*0.01*	0.55	*0.26*
3	0.89	*0.09*	87.95	*10.40*	0.41	*0.01*	0.95	*0.47*
4	0.90	*0.08*	94.85	*9.77*	0.40	*0.01*	1.01	*0.41*
5	0.91	*0.08*	53.63	*9.35*	0.26	*0.01*	0.87	*0.26*
6	0.91	*0.08*	35.03	*8.94*	0.17	*0.01*	0.76	*0.19*
7	0.91	*0.07*	49.51	*8.67*	0.23	*0.01*	0.87	*0.21*
10	0.92	*0.07*	63.63	*8.11*	0.27	*0.01*	0.97	*0.20*
14	0.93	*0.07*	54.97	*7.85*	0.23	*0.01*	0.96	*0.16*
21	0.95	*0.07*	69.23	*7.65*	0.27	*0.01*	1.06	*0.15*
30	0.95	*0.06*	53.43	*7.57*	0.22	*0.01*	1.01	*0.11*

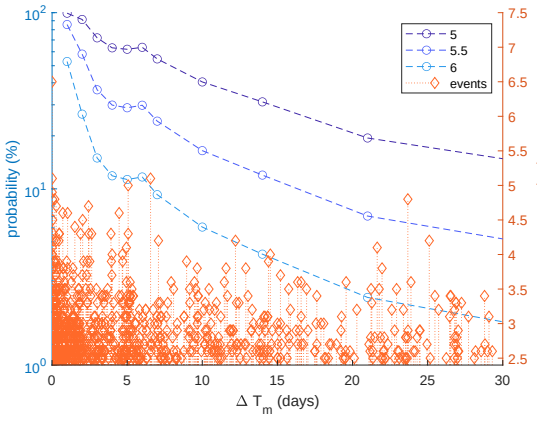

Figure B.10: Probability of large aftershocks for the Monte Cristo Range sequence using the MOL produced by the EVD.

Table B.22: Monte Cristo Range sequence ETAS model parameters estimated using the MLE method without fixing of model parameters with associated 95% confidence intervals.

ΔT_m	β	±	μ	±	K	±	c	±	p	±	α	±
1	2.05	*0.11*	100.00	*503.00*	0.0008	*0.1310*	0.03	*0.46*	0.79	*4.33*	3.54	*43.60*
2	2.20	*0.10*	47.30	*279.00*	0.0002	*0.0403*	0.04	*0.36*	0.70	*2.04*	3.80	*45.80*
3	2.17	*0.09*	0.00	*231.00*	0.0000	*0.0033*	0.28	*1.25*	0.94	*2.69*	4.23	*33.30*
4	2.16	*0.09*	0.00	*132.00*	0.0000	*0.0027*	0.34	*1.16*	1.01	*2.10*	4.09	*16.00*
5	2.18	*0.08*	0.00	*92.50*	0.0000	*0.0050*	0.21	*0.61*	0.86	*1.22*	4.12	*30.40*
6	2.18	*0.08*	0.00	*70.90*	0.0830	*0.2510*	0.19	*0.48*	1.03	*1.22*	2.21	*0.77*
7	2.17	*0.08*	0.00	*52.70*	0.0552	*0.1620*	0.35	*0.77*	1.23	*1.44*	2.28	*0.76*
10	2.19	*0.07*	0.00	*25.00*	0.1170	*0.2220*	0.44	*0.73*	1.47	*1.45*	2.07	*0.53*
14	2.22	*0.07*	0.00	*18.20*	0.0344	*0.0988*	0.32	*0.48*	1.15	*0.84*	2.40	*0.76*
21	2.24	*0.07*	0.00	*9.36*	0.0505	*0.1220*	0.36	*0.41*	1.22	*0.69*	2.30	*0.64*
30	2.26	*0.07*	0.00	*5.52*	0.0294	*0.0664*	0.32	*0.31*	1.12	*0.42*	2.45	*0.58*

Table B.23: Monte Cristo Range sequence ETAS model parameters estimated using the MLE method with the μ parameter fixed to $\mu = 0.0$ with associated 95% confidence intervals. Some errors are so small that they are reported here as less than 0.01.

ΔT_m	β	±	K	±	c	±	p	±	α	±
1	2.05	*0.11*	6e-5	*< 0.01*	0.001	*< 0.01*	0.42	*< 0.01*	4.44	< 0.01
2	2.20	*0.10*	2e-4	*0.02*	0.013	*0.24*	0.49	*1.44*	3.95	*34.50*
3	2.17	*0.09*	1e-5	*< 0.01*	0.283	*1.27*	0.94	*2.72*	4.46	*27.80*
4	2.16	*0.09*	3e-5	*< 0.01*	0.342	*1.17*	1.01	*2.10*	4.20	*18.70*
5	2.18	*0.08*	6e-5	*0.01*	0.206	*0.61*	0.86	*1.22*	4.05	*27.70*
6	2.18	*0.08*	0.08	*0.25*	0.189	*0.48*	1.03	*1.22*	2.21	*0.77*
7	2.17	*0.08*	0.06	*0.16*	0.351	*0.77*	1.23	*1.44*	2.28	*0.76*
10	2.19	*0.07*	0.12	*0.22*	0.435	*0.73*	1.47	*1.45*	2.07	*0.53*
14	2.22	*0.07*	0.03	*0.10*	0.324	*0.48*	1.15	*0.84*	2.40	*0.76*
21	2.24	*0.07*	0.05	*0.12*	0.357	*0.41*	1.22	*0.69*	2.30	*0.64*
30	2.26	*0.07*	0.03	*0.07*	0.316	*0.31*	1.12	*0.42*	2.45	*0.58*

Table B.24: The 2020 Monte Cristo Range sequence model parameter estimates for the ETAS model using the MLE method and associated errors using a 95% confidence intervals. The model parameters $\mu = 0.0$ and $K = 0.1$ were fixed. The model parameter $c = 0.3$ was fixed for $\Delta T_m = 1, 2$ days for stability. These model parameters were used as the Gamma prior mean during the MCMC sampling procedure.

ΔT_m	β	$\pm$	c	$\pm$	p	$\pm$	α	$\pm$
1	2.05	*0.11*	0.30	*N/A*	1.17	*18.10*	2.11	*5.20*
2	2.20	*0.10*	0.30	*N/A*	1.08	*6.38*	2.10	*3.59*
3	2.17	*0.09*	0.27	*1.12*	1.17	*3.24*	2.13	*1.93*
4	2.16	*0.09*	0.29	*0.96*	1.22	*2.88*	2.13	*1.51*
5	2.18	*0.08*	0.24	*0.65*	1.13	*1.79*	2.14	*1.21*
6	2.18	*0.08*	0.19	*0.48*	1.06	*1.26*	2.16	*0.73*
7	2.17	*0.08*	0.37	*0.79*	1.35	*1.62*	2.12	*0.62*
10	2.19	*0.07*	0.44	*0.74*	1.45	*1.43*	2.11	*0.55*
14	2.22	*0.07*	0.29	*0.41*	1.24	*0.86*	2.13	*0.55*
21	2.24	*0.07*	0.32	*0.35*	1.27	*0.67*	2.13	*0.51*
30	2.26	*0.07*	0.26	*0.26*	1.20	*0.43*	2.14	*0.41*

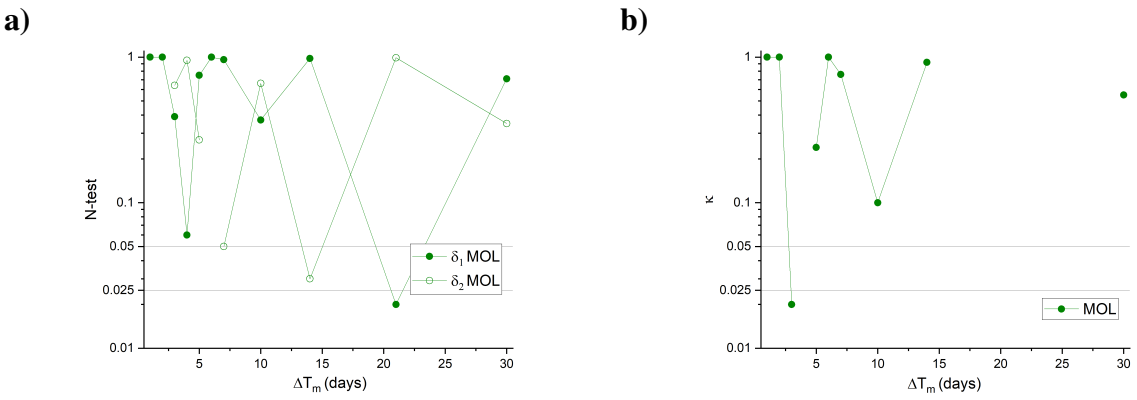

(a) M-test

Figure B.11: The performance of the MOL for various training time intervals for the Monte Cristo Range sequence using the EVD method for forecasting. Forecast performance scores are listed for the a) N-test (δ_1, δ_2) and the b) M-test (κ).

Table B.25: Variance for 2020 Monte Cristo Range sequence Gamma priors. Gamma prior means are provided using the MLE point parameter estimate. In order, the priors are for the MOL and ETAS model

	K	c	p	
	10.0	1e-3	0.01	
μ	K	c	p	α
1e-7	1e-3	1e-4	0.01	0.05

Table B.26: MCMC sampling of model parameter estimates for the Monte Cristo Range sequence fitted to the MOL. The 95% confidence intervals are indicated by the lower (-) and upper (+) bounds of the model parameter distribution.

ΔT_m	β	β -	β +	K	K -	K +	c	c -	c +	p	p -	p +
1	1.90	1.70	2.11	158.40	152.20	164.40	0.05	0.01	0.11	0.48	0.38	0.61
2	2.08	1.89	2.27	151.60	145.80	157.50	0.06	0.02	0.12	0.54	0.43	0.66
3	2.06	1.88	2.24	174.60	169.00	180.50	0.28	0.23	0.33	0.93	0.82	1.05
4	2.07	1.90	2.24	184.80	179.00	191.10	0.34	0.30	0.39	1.00	0.90	1.11
5	2.09	1.92	2.26	161.80	155.90	167.60	0.23	0.19	0.28	0.87	0.78	0.96
6	2.10	1.94	2.26	149.30	143.50	154.90	0.16	0.12	0.21	0.76	0.69	0.84
7	2.09	1.94	2.26	163.70	157.90	169.50	0.24	0.20	0.29	0.87	0.80	0.95
10	2.12	1.96	2.27	184.70	179.00	190.70	0.33	0.28	0.38	0.97	0.91	1.04
14	2.15	2.01	2.30	182.30	176.80	188.30	0.32	0.28	0.37	0.96	0.91	1.02
21	2.18	2.04	2.33	212.80	206.90	218.60	0.45	0.40	0.50	1.06	1.01	1.10
30	2.20	2.06	2.34	197.80	192.10	203.80	0.39	0.34	0.44	1.01	0.97	1.05

Table B.27: MCMC sampling of model parameter estimates for the Monte Cristo Range sequence fitted to the ETAS model. The 95% confidence intervals are indicated by the lower (-) and upper (+) bounds of the model parameter distribution.

ΔT_m	β	β -	β +	μ	μ -	μ +	K	K -	K +	c	c -	c +	p	p -	p +	α	α -	α +
1	2.05	1.83	2.28	0.00	0.00	0.00	0.10	0.06	0.16	0.30	0.28	0.32	1.17	1.00	1.34	2.12	1.96	2.28
2	2.20	2.01	2.41	0.00	0.00	0.00	0.10	0.06	0.16	0.30	0.28	0.32	1.08	0.09	1.22	2.10	1.96	2.26
3	2.17	1.98	2.36	0.00	0.00	0.00	0.09	0.05	0.15	0.27	0.25	0.29	1.17	1.04	1.30	2.16	2.00	2.31
4	2.17	1.99	2.35	0.00	0.00	0.00	0.09	0.04	0.15	0.29	0.27	0.31	1.20	1.08	1.33	2.17	2.01	2.36
5	2.18	2.01	2.35	0.00	0.00	0.00	0.10	0.05	0.16	0.24	0.22	2.59	1.12	1.01	1.24	2.16	1.99	2.34
6	2.18	2.01	2.35	0.00	0.00	0.00	0.10	0.06	0.16	0.19	0.17	0.31	1.06	0.96	1.16	2.16	2.02	2.29
7	2.19	2.04	2.35	0.00	0.00	0.00	0.11	0.07	0.16	0.44	0.42	0.46	1.46	1.34	1.58	2.10	1.96	2.25
10	2.19	2.04	2.35	0.00	0.00	0.00	0.11	0.06	0.16	0.44	0.42	0.46	1.46	1.34	1.58	2.10	1.96	2.25
14	2.22	2.07	2.38	0.00	0.00	0.00	0.10	0.06	0.16	0.29	0.27	0.31	1.24	1.15	1.34	2.14	2.00	2.29
21	2.24	2.10	2.40	0.00	0.00	0.00	0.10	0.06	0.15	0.31	0.29	0.33	1.26	1.18	1.35	2.13	2.01	2.29
30	2.26	2.12	2.41	0.00	0.00	0.00	0.10	0.05	0.16	0.26	0.24	0.28	1.20	1.12	1.28	2.14	2.00	2.32

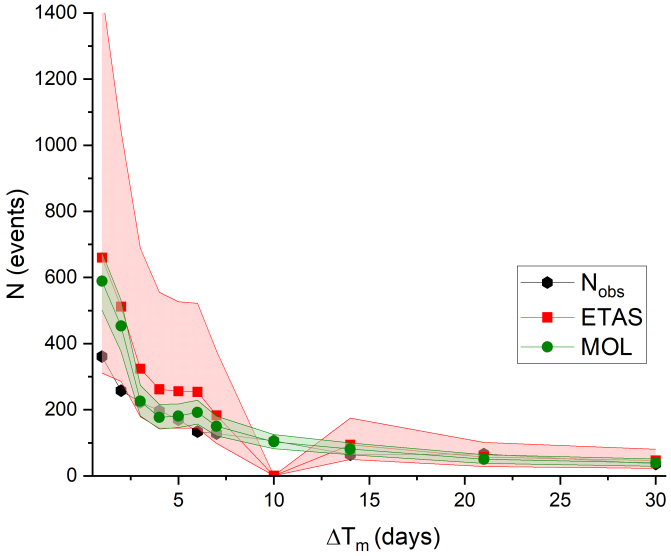

Figure B.12: Average number of events generated during seven day forecast for Monte Cristo Range sequence using the BPD method.

B.5 The 2010 Darfield Sequence and 2011 Christchurch Events, New Zealand

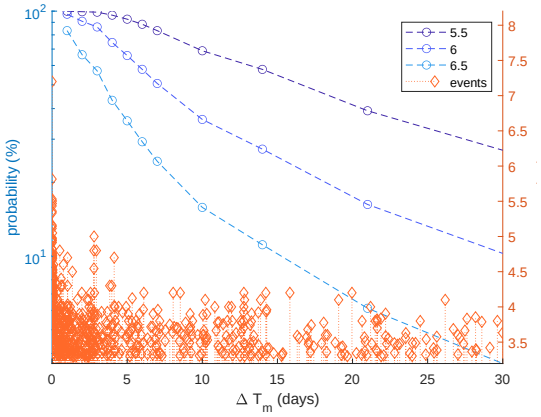

Figure B.13: Probability of large aftershocks for the Darfield sequence with $M_0 = 3.3$ using the MOL produced by the EVD.

Table B.28: The 2010 Darfield sequence model parameter estimates at $M_0 = 3.3$ for the MOL using the MLE method and associated errors using a 95% confidence intervals.

ΔT_m	β	±	K_0	±	c_0	±	p_0	±
1	1.38	*0.08*	59.14	*17.03*	0.004	*0.01*	0.83	*0.17*
2	1.58	*0.08*	74.79	*12.64*	0.002	*0.00*	0.72	*0.11*
3	1.70	*0.08*	88.34	*11.12*	0.001	*0.00*	0.64	*0.08*
4	1.76	*0.08*	83.82	*9.61*	0.001	*0.00*	0.67	*0.07*
5	1.78	*0.08*	80.58	*8.75*	0.002	*0.00*	0.69	*0.07*
6	1.83	*0.08*	80.13	*8.29*	0.002	*0.00*	0.70	*0.07*
7	1.86	*0.08*	78.58	*7.94*	0.002	*0.00*	0.71	*0.07*
10	1.92	*0.08*	75.91	*7.41*	0.003	*0.00*	0.74	*0.06*
14	1.99	*0.07*	77.16	*7.18*	0.002	*0.00*	0.72	*0.05*
21	2.06	*0.07*	74.87	*7.06*	0.003	*0.00*	0.76	*0.05*
30	2.14	*0.07*	74.38	*7.06*	0.004	*0.01*	0.77	*0.05*

Table B.29: The 2010 Darfield sequence model parameter estimates using $M_0 = 3.3$ for the ETAS model using the MLE method and associated errors using a 95% confidence intervals. The model parameter $\mu = 0.0$ was fixed during the model parameter estimation.

ΔT_m	β	±	K	±	c	±	p	±	α	±
1	1.90	*0.13*	51.90	*85.90*	0.009	*0.017*	1.51	*0.77*	0.05	*0.95*
2	2.11	*0.12*	34.30	*46.30*	0.003	*0.008*	1.02	*0.74*	0.72	*1.01*
3	2.20	*0.11*	27.20	*56.10*	0.002	*0.007*	0.95	*0.48*	0.77	*1.46*
4	2.25	*0.11*	23.50	*19.40*	0.003	*0.004*	0.99	*0.20*	0.84	*0.58*
5	2.25	*0.11*	20.90	*17.00*	0.004	*0.006*	1.05	*0.25*	0.81	*0.69*
6	2.30	*0.10*	17.70	*14.30*	0.004	*0.006*	1.01	*0.20*	0.92	*0.57*
7	2.32	*0.10*	15.90	*30.60*	0.005	*0.009*	1.02	*0.42*	0.94	*2.13*
10	2.38	*0.10*	11.80	*20.30*	0.005	*0.015*	0.99	*0.51*	1.12	*2.34*
14	2.43	*0.10*	11.80	*12.70*	0.003	*0.004*	0.95	*0.14*	1.24	*0.38*
21	2.51	*0.10*	8.93	*9.05*	0.005	*0.007*	0.97	*0.14*	1.30	*0.47*
30	2.58	*0.09*	8.41	*8.89*	0.004	*0.013*	0.95	*0.15*	1.41	*1.35*

Table B.30: Variance for 2010 Darfield sequence Gamma priors. Gamma prior means are provided using the MLE point parameter estimate. In order, the priors are for the MOL and ETAS model and remain the same for the different M_0.

	K	c	p	
	3.0	1e-6	0.01	
μ	K	c	p	α
1e-7	1.0	1e-7	0.01	0.1

B.5.1 Increasing M_0

Table B.31: MCMC sampling of model parameter estimates for the Darfield sequence fitted to the MOL for $M_0 = 3.3$. The 95% confidence intervals are indicated by the lower (-) and upper (+) bounds of the model parameter distribution.

ΔT_m	β	β -	β +	K	K -	K +	c	c -	c +	p	p -	p +
1	1.38	1.21	1.56	59.19	55.84	62.56	0.004	0.002	0.006	0.82	0.77	0.88
2	1.59	1.42	1.76	74.70	71.50	78.07	0.002	0.001	0.004	0.72	0.67	0.78
3	1.72	1.55	1.89	88.29	84.99	91.50	0.005	0.004	0.007	0.69	0.63	0.74
4	1.78	1.61	1.95	83.77	80.41	86.85	0.001	< 0.001	0.003	0.67	0.62	0.72
5	1.80	1.64	1.97	80.51	77.25	83.85	0.002	0.001	0.004	0.70	0.65	0.75
6	1.84	1.68	2.01	80.16	76.98	83.24	0.002	0.001	0.004	0.70	0.65	0.75
7	1.87	1.71	2.04	78.53	75.38	81.51	0.002	0.001	0.004	0.71	0.66	0.76
10	1.93	1.77	2.10	75.91	72.91	78.77	0.003	0.001	0.005	0.74	0.69	0.79
14	2.00	1.85	2.17	77.09	74.13	80.17	0.002	0.001	0.004	0.72	0.68	0.76
21	2.08	1.92	2.24	74.77	71.84	77.86	0.003	0.002	0.005	0.75	0.72	0.79
30	2.15	2.00	2.31	74.29	71.02	77.61	0.004	0.002	0.006	0.77	0.73	0.80

Table B.32: MCMC sampling of model parameter estimates for the Darfield sequence fitted to the ETAS model for M_0 = 3.3. The 95% confidence intervals are indicated by the lower (-) and upper (+) bounds of the model parameter distribution.

ΔT_m	β	β -	β +	μ	μ -	μ +	K	K -	K +	c	c -	c +	p	p -	p +	α	α -	α +
1	1.90	1.70	2.11	0.009	0.008	0.010	51.99	49.91	53.96	0.009	0.008	0.010	1.50	1.41	1.61	0.01	< 0.01	0.16
2	2.12	1.92	2.32	0.003	0.002	0.004	34.29	32.38	36.23	0.003	0.002	0.004	1.04	0.97	1.12	0.63	0.36	0.90
3	2.22	2.03	2.41	0.002	0.002	0.003	27.19	25.3	29.3	0.002	0.001	0.003	0.92	0.86	0.99	0.79	0.53	1.05
4	2.27	2.08	2.45	0.003	0.002	0.004	23.5	21.58	25.58	0.003	0.002	0.004	0.98	0.92	1.05	0.82	0.57	1.05
5	2.27	2.09	2.46	0.004	0.004	0.005	20.97	19.11	22.87	0.004	0.003	0.005	1.03	0.97	1.10	0.82	0.58	1.04
6	2.31	2.14	2.50	0.004	0.003	0.005	17.72	15.94	19.64	0.004	0.003	0.005	1.01	0.95	1.06	0.90	0.68	1.11
7	2.34	2.16	2.52	0.005	0.004	0.006	15.94	14.08	18.05	0.005	0.004	0.006	1.03	0.98	1.09	0.89	0.67	1.09
10	2.39	2.22	2.58	0.005	0.004	0.006	11.74	9.964	13.71	0.005	0.004	0.006	1.00	0.95	1.05	1.08	0.88	1.27
14	2.44	2.27	2.62	0.003	0.003	0.004	11.9	10.15	13.8	0.003	0.002	0.004	0.94	0.90	0.99	1.25	1.06	1.42
21	2.52	2.35	2.69	0.005	0.004	0.006	8.93	7.275	10.78	0.005	0.004	0.006	0.98	0.94	1.02	1.26	1.08	1.42
30	2.59	2.42	2.76	0.004	0.003	0.005	8.437	6.763	10.8	0.004	0.003	0.005	0.96	0.92	1.00	1.38	1.21	1.54

Table B.33: The 2010 Darfield sequence model parameter estimates with $M_0 = 3.5$ for the MOL using the MLE method and associated errors using a 95% confidence intervals.

ΔT_m	β	±	K_0	±	c_0	±	p_0	±
1	1.50	*0.10*	33.41	*12.29*	0.008	*0.010*	1.03	*0.22*
2	1.67	*0.10*	44.33	*9.71*	0.005	*0.007*	0.90	*0.14*
3	1.79	*0.10*	55.72	*8.94*	0.002	*0.004*	0.79	*0.10*
4	1.84	*0.10*	54.21	*7.86*	0.002	*0.004*	0.80	*0.09*
5	1.88	*0.10*	53.75	*7.26*	0.002	*0.004*	0.80	*0.09*
6	1.92	*0.10*	53.84	*6.89*	0.002	*0.004*	0.80	*0.08*
7	1.95	*0.10*	53.05	*6.59*	0.003	*0.004*	0.81	*0.08*
10	2.04	*0.10*	52.41	*6.12*	0.003	*0.004*	0.82	*0.07*
14	2.13	*0.09*	54.05	*5.91*	0.002	*0.004*	0.80	*0.06*
21	2.17	*0.09*	51.68	*5.69*	0.003	*0.005*	0.84	*0.06*
30	2.23	*0.09*	51.08	*5.61*	0.004	*0.005*	0.85	*0.06*

Table B.34: The 2010 Darfield sequence model parameter estimates using $M_0 = 3.5$ for the ETAS model using the MLE method and associated errors using a 95% confidence intervals. The model parameter $\mu = 0.0$ was fixed during the model parameter estimation.

ΔT_m	β	±	K	±	c	±	p	±	α	±
1	2.12	*0.17*	45.40	*44.10*	0.004	*0.005*	1.27	*0.31*	0.62	*0.56*
2	2.31	*0.16*	32.20	*113.00*	0.002	*0.006*	1.08	*0.47*	0.99	*3.92*
3	2.39	*0.15*	29.00	*28.20*	0.002	*0.003*	0.99	*0.18*	0.98	*0.60*
4	2.45	*0.14*	22.40	*79.00*	0.002	*0.029*	0.98	*1.32*	1.14	*3.79*
5	2.48	*0.14*	19.20	*18.80*	0.002	*0.004*	0.99	*0.20*	1.20	*0.79*
6	2.53	*0.14*	16.90	*17.50*	0.002	*0.003*	0.96	*0.14*	1.30	*0.55*
7	2.56	*0.14*	14.40	*15.20*	0.002	*0.003*	0.95	*0.14*	1.41	*0.53*
10	2.66	*0.14*	11.50	*13.00*	0.002	*0.003*	0.93	*0.13*	1.56	*0.44*
14	2.74	*0.13*	11.60	*12.50*	0.002	*0.003*	0.91	*0.10*	1.56	*0.40*
21	2.77	*0.13*	9.71	*9.78*	0.002	*0.004*	0.95	*0.11*	1.59	*0.37*
30	2.83	*0.13*	9.54	*15.70*	0.002	*0.004*	0.95	*0.19*	1.65	*0.98*

Table B.35: The 2010 Darfield sequence model parameter estimates using $M_0 = 3.7$ for the MOL using the MLE method and associated errors using a 95% confidence intervals.

ΔT_m	β	±	K_0	±	c_0	±	p_0	±
1	1.74	*0.12*	19.91	*9.05*	0.009	*0.011*	0.27	*0.22*
2	1.95	*0.13*	29.95	*7.92*	0.005	*0.007*	0.16	*0.14*
3	2.03	*0.12*	35.87	*7.23*	0.003	*0.005*	0.12	*0.10*
4	2.08	*0.12*	34.81	*6.40*	0.003	*0.005*	0.11	*0.09*
5	2.12	*0.12*	35.24	*5.98*	0.003	*0.005*	0.10	*0.09*
6	2.18	*0.12*	35.75	*5.70*	0.003	*0.005*	0.10	*0.08*
7	2.21	*0.12*	35.28	*5.45*	0.003	*0.005*	0.09	*0.08*
10	2.29	*0.13*	35.01	*5.05*	0.003	*0.005*	0.09	*0.07*
14	2.41	*0.13*	36.84	*4.87*	0.003	*0.004*	0.07	*0.06*
21	2.43	*0.13*	35.12	*4.62*	0.004	*0.004*	0.07	*0.06*
30	2.50	*0.13*	34.74	*4.51*	0.004	*0.005*	0.07	*0.06*

Table B.36: The 2010 Darfield sequence model parameter estimates using $M_0 = 3.7$ for the ETAS model using the MLE method and associated errors using a 95% confidence intervals. The model parameter $\mu = 0.0$ was fixed during the model parameter estimation.

ΔT_m	β	±	K	±	c	±	p	±	α	±
1	2.69	*0.24*	0.43	*1.22*	0.0001	*0.0007*	1.18	*0.21*	4.07	*0.94*
2	3.02	*0.24*	50.70	*52.70*	0.0023	*0.0036*	1.16	*0.27*	0.92	*0.66*
3	2.97	*0.21*	49.00	*47.30*	0.0023	*0.0030*	1.13	*0.23*	0.85	*1.86*
4	3.03	*0.21*	41.80	*36.70*	0.0022	*0.0069*	1.11	*0.42*	0.99	*1.80*
5	3.06	*0.21*	35.00	*35.30*	0.0022	*0.0032*	1.09	*0.17*	1.11	*0.67*
6	3.16	*0.21*	31.00	*31.10*	0.0020	*0.0029*	1.05	*0.17*	1.21	*0.61*
7	3.19	*0.21*	28.20	*86.70*	0.0019	*0.0085*	1.05	*0.16*	1.28	*0.91*
10	3.31	*0.21*	22.60	*25.40*	0.0017	*0.0029*	1.01	*0.16*	1.46	*0.52*
14	3.44	*0.20*	23.70	*27.00*	0.0013	*0.0021*	0.97	*0.14*	1.48	*0.52*
21	3.44	*0.20*	19.70	*61.60*	0.0017	*0.0026*	1.01	*0.12*	1.54	*1.66*
30	3.53	*0.20*	18.80	*19.90*	0.0017	*0.0029*	1.01	*0.20*	1.57	*0.38*

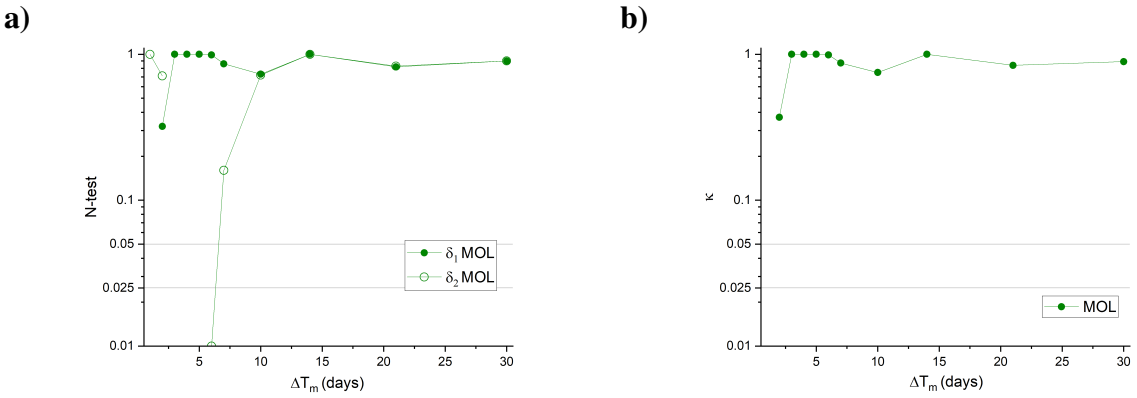

Figure B.14: The performance of the MOL for various training time intervals for the Darfield sequence using the EVD method for forecasting using $M_0 = 3.3$. Forecast performance scores are listed for the a) N-test (δ_1, δ_2) and the b) M-test (κ).

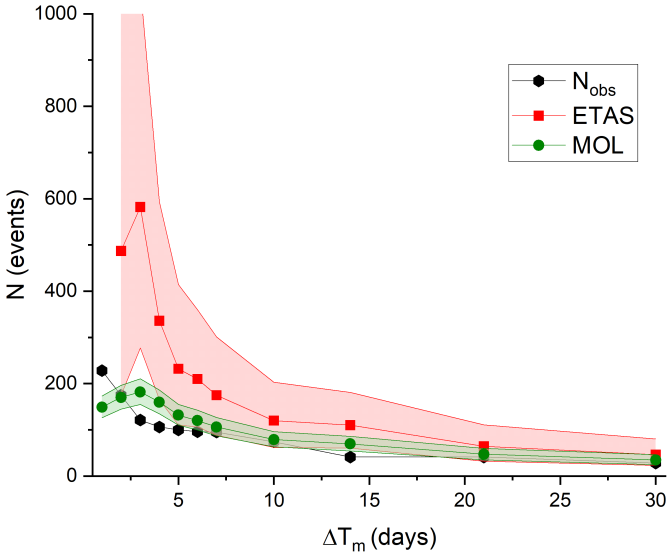

Figure B.15: Average number of events generated during seven day forecast for Darfield sequence with $M_0 = 3.3$.

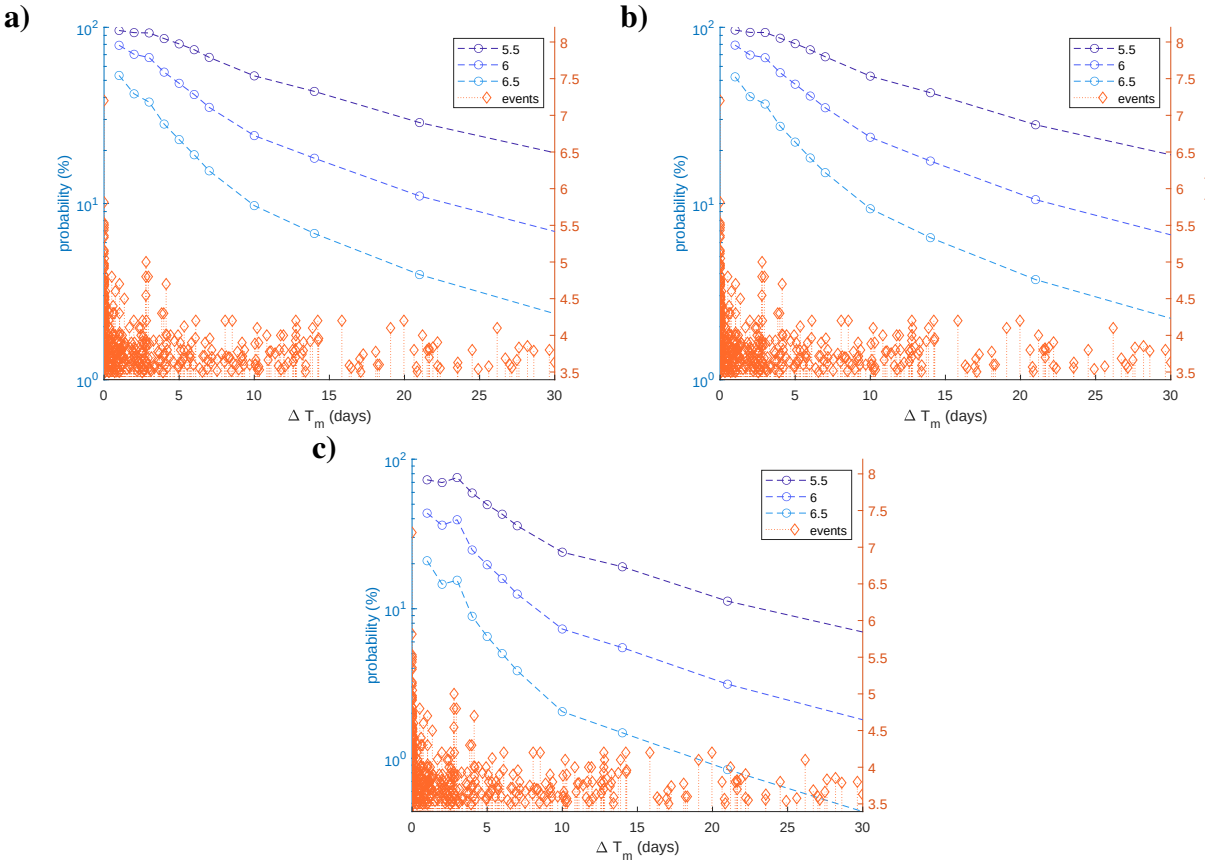

Figure B.16: Probability of large aftershocks for the Darfield sequence for $M_0 = 3.5$ forecasted using the a) MOL with BPD, b) MOL with EVD, and c) ETAS model.

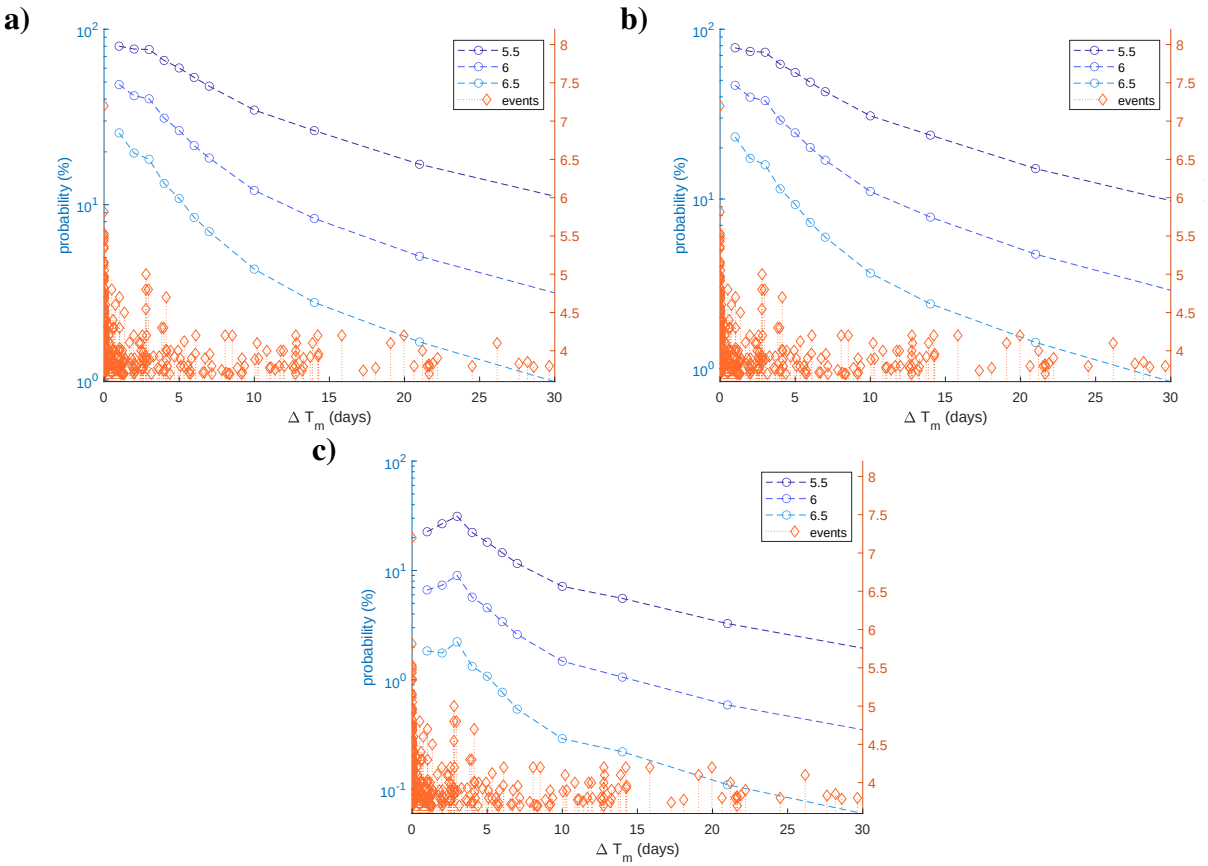

Figure B.17: Probability of large aftershocks for the Darfield sequence for $M_0 = 3.7$ forecasted using the a) MOL with BPD, b) MOL with EVD, and c) ETAS model.

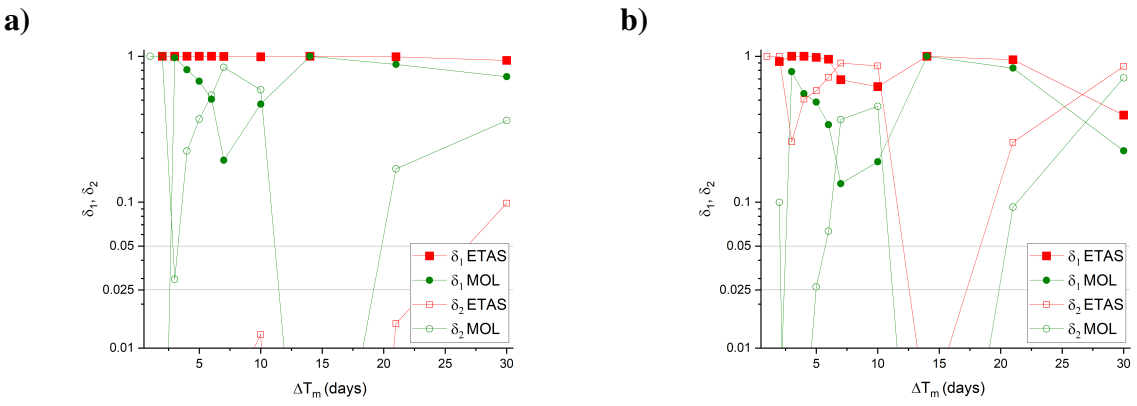

Figure B.18: N-test performance of the Darfield sequence with a) $M_0 = 3.5$ and b) $M_0 = 3.7$.

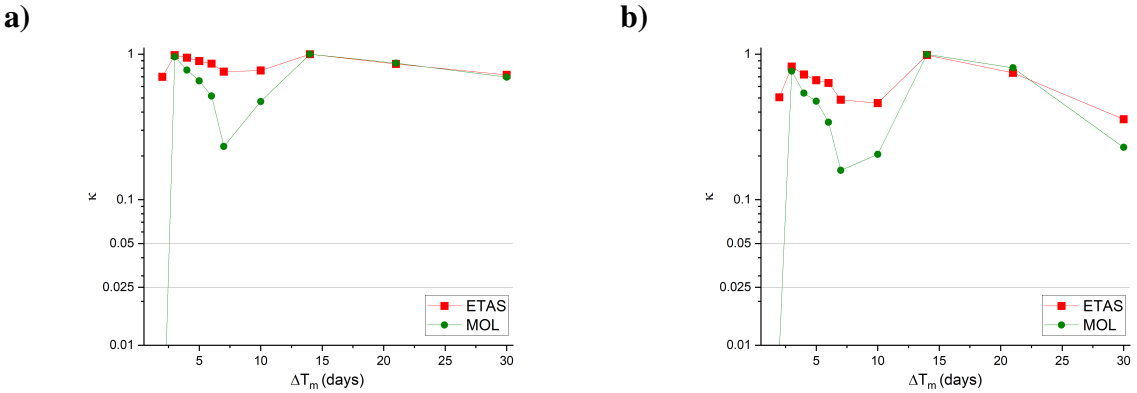

Figure B.19: M-test performance of the Darfield sequence with a) $M_0 = 3.5$ and b) $M_0 = 3.7$.

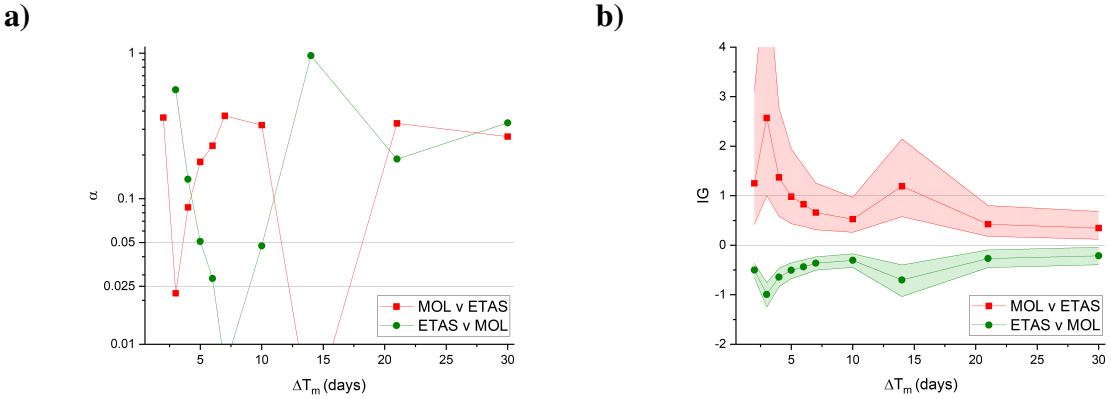

Figure B.20: a) R-test performance of the Darfield sequence with $M_0 = 3.5$. b) The associated information gain is plotted for $M_0 = 3.5$ with 95% confidence intervals.

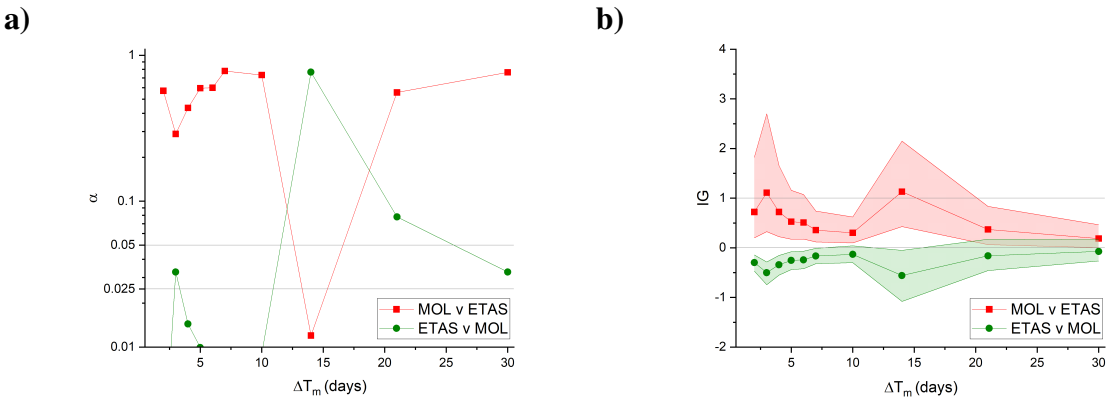

Figure B.21: a) R-test performance of the Darfield sequence with $M_0 = 3.7$. b) The associated information gain is plotted for $M_0 = 3.7$ with 95% confidence intervals.

Curriculum Vitae

Name:	Elisa Dong
Post-Secondary Education and Degrees:	University of Waterloo Waterloo, ON 2014 - 2019 B.Sc. Western University London, ON 2019 - 2022 M. Sc.
Honours and Awards:	OGS QEII-SST 2020 - 2021
Related Work Experience:	Teaching Assistant University of Waterloo 2016 - 2018 Teaching Assistant Western University 2019 - 2021

Public Presentations:

AGU 2021, Conference Presentation entitled Comparison of the forecasting abilities of the ETAS model versus the modified Omori law for several prominent aftershock sequences, Abstract ID: 871608

GAC-MAC 2021, Conference Presentation entitled Early Forecasting for the Probability of Large Aftershocks for the M_w6.5 Monte Cristo Range Sequence, ID: 132693